國立交通大學

機械工程學系

博士論文

一氧化碳毒化對質子交換膜燃料電池性能影響之分析

Analysis of CO Poisoning Effect on the Performance of Proton Exchange Membrane Fuel Cell

研究生：王建評

指導教授：陳俊勳　教授
　　　　　曲新生　教授

中華民國 九十六 年 六 月

一氧化碳毒化對質子交換膜燃料電池性能影響之分析

Analysis of CO Poisoning Effect on the Performance of Proton Exchange Membrane Fuel Cell

研究生：王建評

指導教授：陳俊勳、曲新生

Student：Chien-Ping Wang

Advisor：Chiun-Hsun Chen
Hsin-Sen Chu

國立交通大學
機械工程學系
博士論文

A Thesis
Submitted to Department of Mechanical Engineering
National Chiao Tung University
in partial Fulfillment of the Requirements
for the Degree of
Doctor of Philosophy
in
Mechanical Engineering

June 2007
Hsinchu, Taiwan, Republic of China

中華民國九十六年六月

國立交通大學

論文口試委員會審定書

本校 機械工程 學系博士班 王建評 君

所提論文（中文） 一氧化碳毒化對質子交換膜燃料電池性能影響之分析

（英文） Analysis of CO Poisoning Effect on the Performance of Proton Exchange Membrane Fuel Cell

合於博士資格水準、業經本委員會評審認可。

口試委員： 翁政義 林清發
陳朝光 顏維謀
陳發林

指導教授： 曲新生 陳俊勳

系主任： 教授

中華民國 九六 年 五 月 二十三 日

一氧化碳毒化對質子交換膜燃料電池性能影響之分析

研究生：王建評　　　　　　　　　指導教授：陳俊勳、曲新生

摘要

近年來由於化石燃料的短缺及有限的蘊藏量，加上傳統應用化石燃料發電方式所產生大量的溫室氣體，造成石油價格攀升及地球暖化等重大議題。因此再生能源及潔淨能源科技的發展成為本世紀最重要的研究課題之一。燃料電池因具有潔淨、高效率及模組化特性，使得燃料電池此一新興能源科技的發展倍受重視。未來質子交換膜燃料電池之重點研究方向有二，一為性能提昇及價格下降，另一為如何提高其可靠度及耐久性

。質子交換膜燃料電池的操作性能與使用期限，與輸入燃氣中所含的不純物質(如陽離子、一氧化碳) 有密切的影響。重組器中所含的一氧化碳由於比氫氣具有與白金更強的鍵結能力，而附著於白金表面造成觸媒參與電化學反應的有效面積降低，即使微量的一氧化碳亦是造成燃料電池性能下降及縮短使用期限的重要因素。因此，本研究主要目的即在建立一套完整的理論模式。探討一氧化碳影響電池性能的主要機制，以及受到一氧化碳毒化後白金觸媒表面受到氫氣與一氧化碳的覆蓋情形與電池內部包含氣體、液體的傳輸現象，研究提升電池抵抗一氧化碳毒化的能力。

首先本文發展出一維暫態的 CO 毒化理論模式，探討 CO 在陽極觸媒層中的暫態毒化現象。由理論結果顯示，氫氣在白金表面的覆蓋率隨著時間而降低，這是由於 CO 佔據白金表面所造成。CO 的濃度愈高使得氫氣能參與電化學反應的機會愈小，也縮短達到穩態的時間，

亦即縮短燃料電池的使用期限。另外在較低的 CO 濃度下，增加陽極過電位及增加觸媒的孔隙度明顯增加產生的電流密度。

其次本文推導一維的兩相流理論模式探討 CO 毒化對 PEM 燃料電池性能影響之分析。由結果顯示，高濃度的 CO 造成白金有效反應面積下降。由於電化學反應減緩，陰極觸媒產生的液態水減少使得陽極與陰極的液態水含量降低。在高 CO 濃度及稀薄的氫氣含量下，由於電滲透效應降低及陰極反應生成的液態水減少，使得薄膜內的液態水分佈梯度降低。CO 濃度的改變相較氫氣含量對電池內部液態水的分佈具有較大的影響。CO 濃度在 10-50 ppm 之間電流密度急劇的降低。在不同的 CO 濃度下，提高氫氣含量均可增加電池輸出之電流密度，提高電池抵抗 CO 毒化的能力。

接下來本文推導出一維暫態的兩相流理論模式探討 CO 毒化對 PEM 燃料電池性能影響之暫態分析。結果顯示，高濃度的 CO 造成白金有效反應面積下降也同時降低達到穩態所需的時間。在不同的 CO 濃度下增加氫氣的含量可明顯增加達到穩態的時間。CO 濃度在 10 ppm，操作電壓在 0.6 V 以上，可達到較佳的抗 CO 毒化的能力以維持燃料電池的操作性能。

本文進一步探討高溫型 PBI 薄膜。由於操作溫度可達 200^{o}C，因此水管理及一氧化碳毒化問題可有效解決，並分別由實驗量測及理論分析同時驗證。由實驗結果得知，操作溫度愈高可得愈佳的電池性能，因高溫下可提升化學反應速率。輸入 CO 濃度高達 3000 ppm 及 40% H_2 下，電池性能僅下降約 26%。在不同的一氧化碳及氫氣濃度下，理論分析結果與實驗非常符合。由本文的研究結果可準確分析燃料成份比例對電池性能的影響，以及電池性能隨時間衰退的變化，提供電池或重組器設計重要參考依據。

Analysis of CO Poisoning Effect on the Performance of Proton Exchange Membrane Fuel Cell

student：Chien-Ping Wang　　　　Advisor：Chiun-Hsun Chen
　　　　　　　　　　　　　　　　　　Hsin-Sen Chu

ABSTRACT

Recently, the increase of global energy demand will propel a more rapid depletion of world's fossil fuel reserves and the burning of the fossil fuels for generating electricity will release greenhouse gases into the atmosphere. The requirements for developing the renewable energy and clean energy technology become the most important issue for the human being in this century. Much attention has been devoted to the developments of the fuel cells because they are clean, high efficient and capable of module. There are two major topics of the R&D programs for the PEM fuel cell systems. First, the improvement of the performance and the decrease of the cost, secondly, enhance the reliability and durability of the fuel cells.

Fuel cell performance and life time are strongly influenced by impurities in the fuel gas (cation and CO). Reforming from methanol or gasoline fuels is the most widely used method to generate hydrogen fuel. Even trace amount CO would reduce the hydrogen electro-oxidations effectively by occupying the Pt reacting surface which results in a decrease in the cell performance and life time. To keep a long time and stable operation, how to reduce the CO concentration effectively from the reformer and enhance the tolerance for CO of the fuel cell will become a significant topic. In this work, a comprehensive theoretical model of the poisoning effect of PEM fuel cells by CO is investigated to promote the tolerance for CO and thus elucidate the transport phenomena inside the cell.

In the first part of this study, a one-dimensional transient mathematical model is applied to simulate the carbon monoxide poisoning effect on the performance of the PEM fuel cell. The transient behavior of CO poisoning process across the anode catalyst layer is investigated. The results show that the hydrogen coverage, θ_H, decreases with the time due to the CO adsorption on the catalyst site. A higher CO concentration results in a less available catalyst site for hydrogen electro-oxidation and a more significant decrease in the response time to reach steady state t_{ss}. Increasing anode overpotential and gas porosity would result in an increase in the current density, especially at low level of CO concentration.

Second, a one-dimensional, two-phase mathematical model was developed to analyze the CO poisoning effect on the performance of a PEM fuel cell. Both vapor and liquid water transport are examined inside the cell. The theoretical results indicate that a higher CO concentration results in large CO coverage across the anode catalyst layer. The slowing of the chemical reactions at both the anode and the cathode reduce the liquid water saturation level in the catalytic layers. At high CO concentration and dilute hydrogen feed, the effect of the electro-osmotic drag is small and less liquid water is generated at the cathode catalyst layer, causing the liquid water distribution to have a small slop across the membrane. The distribution of liquid water depends more strongly on the CO concentration than on dilution of hydrogen in the MEA of the fuel cell. A large dropping rate of the current density is observed in the range between 10-50 ppm CO. Increasing the amount of pure hydrogen drastically increases the current density for a wide range of CO contents, promoting the tolerance for CO of the fuel cell.

Third, a one-dimensional, two-phase, transient mathematical model was extended to analyze how carbon monoxide poisoning affects the performance of a PEM fuel cell. The theoretical results indicate that a higher CO concentration results in less hydrogen coverage and a large drop in the time to reach steady state t_{ss}. Increasing the amount of pure hydrogen drastically increases t_{ss} for a wide range of CO contents. At 10 ppm CO, a long t_{ss} can be achieve using pure hydrogen, especially at high cell voltage, promoting the tolerance for CO and providing the desired performance of the fuel cell.

Finally, high temperature proton exchange membrane fuel cells have drawn great attentions due to high CO tolerance and overcoming water managements. In this wrok, theoretical and experimental studies were made to analyze the transient CO poisoning process. Experimental results were measured at different temperature and suffered from various CO contents. Higher performance was obtained at elevated temperature due to faster chemical kinetics. Only 26% of performance loss is obtained under 3% CO and 40%H_2. The effects of temperature, CO contents and H_2 dilutions on the fuel cell performance and the time to reach steady t_{ss} are all investigated. The predictions of the degradation of fuel cell performance show good agreements with experimental results under various fuel compositions. Thus, the present results can provide comprehensive information for designing fuel cell system and methanol reformer.

誌謝

首先感謝恩師 曲新生博士，恩師除了在學術上的悉心指導之外，在待人處世方面更是我學習的典範。其次感謝口試委員翁政義、陳朝光、林清發、陳發林、顏維謀諸位教授對於論文的建議及指教，使得本論文更加嚴謹而充實。

此外感謝世國、木勝、時明等學長在學業及生活上的關心與照顧，幫助我在研究過程中解決許多困難。

最後特別感謝我的家人，在這漫長的求學過程中，不斷地給予我支持及鼓勵，陪伴我經歷過許多挫折及挑戰，僅以此論文獻給所有關心及照顧我的人。

TABLE OF CONTENTS

LIST OF TABLES

LIST OF FIGURES

NOMENCLATURE

a	contact area of Pt catalyst ($cm^2\ cm^{-3}$)
b_{fH}	ratio of forward to backward of hydrogen adsorption (atm)
b_{fCO}	ratio of forward to backward of CO adsorption (atm)
C	concentration of reactant gas (mole cm^{-3})
D	diffusion coefficient ($cm^2\ s^{-1}$)
i	current density (A cm^{-2})
k	conductivity of the Nafion phase
K	permeability, cm^2
k_{eH}	hydrogen electro-oxidation rate constant (A cm^{-2})
k_{eCO}	CO electro-oxidation rate constant (A cm^{-2})
k_{fH}	hydrogen adsorption rate constant (A $cm^{-2}\ atm^{-1}$)
k_{fCO}	CO adsorption rate constant (A $cm^{-2}\ atm^{-1}$)
M	molecular weight, g mol^{-1}
n	number of electrons
P	total pressure (atm)
R	universal gas constant (J $mol^{-1}\ K^{-1}$)
s	liquid water saturation
T	temperature (K)
t	time (s)
X	molar fraction
x	distance (μm)

Greek

ε	porosity
θ	coverage ratio on Pt catalyst site
ξ	molar area density of Pt catalyst sites (C cm^{-2})
ϕ	ionic potential (V)
μ	viscosity, (g cm^{-1} s^{-1})
ρ	density, (gcm^{-3})
η	overpotential
γ	stoichiometric coefficient
σ	rate constant of Henry's law
ΔE_H	activation energy change for hydrogen dissociative adsorption near CO occupied sites (J mol^{-1})
ΔG_f	variation of free energy of CO adsorption between zero and full coverage (J mol^{-1})

Superscripts

in	inlet at catalyst layer
sat	saturation

Subscripts

CL	catalyst layer
CO	carbon monoxide
H_2	hydrogen
MEM	membrane
O_2	oxygen
s	solid phase of electrode

ss	steady state
wg	water vapor
wn	liquid water in Nafion phase

1. INTRODUCTION

1.1 Motivation

From the world energy outlook of IEA 2006, the global energy demand grows nearly 60% since 2002 to 2030. From Fig 1.1, fossil fuels are the most important resources which account for almost 90% of the energy growth. Due to the increased of global energy demand will propel a more rapid depletion of world's fossil fuel reserves. In the divinable future, this will not only increase the oil price but also release a great deal of greenhouse gases into the atmosphere. From Fig 1.2, the prediction of global CO_2 emission by fuel grows nearly 55% between 2004 and 2030. Base on the information the developments of renewable and clean energy technologies become one of the most important issue in this century.

The hydrogen, fuel cells and infrastructure technologies program is shown in Figure 1.3 [EERE/DOE, 2006]. There are four strategic goals of EERE for integrating R&D activities such as hydrogen production, delivery, storage and applications. Figure 1.4 shows a diverse set of resources to produce hydrogen. Biomass, geothermal, hydro, wind, and fossil fuel are able to produce hydrogen. Through use of fuel cells in distributed generation and transportation perform high efficiency and low emissions. The hydrogen economy timeline as shown in Figure 1.5 is predicted by DOE. There are four transition phases to a hydrogen economy. The transition will require strong public and private partnerships, and this transition will take several decades.

Fuel cells are highly efficient energy conversion devices that can replace combustion engine technology. Combining hydrogen and oxygen, fuel cells generate electrical power and produce pure water through electrochemical reactions. Fuel cells are quiet, efficient and convert energy electrochemically rather than mechanically. In recent years, the proton exchange membrane fuel cell is highly attractive for both portable and stationary application due to its high operating efficiency and environmental friendliness. This gives the PEM fuel cells great flexibility of a wide range of applications, Fig 1.6.

The most efficient fuel for use in a PEM fuel cell is pure hydrogen. However, this is difficult to store and has a high cost of production. Reforming from hydrocarbons, including gasoline and alcohol is the most extensively used technique for generating hydrogen fuel for use in proton exchange membrane fuel cells, which contain 45% hydrogen, 10ppm CO, 15% CO_2 and 1% CH_4 [1]. CO at a concentration even as low as 5-10 ppm effectively blocks Pt reaction sites for the electro-oxidation of hydrogen [2-3]. The affinity between CO and Pt is such that even at this low concentration of CO, the consequent loss of performance is severe [4, 5]. For the reforming process to be effective in the fuel cell system, this problem must be solved.

Recently, high temperature phosphoric acid doped membrane fuel cells have been developed to overcome water management and CO tolerance. PBI is a basic polymer and exhibits high conductivity through doping with various acids or bases. Sulphuric acid and phosphoric acid are used to perform high membrane conductivity. The operating temperature is around 120~180^{o}C of acid-doped PBI membrane fuel cell which is much higher than PFSA polymer membrane fuel cells. Water inside fuel cell becomes vapor phase and exhibit high tolerance of CO. Chemical kinetics also become faster at elevated temperature. Protons conduct in solid matrix for PBI membrane, so the membrane conductivity is less influence by liquid water content. In addition, a higher mechanical strength and a lower permeability of PBI membrane provides an alternative choice to replace Nafion. Fuel not only can be fed directly into the fuel cell but also can be made into a compact design with methanol reformer.

Here we investigate the effects of CO poisoning and hydrogen dilution on the performance of fuel cells. The theoretical model that combines transport equations of reactants, water and CO poisoning is developed. Transient behavior is also one of the most important issues that we investigated in this work. Our purpose is to gain a fundamental understanding of the CO poisoning process, including coverage profiles, reactants, vapor and liquid water transport. High temperature PBI membrane fuel cell is also investigated in our theoretical and experimental studies. These results can further realize CO poisoning process inside fuel cell. Fuel cell performance under various fuel compositions can be accurately predicted from our simulation and realize the transient degradations of the fuel cell performance. Thus, this can provide sufficient information for the designing reformer and the fuel cell system.

1.2 Fuel Cell Types

Proton Exchange Membrane Fuel Cell (PEMFC)

In 1960s, the first proton exchange membrane fuel cell was developed by General Electric in the United States [6]. The first space vehicle was used by NASA. Figure 1.7 shows the schematic diagram of the PEM fuel cell. The electrolyte is an ion conduction polymer to move H^+ ion through the supporting ionomer structure. The PEM fuel cells work at low temperature which can start quickly. The thinness of the MEA makes the compact design and without corrosive fluid in the cell. This makes that the PEMFC is suitable for portable and stationary applications. Fig 1.8 shows the component diagram of a PEM fuel cell. At the anode side, the hydrogen oxidation reaction releasing H^+ ions and electrons

$$2H_2 \rightarrow 4H^+ + 4e^- \tag{1-1}$$

At the cathode, the oxygen reduction reaction reacts with H^+ ions and electrons to produce water

$$O_2 + 4e^- + 4H^+ \rightarrow 2H_2O \tag{1-2}$$

Only water is produced by the above electro-chemical reactions. This results in an environmental friendliness to replace the internal combustion engine.

Alkaline Electrolyte Fuel Cells

The first application of the alkaline fuel cell was adopted by F.T. Bacon at Cambridge that took human to the moon in Apollo mission [6]. The electrolyte of the AFC is an alkaline solution. Potassium hydroxide or sodium hydroxide solution is the prime use as the electrolyte. The basic chemistry at the anode is

$$2H_2 + 4OH^- \rightarrow 4H_2O + 4e^- \tag{1-3}$$

The electrons pass around the external circuit. At the cathode, new OH^- ions is formed

$$O_2 + 4e^- + 2H_2O \rightarrow 4OH^- \tag{1-4}$$

The main advantages of the AFC are the low activation overvoltage loss at the cathode and the low system cost. In the low temperature fuel cells, activation loss is the most important voltage loss, but the reason is not well understood. The very low cost of the electrolyte (potassium hydroxide) and not usually have bipolar plate reducing the cost the alkaline fuel cells. The main disadvantage of the AFC is the CO_2 react with the KOH. The reduction of the OH^- concentration will greatly drop the cell performance.

Direct Methanol Fuel Cell

In the DMFC, methanol is used as a fuel instead of hydrogen which is effectively produced from hydrocarbon fuels. Methanol fuel works in both the alkaline and PEM electrolytes. The reactions at the anode and cathode depend on the electrolyte used. The use of alkaline electrolyte has a major problem which results in carbonate formation. Current research and development of DMFC is focused on PEM electrolyte.

There are two major problems associated with DMFC. First, the fuel anode reactions proceed much slowly than with hydrogen. Because of methanol reaction is a more complex reaction. This results a far lower power for a given size. Second, the fuel crossover significantly affects the performance of the fuel cells which is particularly acute with PEM electrolyte. Because of methanol mixes well with water and then reaches the air cathode.

Phosphoric Acid Fuel Cell

The PAFC use a phosphoric acid (H_3PO_4) as an electrolyte to conduct proton which like Nafion membrane in the PEM fuel cells. Phosphoric acid is the inorganic acid that has high thermal, chemical, and electrochemical stability. It's also contained high volatility (above 150^{o}C) to be adopted as an electrolyte for fuel cells. Due to its low freezing point (42 ^{o}C) of the pure phosphoric acid, PAFC is usually maintained above such temperature. Unlike PEMFC, the operating temperature of the PAFC is normally around 180 to 200 ^{o}C that has greater tolerance of CO (up to 1%). After long time operation, it is necessary to replenish electrolyte. This is because that the vapor pressure is low and some acid is lost during operation.

.

Molten Carbonate Fuel Cell

The MCFC is one type of high temperature fuel cells (600-700^{o}C). The electrolyte of the MCFC is usually a binary molten mixture of lithium and potassium, or lithium and sodium carbonates. A ceramic matrix of $LiAlO_2$ is considered to retain such electrolyte. Because of the high operating temperature, the alkali carbonates form a highly ionic conductivity with carbonate CO_3^{2-} ions. The anode and cathode reactions are

$$2H_2 + 2CO_3^{2-} \rightarrow 2H_2O + 2CO_2 + 4e^- \tag{1-5}$$

$$O_2 + 2CO_2 + 4e^- \rightarrow 2CO_3^{2-} \tag{1-6}$$

Unlike all the other cells, CO_2 must be supplied to the cathode, and thus converted to carbonate ions. Another important feature is that CO can be fed to the MCFC as hydrogen fuel.

Solid Oxide Fuel Cell

The SOFC is the only one type of fuel cell that contain complete solid-state device. An oxide ion-conducting ceramic material is used as the electrolyte. Because only gas and liquid phase are considered, it is simpler than all the other fuel cell system. Since no liquid electrolyte is needed, the electrolyte management problems that appear with the PAFC and MCFC do not occur. The SOFC works at high operating temperatures (800-1100°C) which means that precious electrocatalysts are not needed. Like MCFC, carbon monoxide also can be fed as fuel to produce electrons. The anode and cathode reactions for the SOFC are

$$2H_2 + 2O^{=} \rightarrow 2H_2O + 4e^- \tag{1-7}$$

$$O_2 + 4e^- \rightarrow 2O^{=} \tag{1-8}$$

There are two types of design of SOFC. The great advantage of the tubular SOFC is that high temperature gas-tight seals are eliminated. This is also the disadvantages of the planar design of the SOFC.

1.3 Literature Survey

Zero-Dimensional Models

The simplest method use only a single equation to describe the cell polarization is the zero-dimensional models. The models can not realize the fundamental understanding of the transport phenomena but are worth for determining the kinetic parameters and are relatively simple for use. A typical expression of the 0-D model is used by Kim et al. [7] which incorporated the gas-phase mass transport limitations

$$V = U + b\log(i_0) - b\log(i) - Ri - m\exp(ni) \tag{1-9}$$

in which V is the cell potential, U is the reversible potential, i_o is the exchange current density, b is the Tafel slope, R represents the total resistance, and m and n are fitting parameters, respectively. Sena et al. [8] used similar approach describing the water transport in the membrane. For Nafion 115 and 117 membranes, liquid water flooded is the limiting effect at high current density. For Nafion 112 membrane, oxygen diffusion effects dominate the cell behavior. Pisani et al. [9] and Passalacqua et al. [10] change the concentration overpotential to be a more complicate function with more fitting parameters. Pisani et al. [9] derived a semi-empirical equation to describe the performance of the fuel cell. The Ohmic overpotential is used to be the only one empirical term in the performance equation. The modeling results showed a quantitative depiction of the voltage drop at high current density. Passalacqua et al. [10] proposed a equation that described the relation between the current density and potential. The results indicated that cell performance is affected by the Nafion content. An optimal content of Nafion was found about 33 wt% of ionomer.

Fuel Cell Modeling

The fuel cell sandwich model shows the cross section of the fuel cell which includes flow field, diffusion media, catalyst layer and membrane. Fuels are fed through the flow field at the anode and cathode side. The fuels flow through the diffusion media and react at the catalyst layers. At the anode catalyst layer, electrons and ions are generated by hydrogen oxidation-reactions. At the cathode catalyst layer, the oxygen reduction reactions produce either liquid or vapor water. Energy and mass transport along with electrochemical kinetics occur through various sandwich layers. Various parts of the fuel cell modeling equations are presented as follows

Membrane Modeling

For polymer electrolyte fuel cells, electrolyte is a proton-conducting membrane. Figure 1.9 shows the structure of the membrane as a function of water content [11]. The first type of membrane modeling treating the membrane system as a single phase is the diffusive model which corresponds to the vapor equilibrated membrane (panel c of figure 1.9). The model assumes that the proton and water dissolve and move by diffusion. The simplest method for use to treat the proton movement is the Ohm's law

$$i = -k\nabla\phi \tag{1-10}$$

where k is the membrane conductivity. The above equation is the simplified result of using dilute theory. Only the interaction between each dissolved species and the solvent is considered. If water transportation is considered in the membrane, the electro osmotic flow can be added to the overall flux of water.

$$N_w = \xi\frac{i}{F} - D_w\nabla C \tag{1-11}$$

in which ξ is the electro-osmotic coefficient. The effect of electro-osmotic drag is proportional to the current density. Kulikovsky [12] and Siegel et al. [13] used this method successfully to treat the membrane as a single phase. Kulikovsky study the nonlinear distribution of water content through the membrane. Water diffusion coefficient drops rapidly blow certain λ value which causes a region with large gradient of water. The model also shows the increase of membrane resistance with current density. Siegel et al. used agglomerate catalyst geometry to analyze the fuel cell behavior. As a result, the optimal void fraction of 0.4 was found for the electro-chemical reactions. Cell performance decreased with the size of the catalyst agglomerate.

One another approach is the hydraulic model that assumes the membrane system as two phases (water and membrane). The membrane is treated as having pores that are filled with liquid water. The water content of the membrane is assumed to be constant shown in panel d of Fig. 1.9. The gas pores of the membrane are filled with liquid water. Bernardi and Verbrugge [14,15] first treated the membrane using above fashion. The Schlogl's equation is used to define the liquid water velocity in the pores of the membrane phase which is related to the pressure gradient and potential gradient. Murgia et al. [16] used the same approach to model the liquid water transport in fuel cells. The study modified the model of Bernardi and Verbrugge (BV model). The MBV model integrated the Bulter-Volmer equation in the catalyst layer to get more stable numerical calculation. The results show indistinguishable between these two models and extend the range of the current density.

Rowe and Li [17] combined both diffusive and hydraulic model to treat the liquid water transport in the membrane. The model investigated temperature distribution and water management in the fuel cell. As a result, the temperature difference becomes larger and low operation temperature and partial humidified streams. At high operating pressure, membrane hydration decrease due to the decrease of water vapor concentration within in the anode electrode.

$$N_w = \xi \frac{i}{F} - D_w \nabla C - C \frac{k}{\mu} \nabla P \tag{1-12}$$

The problem with the above approach is the use of a gas pressure gradient. This means that the gas-phase is exist within the membrane, but does not agree with experiments.

Diffusion Media Modeling

The diffusion media are placed between the catalyst layer and gas channel which is generally made either a carbon paper or a carbon cloth material. The diffusion media provide a structure support and a pathway for reactants, water and electrons. The transportations of the species are discussed as follows

For the gas-phase transport, if the mean free path of the gas molecule is less than 0.01 times the pore radius, the Stefan-Maxwell equation is used to illustrate the gas transport in the fuel cell.

$$\nabla x_i = \sum_{j \neq i} \frac{x_i N_j - x_j N_i}{C_T D_{i,j}^{eff}} \tag{1-13}$$

where x is the molar fraction, $D_{i,j}^{eff}$ is the effective binary diffusion coefficient. As the pore size is comparable to the gas mean free path, Knudsen diffusion becomes more significant. Kulikovsky et al. [18] combined both Stefan-Maxwell and Knudsen diffusion to treat both diffusion medium and catalyst layer of a PEM fuel cell cathode. Two different values of the carbon conductivity is considered to investigated oxygen concentration distribution, potential of carbon phase, electron flow and current density distribution. The simulation results indicate that a dead zone in front of the gas channel within in the catalyst layer is formed with low carbon conductivity. Reduction of the catalyst loading leads only an insignificant effect on the cell performance. Kulikovsky [12] also assumed that vapor water transport by Knudsen diffusion in the catalyst layer. In this work, the Knudsen diffusion coefficient is a function of pore size. The diffusion coefficient of water drops significantly below certain value of water content which cause the high nonlinear distribution of liquid water across the membrane. Membrane resistance and gradient of liquid water distribution increase with current density due to nonlinear drying at the anode side of the membrane.

Bulk diffusion dominates when the pore size is 100 times to the molecule mean free path, and Knudsen diffusion dominates when the pore size 0.1 times to the molecule mean free path. Weber and Newman [11] indicated that Knudsen diffusion become a significant effect when the pore radius is less then about 0.5 μm. Typically, pore size is often 0.5~20 μm in the diffusion media, and 0.05~2 μm. in the Microporous layer. Thus, only microporous layer should be accounted using Knudsen diffusion.

The simplest method to treat the liquid water inside the cells is to neglect it. The liquid water transport is not considered and the effect is to decrease the effective diffusion coefficient of gas species. Gurau et al. [19] developed an analytical solution of a half-cell mode. The parallel composite structure of the diffusion medium with different porosity was applied to mimic the flooding effect. Chu et al. [20] further developed a one-dimensional model to consider the non-uniform porosity of the diffusion medium. In this work, various functions of the porosity are considered to simulate liquid water across the gas diffusion medium.

Gas and liquid are actually coexistence in a porous medium of the fuel cells. The interaction between gas and liquid is expressed as

$$P_c = P_l - P_g = -\frac{2\gamma \cos\theta}{r} \tag{1-14}$$

in which γ is the surface tension of water, θ is the contact angle, r is the pore radius. The most significant aspect of the two-phase model is the prediction of the liquid saturation s which is defined as liquid fraction of pore volume. The liquid water saturation greatly influences the gas diffusion coefficient and represents the flooding effect. He et al. [21] used two-phase model to investigate the interdigitated flow fields of the PEM fuel cells. The simulation results indicate that high pressure gradient between the inlet and outlet channel produce higher performance of the fuel cell. An optimal thickness of the electrode (0.08 cm) is obtained. The higher the channel/shoulder ratio also yields better cell performance. Natarajan and Nguyen [22] developed a three-dimensional model the study the liquid water flooding in the fuel cell cathode. As a result, higher stoichiometric rate and temperature result in higher current density. The cell performance increase with decreasing inlet stream humidity You and Liu [23] developed a multiple-phase mixture model to examine the two-phase distribution in the fuel cell cathode. The liquid water saturation increases with current density. In addition, high humidification temperature at both anode and cathode inlet increase the liquid water saturation but decrease the limiting current density. Pasaogullari and Wang [24] applied the commercial CFD software, Fluent, to study the effect of humidification level and flow rate of reactants on the cell performance and liquid saturation profile. Liquid saturation increased with humidification level along the flow channel. In the fully humidified situation, the membrane are well hydrated which results high current density.

Catalyst Layer Modeling

The simplest type of catalyst layer modeling is the zero-dimensional or interface models. The catalyst layers are treated as an interface between the diffusion media and the membrane. The thickness and the structure of the catalyst layer are assumed to be ignored. Kulikovsky [12] and Natarajan [20] used Faraday's law as a generation/consumption term at the boundary between the membrane and the diffusion medium. More rigorous modeling (porous-electrode model) treat the catalyst layer with finite thickness [16,17]. The characteristic length is the thickness of the catalyst layer. This model is concerned about the chemical-reaction distribution across the catalyst layer. Siegel [13] described a mathematical PEMFC model base on agglomerate catalyst geometry. The model describes that gas flow through pores and then diffuses into agglomerate catalyst, as shown in Fig 1.10. In this approach, the characteristic length is the agglomerate size and the agglomerates are assumed to be uniform. Pisani et al [25] considered cylindrical gas pores of fixed radius through the catalyst layer. Both longitudinal and transverse oxygen diffusion are solved in gas phase and liquid phase, respectively. Pisani [26] further compared five different porous structure of the catalyst layer. Lin et al [27] used thin-film agglomerate model to simulate the catalyst layer structure. For the agglomerate model analysis, an effectiveness factor is used to describe the ORR as follows

$$\nabla \cdot i = a i_h E \tag{1-15}$$

where E is the effectiveness factor. In spherical agglomerate, an analytic expression is shown as [28,29]

$$E = \frac{1}{3\phi^2}\left(3\phi \coth(3\phi) - 1\right) \tag{1-16}$$

where ϕ is the Thiele modulus for the system.

$$\phi = \zeta \sqrt{\frac{K}{D^{eff}_{O_{2,agg}}}} \tag{1-17}$$

where ζ is the characteristic length of the agglomerate, $R_{agg}/3$ for spheres, $R_{agg}/2$ for cylinders, and δ_{agg} for slabs, and K is a rate constant given by

$$K = \frac{a i_{ORR}}{4FC^{ref}_{O_2}} \exp\left(-\frac{\alpha_c F}{RT}\left(\eta_{ORR}\right)\right) \tag{1-18}$$

The governing equation for the agglomerate model without external mass-transfer limitation is expressed as

$$\nabla \cdot i = 4FC_{O_2}^{bulk}\left(\frac{1}{\dfrac{\delta_{film}}{A_{agg}D_{O_2,FILM}}+\dfrac{1}{KE}}\right) \tag{1-19}$$

Poisoning Effects by Impurity Ions and CO

Many researchers have focused their interest to investigate the effects of the impurities ions from both hydrogen fuel and air on the cell performance. Okada et al. [30-37] experimentally examined the water transport in the membrane of the fuel cell with the effects of various impurity ions. Water content, membrane conductivity, ionic transference coefficient, and diffusion coefficient of water decrease with an increase in the impurity ions. Okada [38,39] and Chen et al.[40] theoretically discussed the effect by impurity cations in membranes of PEM fuel cells. Okada [38,39] investigated the poisoning effect of impurity ions at the anode and cathode side, respectively. Operating current density and membrane thickness significantly affect the membrane performance. The most severe effects on the cell performance by the contaminant ions occur at the membrane-cathode interface. Chen [40] combined the theoretical model by Okada [38,39] to study the transient behavior of water transport in the membrane. The results show that contaminant ions enhance the electro-osmotic effect but decrease the diffusion of water from cathode. The steady state time t_{ss} decrease with the initial current density increase.

The most efficient fuel for use in a PEM fuel cell is pure hydrogen. However, this is difficult to store and has a high cost of production. Reforming from hydrocarbons, including gasoline and alcohol is the most extensively used technique for generating hydrogen fuel, which contain 45% hydrogen, 10ppm CO, 15% CO_2 and 1% CH_4 [1]. CO at a concentration even as low as 5-10 ppm effectively blocks Pt reaction sites for the electro-oxidation of hydrogen [2-3]. The affinity between CO and Pt is such that even at this low concentration of CO, the consequent loss of performance is severe [4-5]. Lee et al. [4] investigated the tolerance of PtSn/C, Pt/C and PtRu/C alloy electrocatalysts for CO. Depending on the nature of the electrode material, the CO oxidation occurs at different potentials. The improvement of CO tolerance is contributed by the changes in the thermodynamics and the CO adsorption process. Murthy et al. [5] presented the steady-state and transient performance of a fuel cell with relatively high concentrations of CO, for two types of gas diffusion media.

Recently, many efforts have been made to increase the tolerance of the PEM fuel cell to CO [41-46]. Schmidt et al. [41] and Divisek et al. [42] presented two methods for improving the cell performance using H_2/CO as a fuel. First, the use of Pt-Ru electrocatalysts at the anode can considerably enhance the tolerance to CO. Second, the addition of liquid hydrogen peroxide to the humidification water in the cell leads to the formation of active oxygen by the decomposition of H_2O_2. Complete recovery can be achieved for H_2/100 ppm CO. Si et al. studied the CO tolerance of the Pt-Ru/C catalyst at elevated temperature and atmospheric pressure in a PEM fuel cell [43]. They demonstrated that the anodic polarization fell dramatically as the temperature increased, because the CO coverage was lower. Improving the activity of the catalyst with a high CO tolerance increases the rates of reaction of CO and hydrogen. Zhang et al. [44] found that CO poisoning process can be accelerated at high anode flow rate. The performance decreases substantially as the anode flow rate increases, because CO is adsorbed on the catalyst site. However, increasing the anode overpotential promotes the oxidation of CO, maintaining desired cell performance. Yu et al. [45] and Santiago et al. [46] adopted the Pt-Ru/C electrocatalyst for different electrode structures to improve the tolerance of PEMFC to CO. Water sufficiently activates the Ru surface to promote the oxidation of CO. Xue et al. [47] developed a novel method to prepare the

Pt–Ru–P/C catalyst. The results show that Pt–Ru–P/C catalyst shows high activity for the methanol electro-oxidation. The greater oxidation of carbon monoxide also obtains compared with Pt–Ru/C catalyst. A PtRuIr/C catalyst was prepared by Liang et al [48] to exhibit excellent CO tolerance for PEM fuel cells. Ir in the PtRu electrocatalyst produces excellent activity of CO electro-oxidations. The superior performance is attributed by the interaction between RuO_2 and IrO_2.

To avoid the use of precious metal, some researchers adopted some methods to restore the cell performance during the operation process, including the oxidant-bleeding [49,50], self-oxidation [2,51], and current-pulsing [51,52]. Qi et al. [49] used cyclic voltammetry method to detect the CO adsorption on the cathode catalyst layer. The results show poisoning and recovering process is quickly within in 15 minutes. CO can pass through the membrane and poison the cathode catalyst. The potential drop at the cathode side is sometimes larger than anode. Well hydrated membrane can prevent CO crossover the membrane and increase the tolerance of CO. Adock et al. [50] used reconfigured anode (RCA) to enhance the air-bleed effectiveness for increase the CO tolerance of the fuel cell. A nonprecious-metal is place on the anode side adjacent to the flow field in order to perform preferential oxidations. Thomason et al. [51] compared both self-oxidation and current pulsing method for increasing the tolerance of CO. From the experimental results, current pulsing is more effective than self-oxidation in creasing the tolerance of CO. Carrette et al. [52] also used pulsing technique for determining the optimized operating conditions. Under various CO concentration, pulsing frequency need to be adjusted without significant performance loss.

Other researches have been developed to investigate the effect of hydrogen dilution in the anode feed [53, 54]. The effect of hydrogen dilution without CO containing fuel has been studied [53]. The predicted polarization curves showed a strong effect on cell performance. Gu [54] studied the dilution effect of N_2 and CO_2 individually. As a result of RWGS, CO_2/H_2 mixture has significantly larger polarization than N_2/H_2 mixture at the same concentration. Wee and Lee [55] established an overview of the development of CO tolerant electrocatalysts.

In theoretical studies, Springer et al. [56] derived a mathematical model to describe CO poisoning on the catalytic sites. Chan et al. [57] combined the theoretical models developed by Springer et al. [56] and Bernardi et al. [14,15] to examine the CO kinetics. Bhatia and Wang [58] treated the characteristics of the anode catalyst layer as a boundary condition in analyzing the transient CO poisoning behaviors for various levels of CO. Baschuk and Li [59] developed a mathematical model to simulate both CO poisoning and oxygen bleeding.

Recently, high temperature polybenzimidazole (PBI) membrane fuel cells have received great attentions. Wainright et al. [60] applied acid-doped PBI membrane for fuel cells. PBI is a basic polymer and exhibits high conductivity through doping with various acids or bases. Sulphuric acid and phosphoric acid are the most widely used doping matter to perform high conductivity. Wang et al. [61] demonstrated that the PBI membrane fuel cells performed well at 150^{o}C under atmosphere. After 200 hour operating, no membrane dehydration occurred. Li et al. [62] investigated phosphoric acid doped PBI membrane fuel cell in a various doping range. Acid doping level, water uptake, water drag coefficient and mechanical strength were all investigated. Proton conductivity of PBI and PBI composite membranes was measured by He et al. [63]. The conductivity could be influence by temperature, acid doping level and humidity. Li et al. [64] studied the influence of doping level and water uptake of PBI membrane fuel cells. Methanol permeation and proton conductivity of poly(N-methylbenzimidazole) (PNMBI), poly(N-ethylbenzimidazole) (PNEBI) and PBI were investigated by Pu et al. [65]. Ma et al. [66] made a complete set of membrane conductivity under various humidity, temperature and acid doping level. Liu et al. [67,68] investigated the O_2 reduction at a Pt-polymer electrolyte interface.

The operating temperature of acid-doped PBI membrane fuel cells is much higher than PFSA polymer membrane fuel cells. Several advantages make it superior to low temperature PEMFC. Firstly, operating temperature up to 200^{o}C can tolerate up to 3% CO in anode hydrogen fuel [69]. Dhar et al. [70,71] indicated that CO adsorption at platinum catalysts was easily occurred at low temperature. This makes it possible that the reformed gas can be fed directly into the fuel cell thus simplify the fuel cell system. Secondly, water managements such as liquid water flooding can be neglect at elevated temperature higher than boiling point of liquid water. He et al. [63] indicated that relative humidity is quite less influence on membrane conductivity of PBI membrane than Nafion membrane. Fuel cells work at high temperature can be made into a compact design with methanol reformer [72-76]. This is because nearly 100% conversion can be made around 200^{o}C through methanol steam reforming [75,76]. Reformed gas not only can be fed into the fuel cell directly but also provide a sufficient amount of heat for fuel cells. Park et al [74] developed a microchannel methanol steam reformer for fuel cells. As shown in Figure 1.11, microchannel reactors are integrated with the combustor, vaporizer, heat exchanger and steam reformer. Pan et al. [75] integrated a high temperature PBI membrane fuel cell with a methanol steam reformer as shown in Figure 1.12. The integration successfully improves the system construction and efficiency.

Several experiments have been made to analyze high temperature PBI membrane fuel cells. But there are only few of theoretical studies. Cheddie and Munroe [77] applied a one-dimensional model to predict the performance of PBI membrane fuel cells. Korsgaard et al [78] used a semi empirical model to approach the experimental data of polarization curves of PBI membrane fuel cells. However, there are still absent of theoretical investigations to realize the fundamental transportation inside the PBI membrane fuel cells.

1.4 Objectives

In the present study, our purpose is to analyze how carbon monoxide poisoning affects the performance and durability of a PEM fuel cell. First, we develop a one-dimensional transient mathematical model to simulate the carbon monoxide poisoning effect of the PEM fuel cell. Because of the transient evolution of the CO poisoning is not well understood. This study focuses on the transient behavior of CO poisoning process across the anode catalyst layer and the response time to reach steady state t_{ss}. Hydrogen and CO adsorption on the catalyst site explain how CO results in a less available catalyst site for hydrogen electro-oxidation.

Second, we develop a one-dimensional, two-phase theoretical model to analyze the CO poisoning effect of a fuel cell. We discuss the transport of water, fuel and oxidant in the MEA of PEM fuel cells based on two-phase modeling. Both vapor and liquid water transport are discussed inside the cell. The slowing of the chemical reactions at both the anode and the cathode can influence the liquid water distribution in the catalyst layers and membrane. The effects of dilute hydrogen feed are also discussed.

Third, a transient mathematical model is extended from our previous two-phase model to analyze how CO poisoning affects the PEM fuel cell. This is because that there is no existing study which shows the transient evolution of liquid water transport under CO poisoning process. This work tries to make some contribution in the scientific understanding on the effect of CO poisoning in PEM fuel cells. The time to reach steady state t_{ss} is discussed under various operating cell voltage and the amount of pure hydrogen to promote the tolerance for CO.

Finally, an experimental apparatus has been built to investigate high temperature PBI membrane fuel cells. The operating temperature of acid-doped PBI membrane fuel cells is much higher than PFSA polymer membrane fuel cells. Our objectives are to investigate the performance of PBI membrane fuel cells under various fuel compositions from both simulation and experiments. Effects of temperature, CO content and hydrogen concentration on the cell performance and t_{ss} are all investigated. The transportations of hydrogen coverage, CO coverage on the platinum catalysts and the ionic potential loss across the MEA were shown in our simulation results.

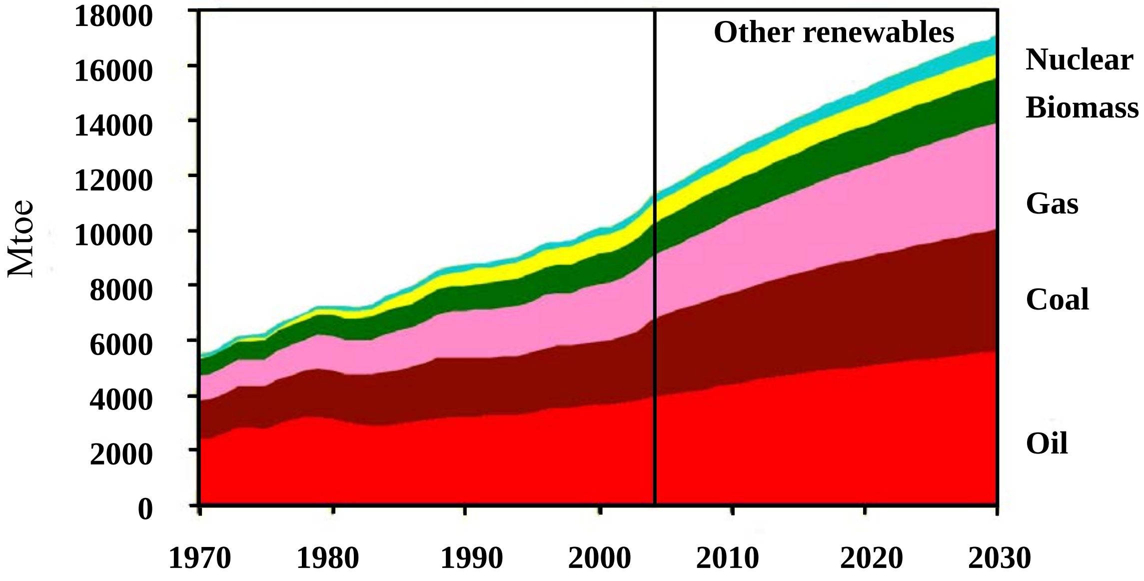

Fig 1.1 Energy demand of the world between 1970 to 2030 (IEA, 2006)

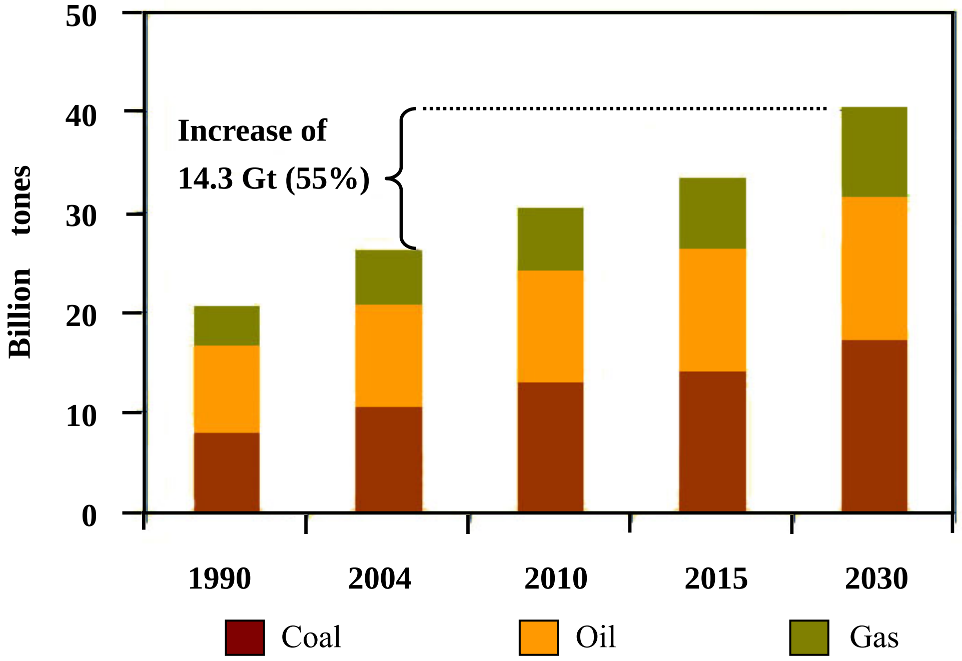

Fig 1.2 CO_2 emissions by fuel grow 55% between 1990 to 2030 (IEA, 2006)

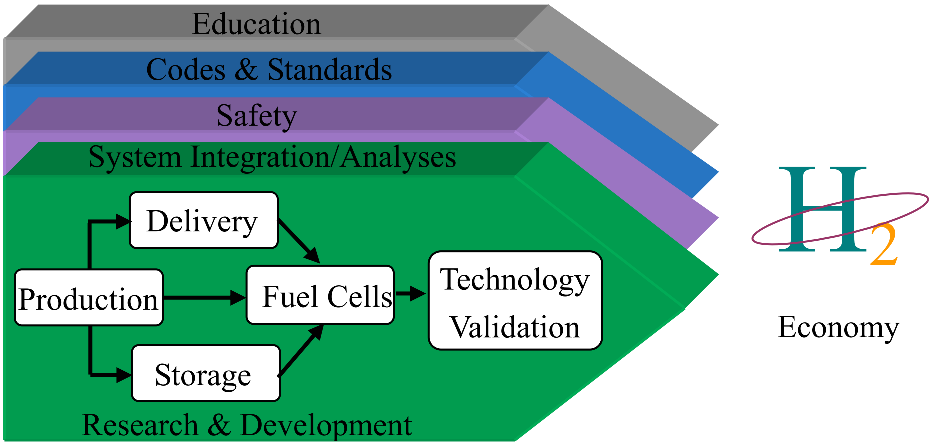

Fig 1.3 The hydrogen, fuel cells & infrastructure technologies program [EERE / DOE, 2006]

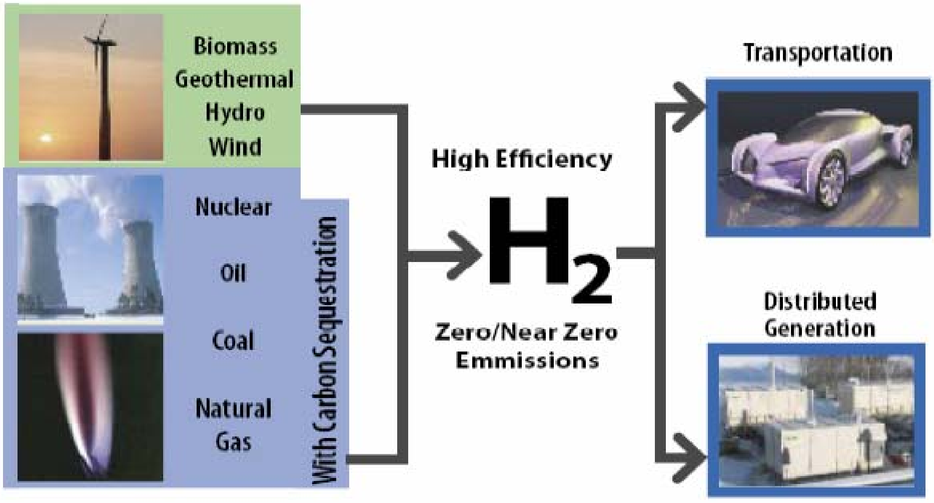

Fig 1.4 A domestic hydrogen energy system [EERE / DOE, 2005]

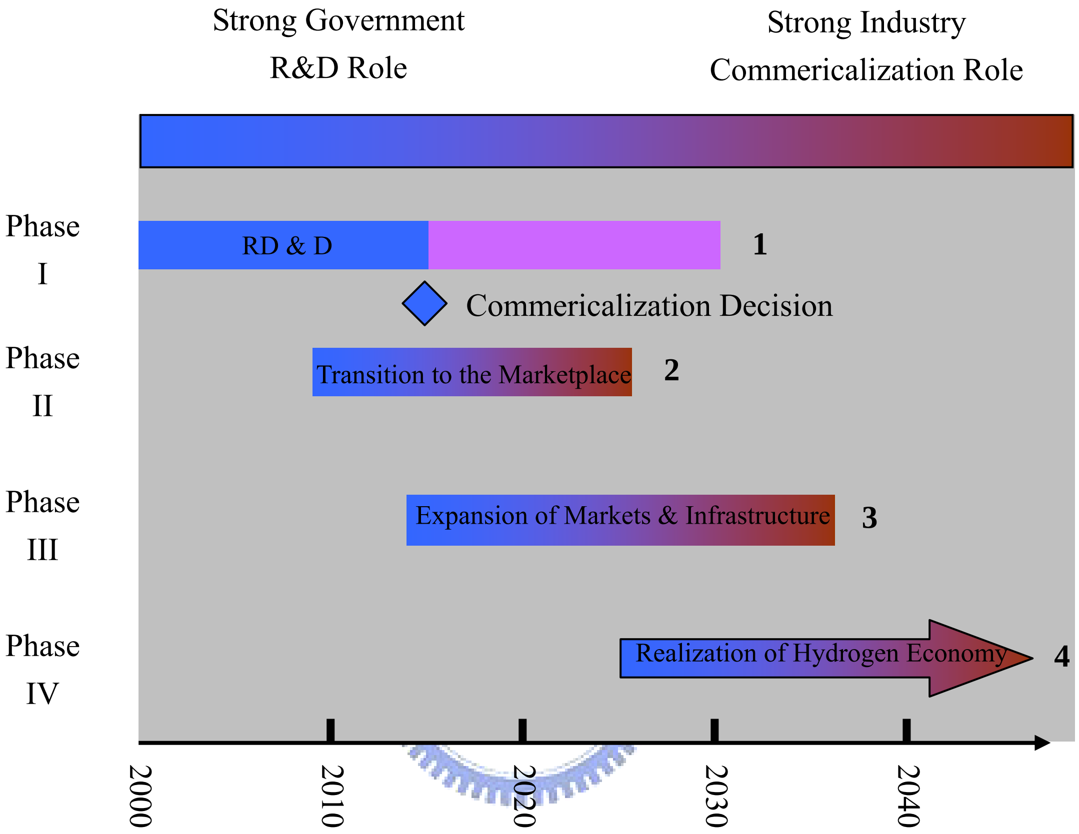

Fig 1.5 Hydrogen economy timeline [EERE / DOE, 2005]

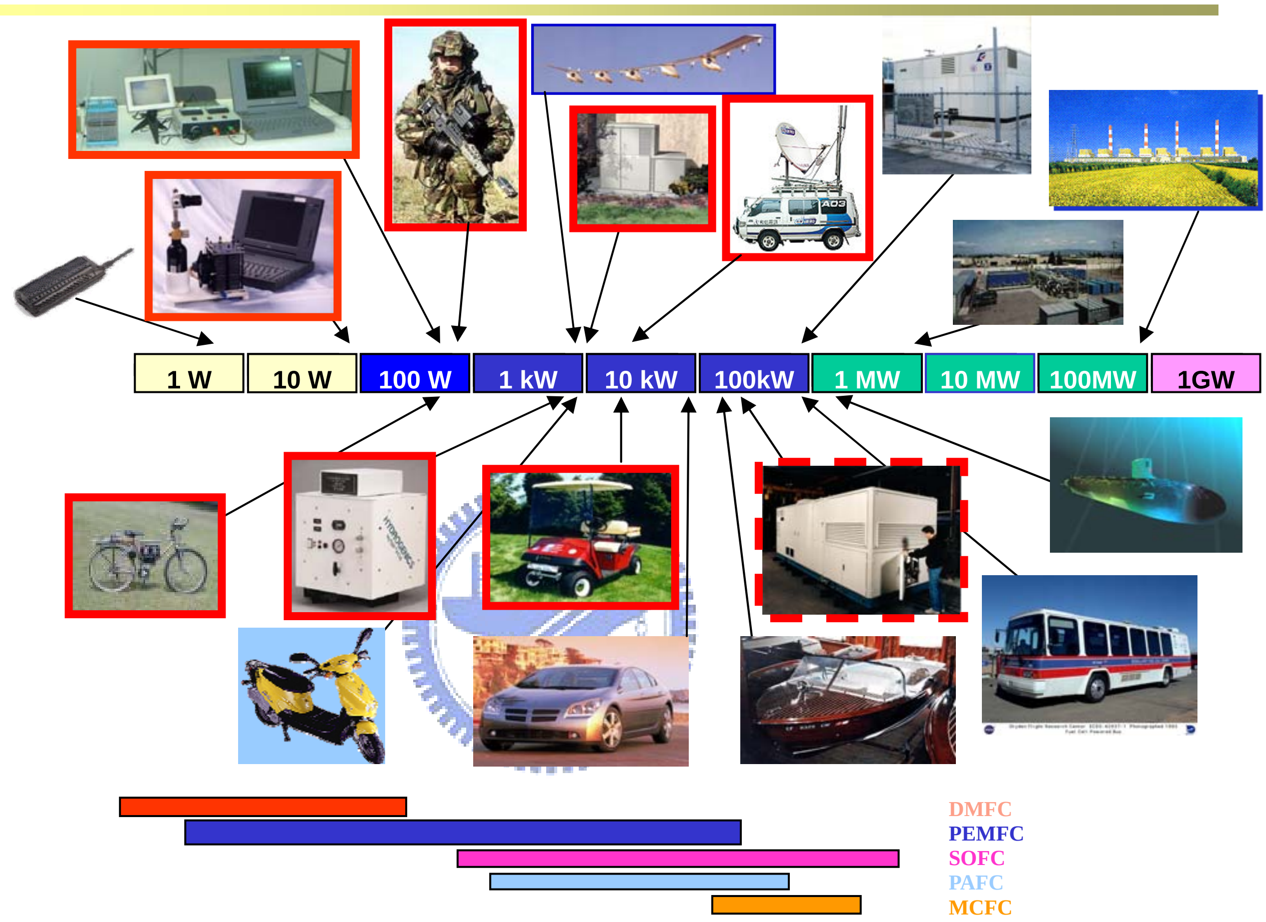

Fig 1.6 Applications of the fuel cell (ERL/ITRI)

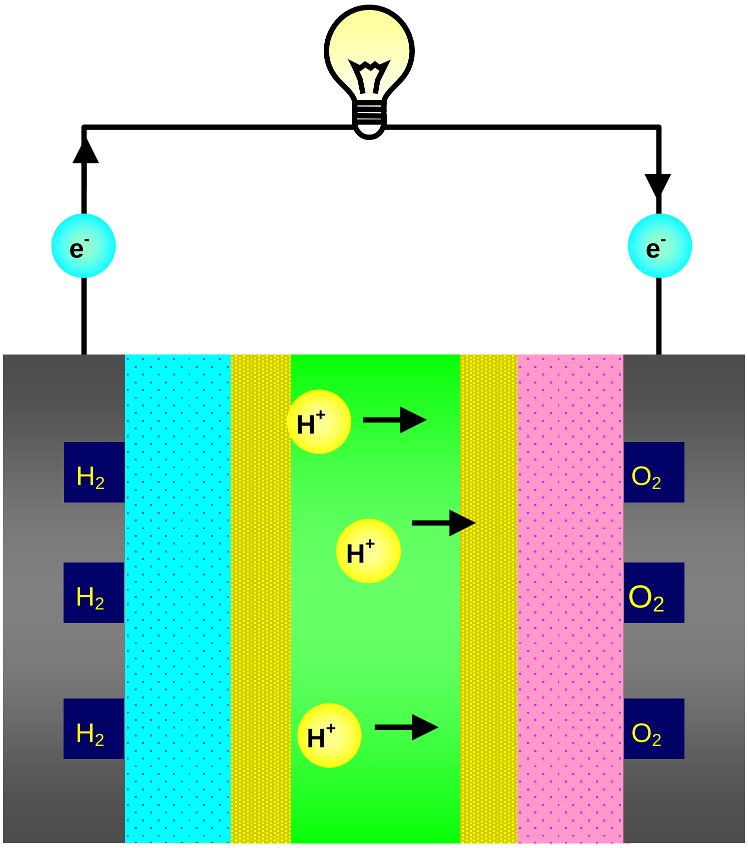

Fig 1.7 Schematic diagram of a PEM fuel cell

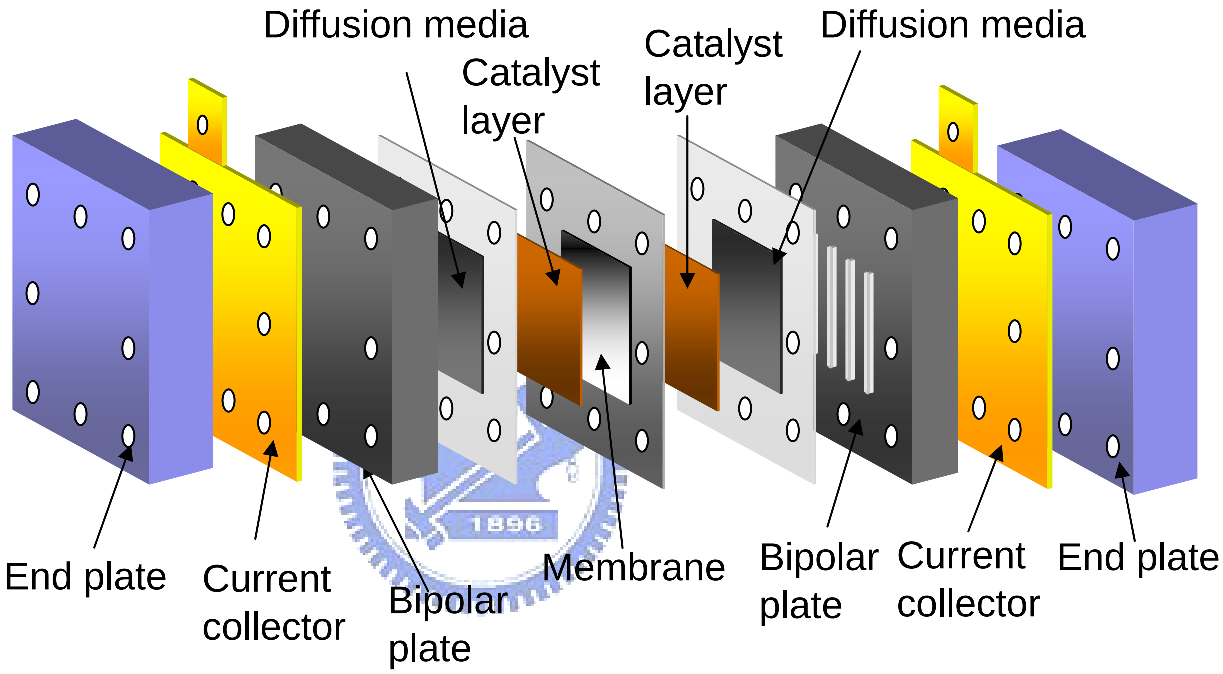

Fig 1.8 Component diagram of a PEM fuel cell

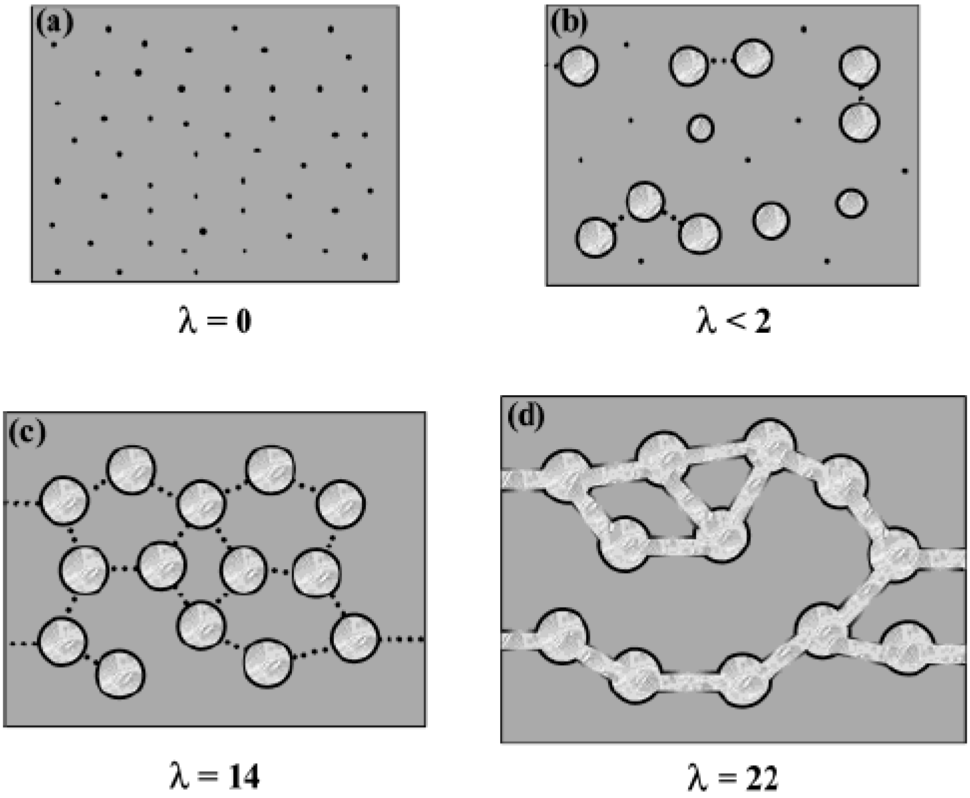

Fig 1.9 Structure of the membrane as a function of water content [11]

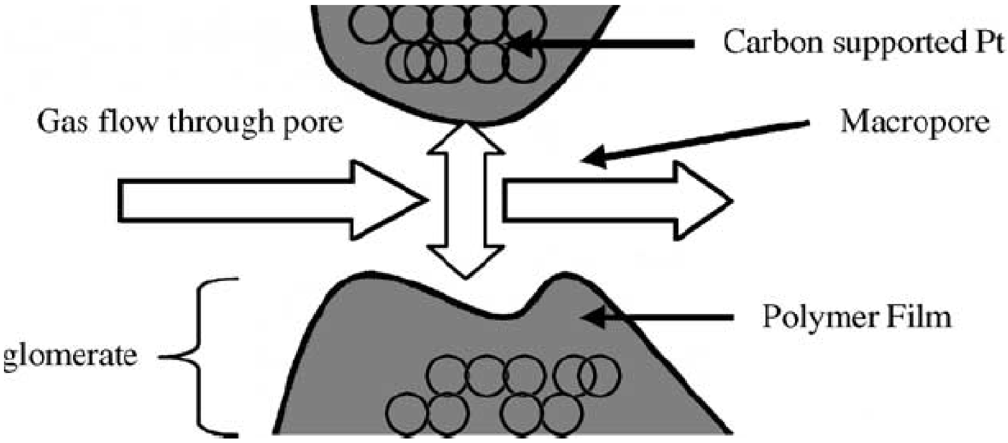

Fig 1.10 Schematic diagram of the agglomerate catalyst [13]

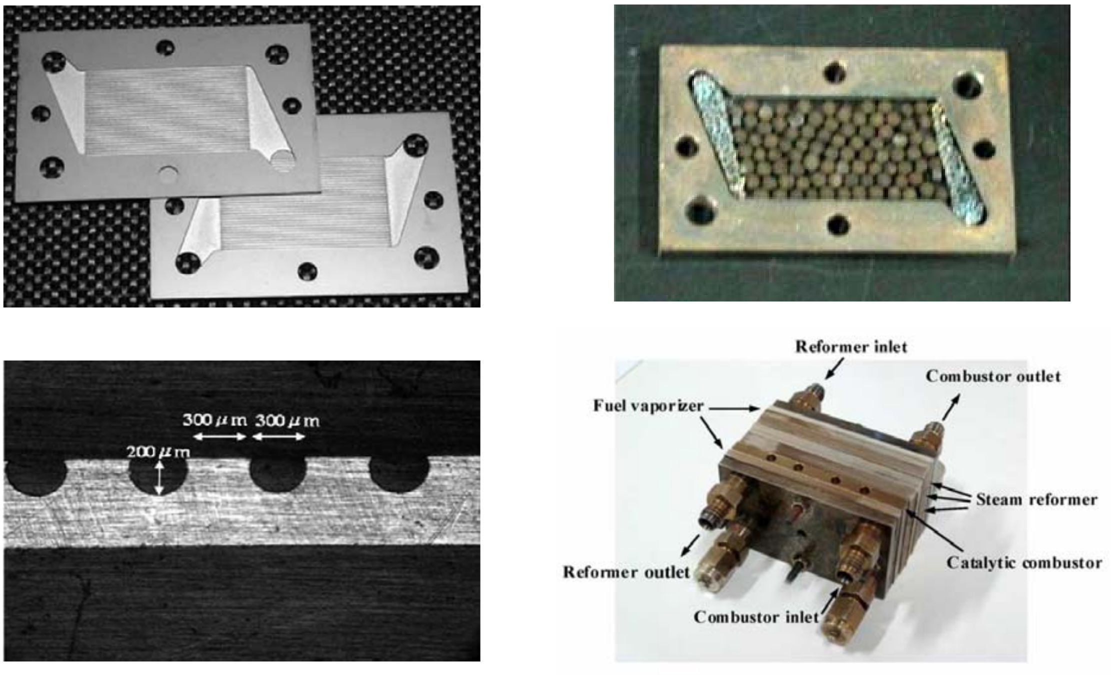

Fig. 1.11. Methanol fuel processor [74].

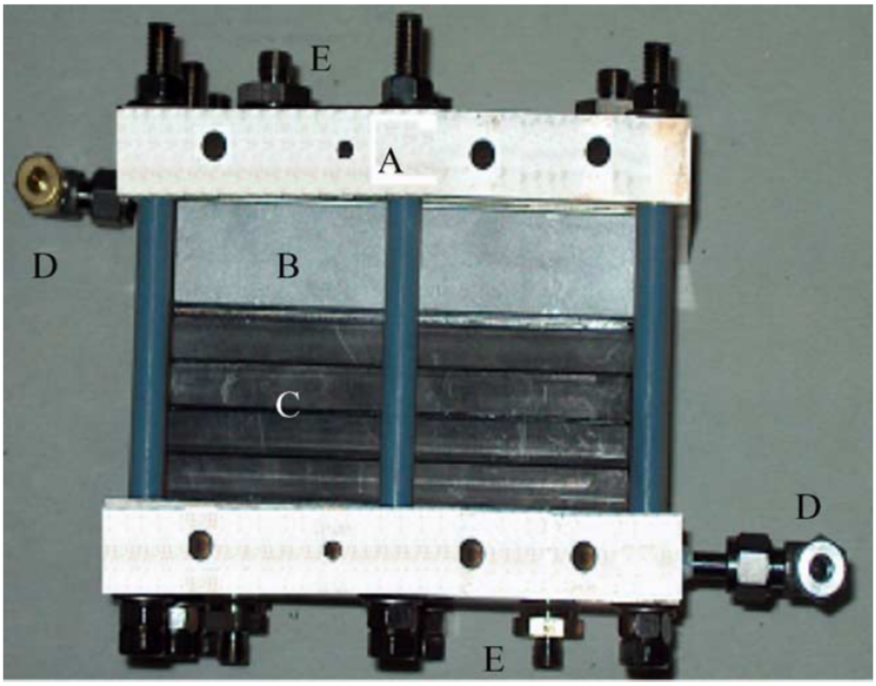

Fig 1.12 A PBI cell stack with an integrated methanol reformer [75]

2. Transient Behaviors of CO Poisoning in the Anode Catalyst Layer

A one-dimensional transient mathematical model is applied to simulate the carbon monoxide poisoning effect on the performance of the PEM fuel cell. Based on the CO kinetic model developed by Springer et al. [56], the transient behaviors of CO poisoning process across the anode catalyst layer is investigated. Several physical parameters are considered to promote the tolerance for CO and analyze the influence on the response time to reach steady state t_{ss}. The transient behavior of hydrogen and CO transport are also investigated. In this chapter, an anode catalyst layer of thickness L_c is considered, as schematically shown in Fig. 2.1. Some basic assumptions were made as following:

1. Unsteady state.
2. One dimension, isothermal.
3. Ideal gas.
4. Catalyst layer is isotropic.
5. Only diffusion mechanism is considered.
6. Hydrogen and carbon monoxide were considered in the catalyst layer.
7. Anode overpotential is constant.
8. Liquid water is neglected.

2.1 Theoretical Model

Consider an anode catalyst layer of thickness L_c, as schematically shown in Fig. 2.1. Transient analysis of CO poisoning behaviors across the anode catalyst layer is investigated. The theoretical model of CO kinetics proposed by Springer et al. [56]

was adopted in this work. For hydrogen, CO, and Pt interfacial kinetics, four expressions are described as follows

$$H_2 + 2Pt \overset{k_{fH}}{\underset{b_{fH}k_{fH}}{\leftrightarrow}} 2(H - Pt) \tag{2-1}$$

$$CO + Pt \overset{k_{fc}}{\underset{b_{fc}k_{fc}}{\leftrightarrow}} (CO - Pt) \tag{2-2}$$

$$(CO - Pt) + H_2O \overset{k_{ec}}{\rightarrow} Pt + CO_2 + 2H^+ + 2e^- \tag{2-3}$$

$$H - Pt \overset{k_{eH}}{\rightarrow} Pt + H^+ + e^- \tag{2-4}$$

Hydrogen dissociative chemisorption and the CO adsorption on the Pt catalyst sites are described by the Eq. (2-1) and Eq. (2-2), respectively. In the above equations, The Eq. (2-3) and Eq. (2-4) represent the CO and hydrogen electro-oxidation, respectively. Under the time-dependent conditions, Eq. (2-5) and Eq. (2-6) describe the first order transient process of adsorption, desorption and charge fluxes.

$$\xi \frac{d\theta_{H_2}}{dt} = k_{fH} X_{H_2} P(1 - \theta_H - \theta_{CO}) - b_{fH} k_{fH} \theta_{H_2} - 2k_{eH} \theta_{H_2} \sinh\left(\frac{n_{H_2} F \eta}{2RT}\right) \tag{2-5}$$

$$\xi \frac{d\theta_{CO}}{dt} = k_{fCO} X_{CO} P(1 - \theta_H - \theta_{CO}) - b_{fCO} k_{fCO} \theta_{CO} - 2k_{eCO} \theta_{CO} \sinh\left(\frac{n_{CO} F \eta}{2RT}\right) \tag{2-6}$$

where θ_{H_2} and θ_{CO} denote the fraction of catalyst site cover by hydrogen and CO, respectively. The forward rate constant of hydrogen and CO adsorption-to-desorption rate ratios are expressed as k_{fH} and b_{fc}, which are functions of CO coverage ratio and expressed as follows:

$$k_{fH} = k_{fH0} \cdot \exp\left[-\frac{\delta(\Delta E_H)}{RT}\left(1 - \exp\left(\frac{\lambda \theta_{CO}}{\theta_{CO} - 1}\right)\right)\right] \tag{2-7}$$

$$b_{fCO} = b_{fCO0} \cdot \exp\left[\frac{\delta(\Delta G_{CO})}{RT} \theta_{CO}\right] \tag{2-8}$$

Unsteady transport equations for H_2 and CO across the anode catalyst layer can be written as:

$$\varepsilon_{CL}\frac{\partial C_{H_2}}{\partial t}=\varepsilon_{CL}D_{H_2}\frac{\partial^2 C_{H_2}}{\partial x^2}-\frac{di_{H_2}}{dx}\left(\frac{\gamma_{H_2}}{n_{H_2}F}\right) \tag{2-9}$$

$$\varepsilon_{CL}\frac{\partial C_{CO}}{\partial t}=\varepsilon_{CL}D_{CO}\frac{\partial^2 C_{CO}}{\partial x^2}-\frac{di_{CO}}{dx}\left(\frac{\gamma_{CO}}{n_{CO}F}\right) \tag{2-10}$$

Where ε_{CL} stands for the gas porosity, D_{H_2} and D_{CO} denote the diffusion coefficient of hydrogen and CO, respectively. s is the stoichiometric coefficient, n is the number of electrons, F is Faraday constant, and $\frac{di}{dx}$ is the electro-chemical reactions which are described by Eq. (2-11). Subscripts H_2 and CO represent the hydrogen and carbon monoxide, respectively. The operating current density is then:

$$\frac{di}{dx}=\frac{di_{H_2}}{dx}+\frac{di_{CO}}{dx}=2ak_{eH}\theta_{H_2}\sin\left(\frac{n_{H_2}F\eta}{2RT}\right)+4ak_{eCO}\theta_{CO}\sinh\left(\frac{n_{CO}F\eta}{2RT}\right) \tag{2-11}$$

To investigate the transient behaviors of the reactant gases distributions and coverage ratio distributions across the anode catalyst layer, the initial conditions are all set from zero which expressed as follows:

$$C_{H_2}(x,0)=C_{H_2}^0 \tag{2-12}$$

$$C_{CO}(x,0)=C_{CO}^0 \tag{2-13}$$

$$\theta_{H_2}(x,0)=\theta_{H_2}^0 \tag{2-14}$$

$$\theta_{CO}(x,0)=\theta_{CO}^0 \tag{2-15}$$

At the boundary x=0, the hydrogen and CO are given a fixed amount of concentration. The interface between the anode catalyst layer and the membrane (x=L_c), the flux of reactant gases equal to zero. The corresponding boundary conditions are illustrated as follows:

$$C_{H_2}=C_{H_2}^{in}(0,t) \tag{2-16}$$

$$C_{CO} = C_{CO}^{in}(0,t) \tag{2-17}$$

$$D_{H_2}\frac{\partial C_{H_2}}{\partial x} = 0(L_c,t) \tag{2-18}$$

$$D_{CO}\frac{\partial C_{CO}}{\partial x} = 0(L_c,t) \tag{2-19}$$

Because of no electro-oxidation occurs at the interface between the anode gas diffusion layer and the anode catalyst layer, the current density is set to be zero.

$$i = 0 \tag{2-20}$$

2.2 Numerical Method

The equations (2-9) and (2-10) for H_2 and CO are the parabolic partial differential equations. In this study, governing equations were solved by using implicit method. The above equations can be rewritten as

$$\varepsilon_{CL}\frac{C_{H_2,i}^{n+1} - C_{H_2,i}^{n}}{\Delta t} = \varepsilon_{CL}D_{H_2}\frac{C_{H_2,i+1}^{n+1} - 2C_{H_2,i}^{n+1} + C_{H_2,i+1}^{n+1}}{\Delta x^2} - \frac{di_{H_2,i}}{dx}\left(\frac{\gamma_{H_2}}{n_{H_2}F}\right) \tag{2-21}$$

$$\varepsilon_{CL}\frac{C_{CO,i}^{n+1} - C_{CO,i}^{n}}{\Delta t} = \varepsilon_{CL}D_{CO}\frac{C_{CO,i+1}^{n+1} - 2C_{CO,i}^{n+1} + C_{CO,i+1}^{n+1}}{\Delta x^2} - \frac{di_{CO,i}}{dx}\left(\frac{\gamma_{CO}}{n_{CO}F}\right) \tag{2-22}$$

The 4th order Runge Kutta algorithm were applied to solved the coverage of H_2 and CO. The governing equations must be solved simultaneous for the dependent variables. The steady-state condition is defined as the relative error reaches:

$$\frac{C_i^{n+1} - C_i^{n}}{C_i^{n}} \le 10^{-8} \tag{2-21}$$

in which C_i^n represents any variables at *n*th time step.

2.3 Results and Discussion

To examine the transient behaviors of the poisoning process, various CO concentrations are employed to simulate a wide range of hydrogen fuel from the reformer. Several physical parameters are considered to analyze the reactant gas distribution, coverage, current density, and the time response needed to reach the steady state condition after a the start-up operation. Table 2.1 presents the parameters used in this work.

Transient evolutions of the hydrogen and CO distributions across the anode catalyst layer with 100 ppm CO are shown in Fig. 2.2. Because of the fast kinetics of hydrogen, the current density was provided by hydrogen electro-oxidation resulting much lower concentration profiles. In contrast, the concentration distribution of CO was only depleted slightly across the anode catalyst layer. As a result, both the hydrogen and the CO concentrations take 541 s to reach the steady-state condition after a start-up operation.

The transient distributions of the hydrogen coverage across the anode catalyst layer for 100 ppm CO are indicated in Fig.2.3. It is clearly seen that the hydrogen coverage, θ_H, decreases with the time due to the CO adsorption on the catalyst site. Owing to the high affinity between CO and Pt catalyst, large anode overpotential is needed to oxidize CO. As shown in Fig. 2.4, the catalyst site is adsorbed by the CO when the reacting time goes. This causes the hydrogen to diffuse deeply into the catalyst layer, which in turn, seeks for more catalyst sites. Without extremely high overpotential to make the CO oxidation, the accumulation of CO on the catalyst site is sustained and therefore reduces the hydrogen oxidation.

Figure 2.5 shows the unsteady variations of the hydrogen oxidation current density across the anode catalyst layer. It is observed in Fig. 2.5 that the hydrogen oxidation increases sharply after the start-up operation (within the first 2 μm). Comparison of the corresponding hydrogen concentration distributions in Fig. 2.2 indicates that the fast kinetics of hydrogen results in a significant increase in the hydrogen oxidation current. In Fig. 2.6, the CO oxidation current is in the order of 10^{-8} A cm^{-2} which is much smaller than the hydrogen oxidation current. This implies that the CO oxidation current can be neglected.

Under various levels of the CO concentration from the reformer, the cell performance decreases with an increase in the CO concentration. Figure 2.7 shows the steady-state hydrogen coverage under various CO concentrations in the range between 10~100 ppm. It is seen that the fuel with a high CO level would reduce the hydrogen coverage on the catalyst sites which can reduce the cell current density significantly. Otherwise, a significant rise in the θ_{CO} from 0.5 to 0.94 at the range from 10-100 ppm CO is found in Fig. 2.8.

Figure 2.9 presents the total cell current density distributions across the anode catalyst layer under various ppm CO. The predicted CO poisoning results are compared with the experimental data of Oetjen et al. [79]. The current density nearly 1 A cm^{-2} was obtained at η=0.01 in present result without CO contained. The experimental data were subjected to different CO concentration polarization curve at 0.6 V which corresponds to CO-free at current density 1 A cm^{-2}. As shown in Fig 2.9, the results show a good agreement with experimental data. A careful examination of Fig. 2.9 discloses that the current density would decrease from 1. A cm^{-2} to, 0.487, 0.365 or 0.263 A cm^{-2} when the hydrogen is subjected to 25, 50 or 100 ppm CO, respectively. The predicted steady-state current density under different ppm CO is consistent with those of Oetjen [79].

As mentioned above, the hydrogen with various CO concentration not only drops the cell current density but also affects the response time interval t_{ss}. Figure 2.10 shows the effects of the ppm CO on the response time interval t_{ss} for different anode overpotential and gas porosity. An overall inspection of Fig. 2.10 indicates that the ppm CO has a significant impact on the response time interval. This is because that the hydrogen with a high CO concentration would increase the CO adsorption on the catalyst sites, which in turn, cause a decrease in the response time interval t_{ss}. While the overpotential and gas porosity have a slight influence on the response time interval. In addition, the response time interval decreases with an increase in the ppm CO.

Figure 2.11 presents the variations of current density with CO concentration under different anode overpotential and gas porosity. It is seen that with a higher anode overpotential or gas porosity at the catalyst layer can obtain a much greater current density, especially at low CO concentration. This can be made plausible by noting the fact that the catalyst layer with a high porosity, the hydrogen fuel can be easily fed into the catalyst layer and high anode overpotential can free up the catalyst reacting sites for hydrogen oxidation by bringing about the great CO oxidation. With 0.01 V anode overpotential and 10 ppm CO, the corresponding current density is 0.79 A cm^{-2} and 0.6 A cm^{-2} for the porosity being 0.5 and 0.3, respectively. But, when the CO concentration is increased, the effects of the gas porosity on the current density would become less significant. A similar trend can be obtained for the case with overpotential 0.005V at the same gas porosity under various CO concentrations.

Table 2.1 Values of parameters used in the present study [15,56].

T	353 K
P	3 atm
α	0.5
D_{H2}	2.59×10^{-6} cm^2 s^{-1}
k_{fH0}	100 A cm^{-2} atm
b_{fH}	0.5
k_{eH}	4 A cm^{-2}
k_{ECO}	10 A cm^{-2} atm
b_{fCO}	1.51×10^{-9} atm
k_{eCO}	1×10^{-8} A cm^{-2}

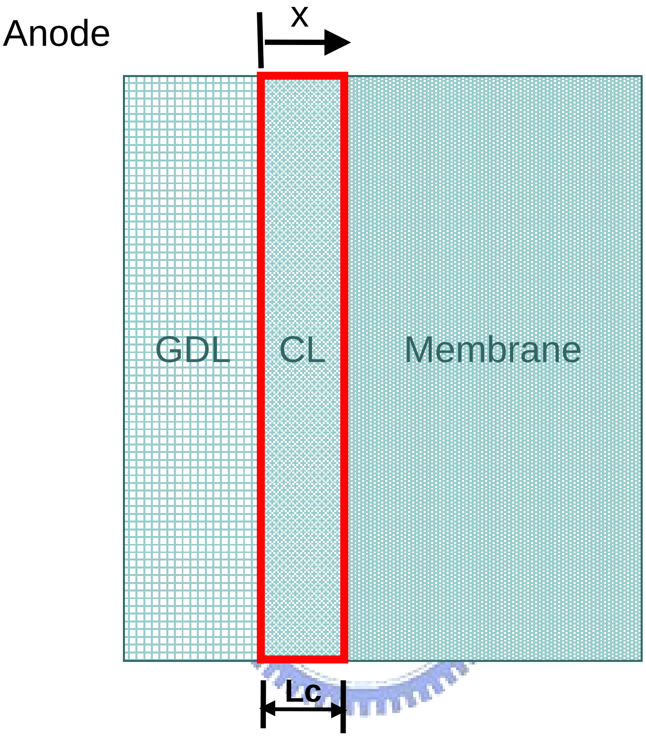

Fig. 2.1 Schematic diagram of a PEM fuel cell anode.

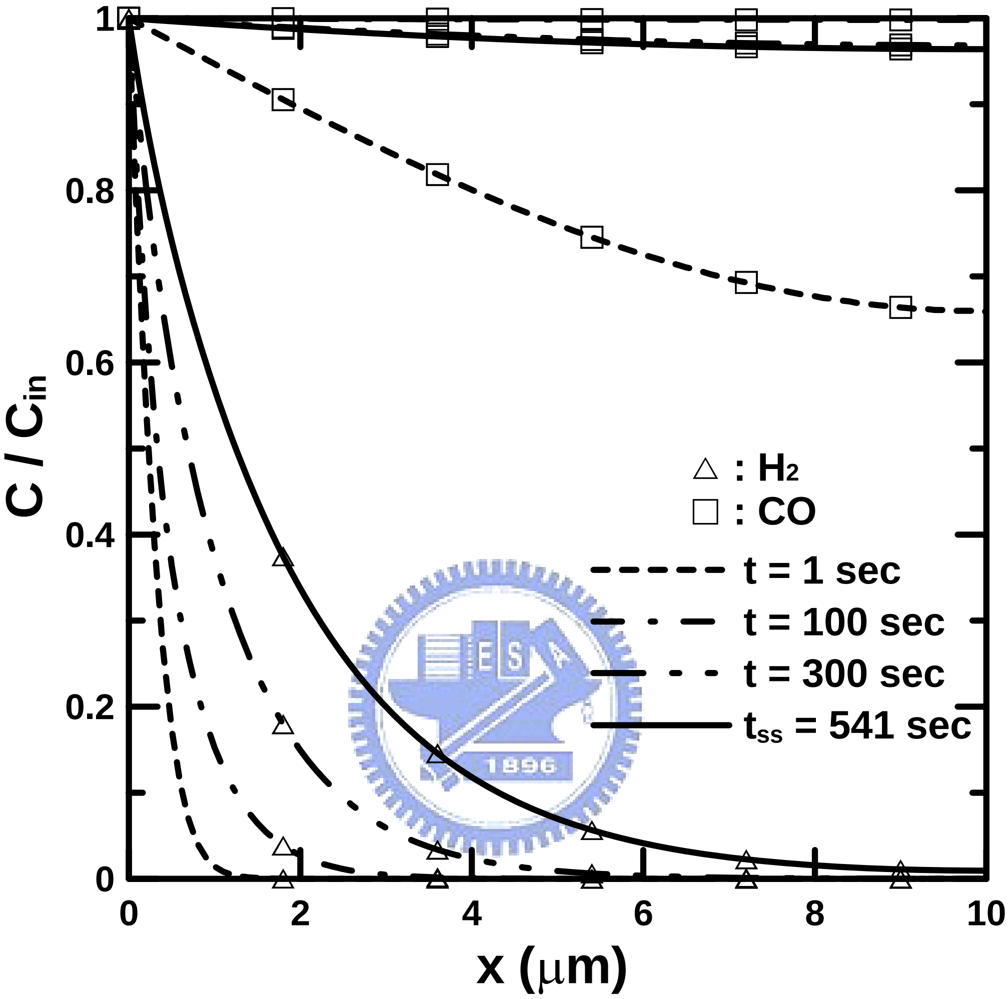

Fig. 2.2 Hydrogen (△) and carbon monoxide (□) distributions at various time steps across anode catalyst layer for 100 ppm CO, ε_{CL}=0.4, η=0.01, and L_c=10μm.

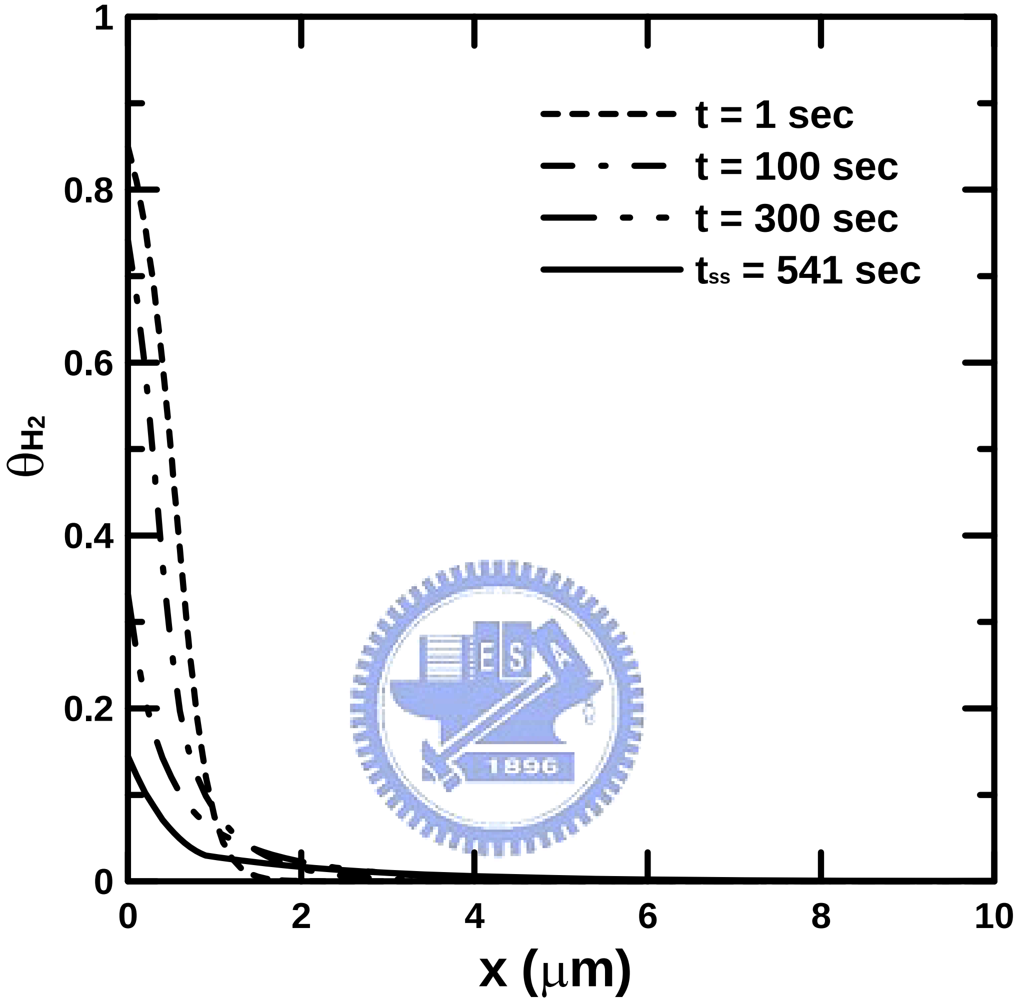

Fig. 2.3 Distributions of θ_{H_2} at various time steps across anode catalyst layer for 100 ppm CO, ε_{CL}=0.4, η=0.01, and L_c=10μm.

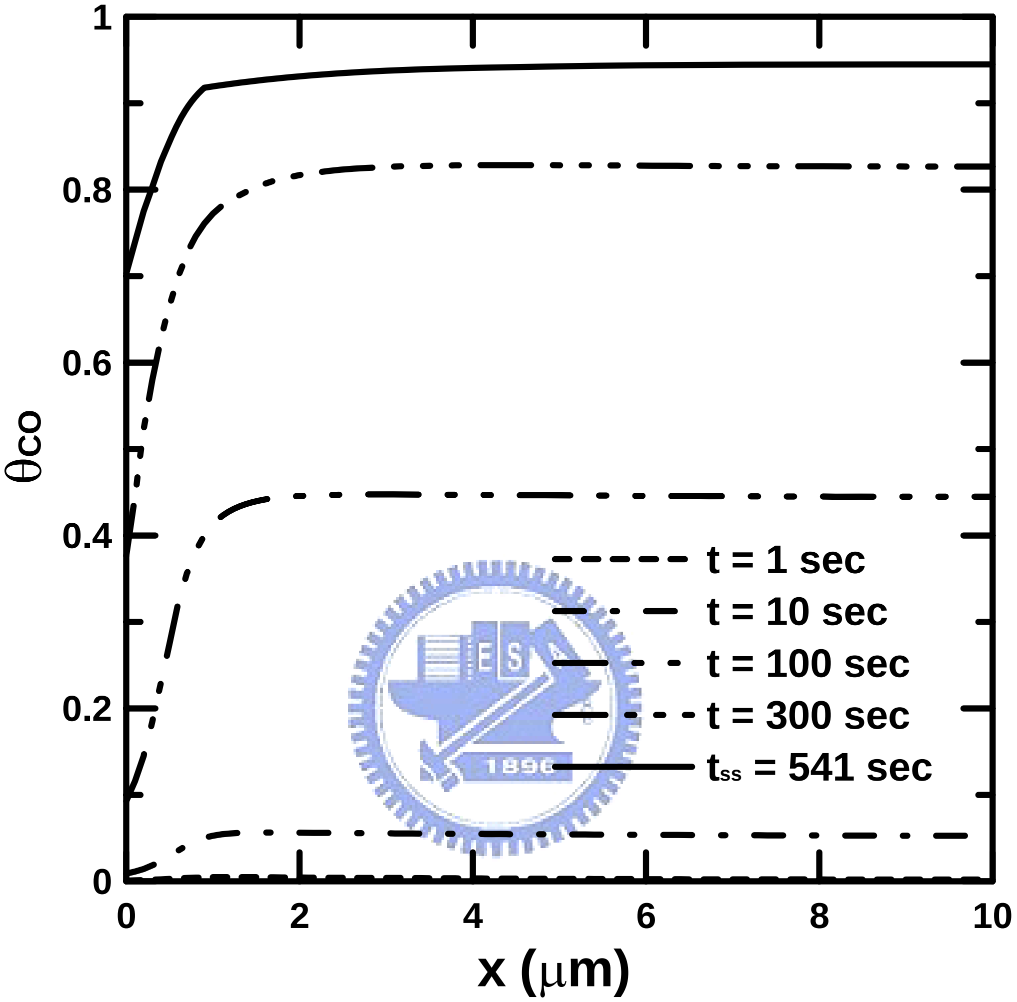

Fig. 2.4 Distributions of θ_{CO} at various time steps across anode catalyst layer for 100 ppm CO, ε_{CL}=0.4, η=0.01, and L_c=10μm.

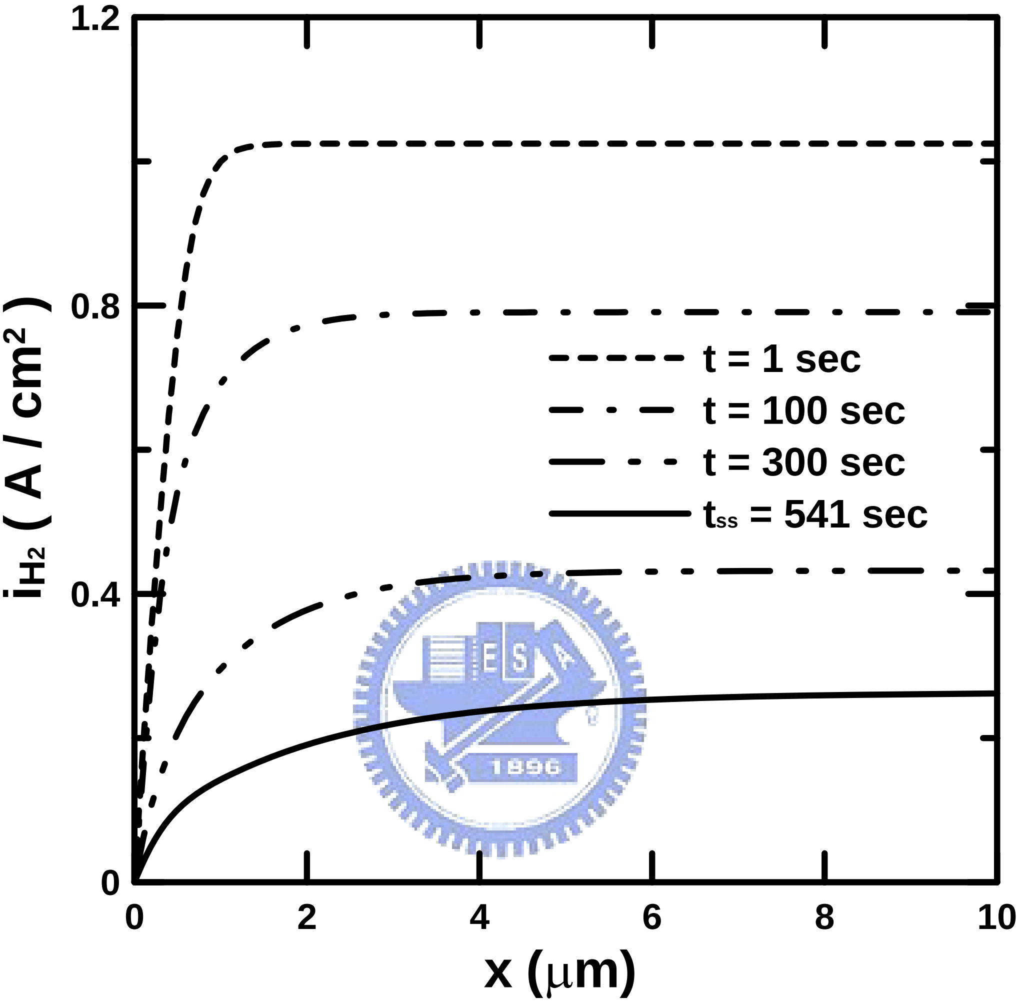

Fig. 2.5 Distributions of hydrogen oxidation current at various time steps across anode catalyst layer for 100 ppm CO, ε_{CL}=0.4, η=0.01, and L_c=10μm.

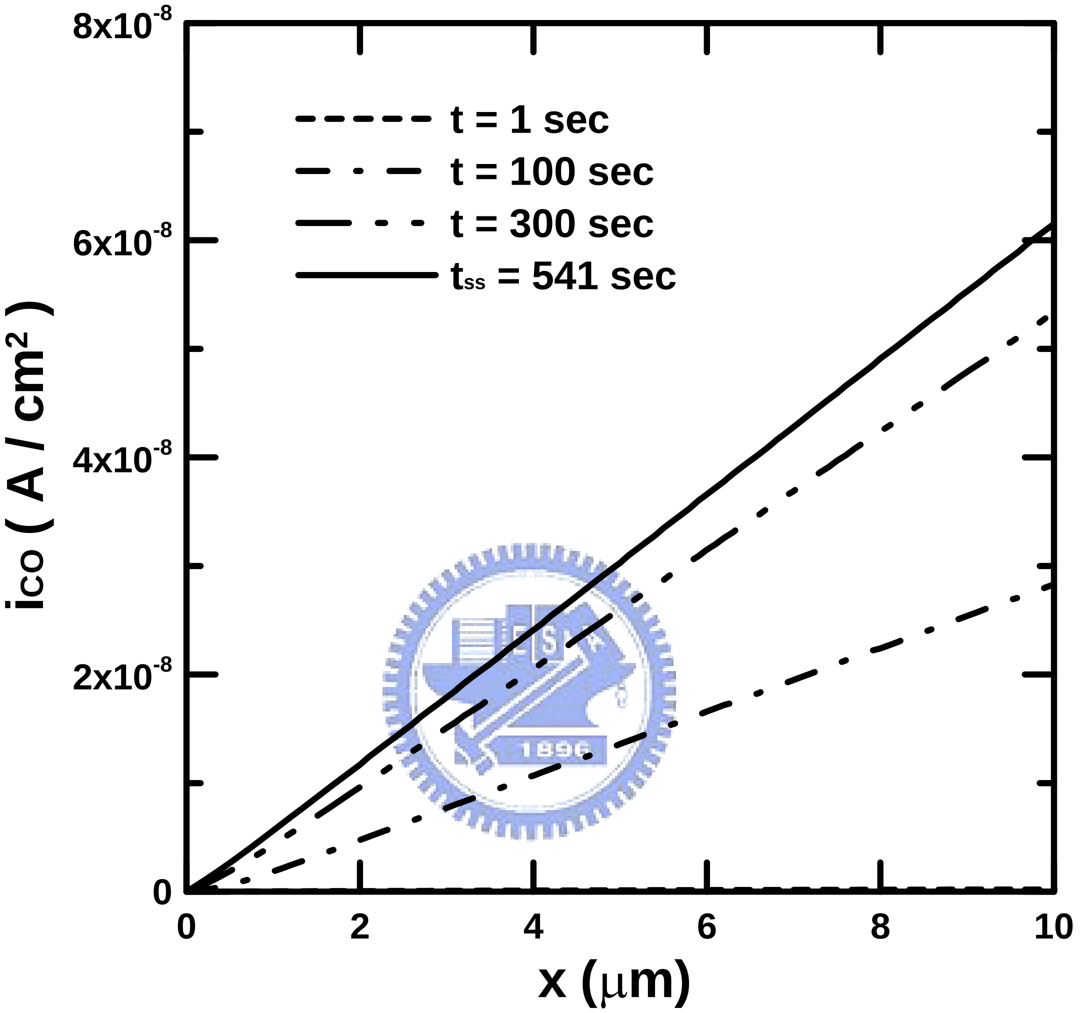

Fig. 2.6 Distributions of CO oxidation current at various time steps across anode catalyst layer for 100 ppm CO, ε_{CL}=0.4, η=0.01, and L_c=10μm.

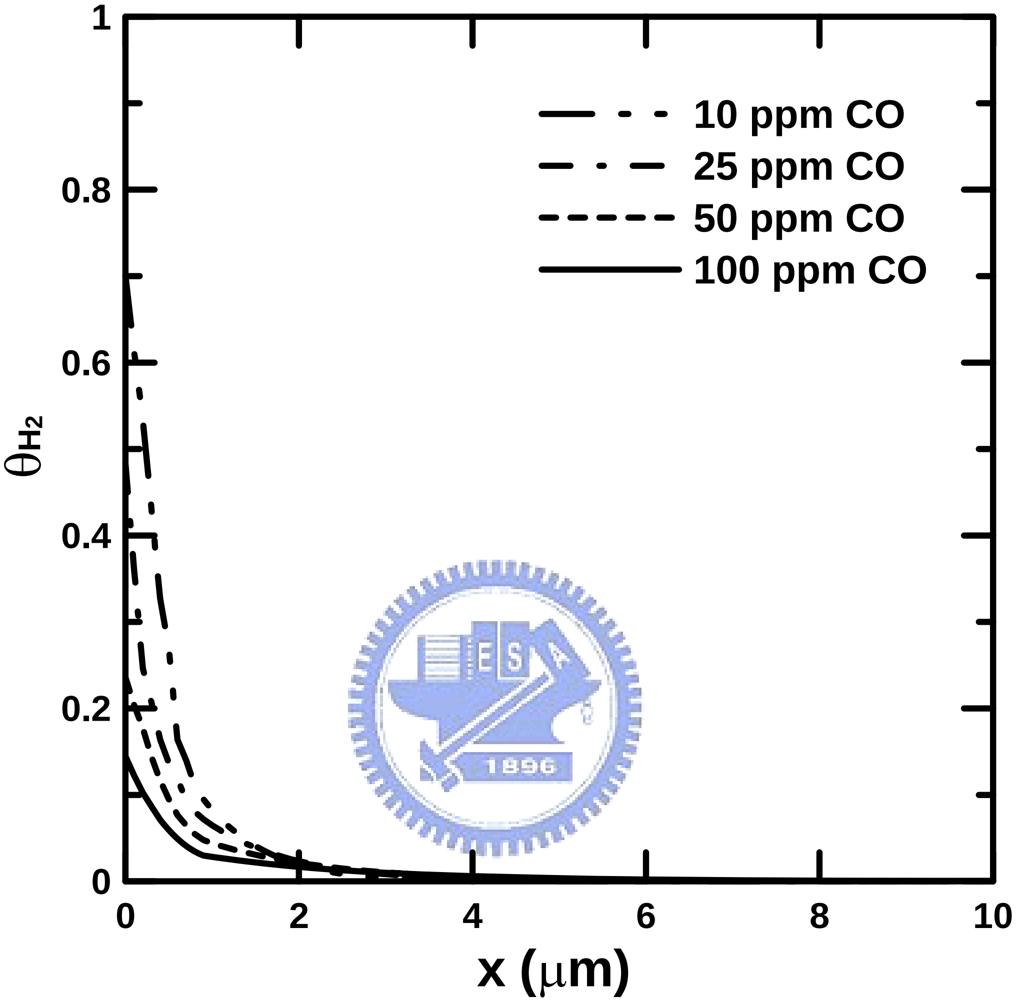

Fig. 2.7 Distributions of θ_{H_2} at steady state across anode catalyst layer for different CO concentration with ε_{CL}=0.4, η=0.01, and L_c=10μm.

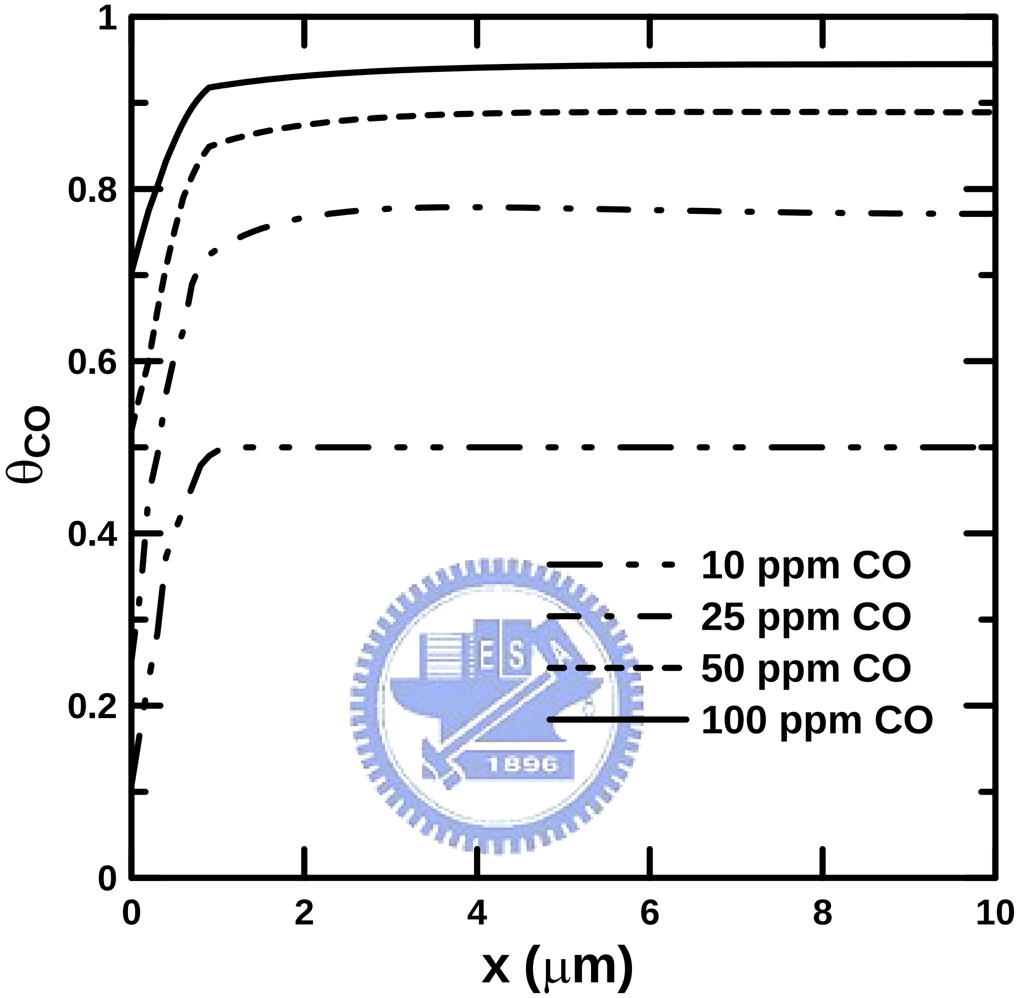

Fig. 2.8 Distributions of θ_{CO} at steady state across anode catalyst layer for different CO concentration with ε_{CL}=0.4, η=0.01, and L_c=10μm.

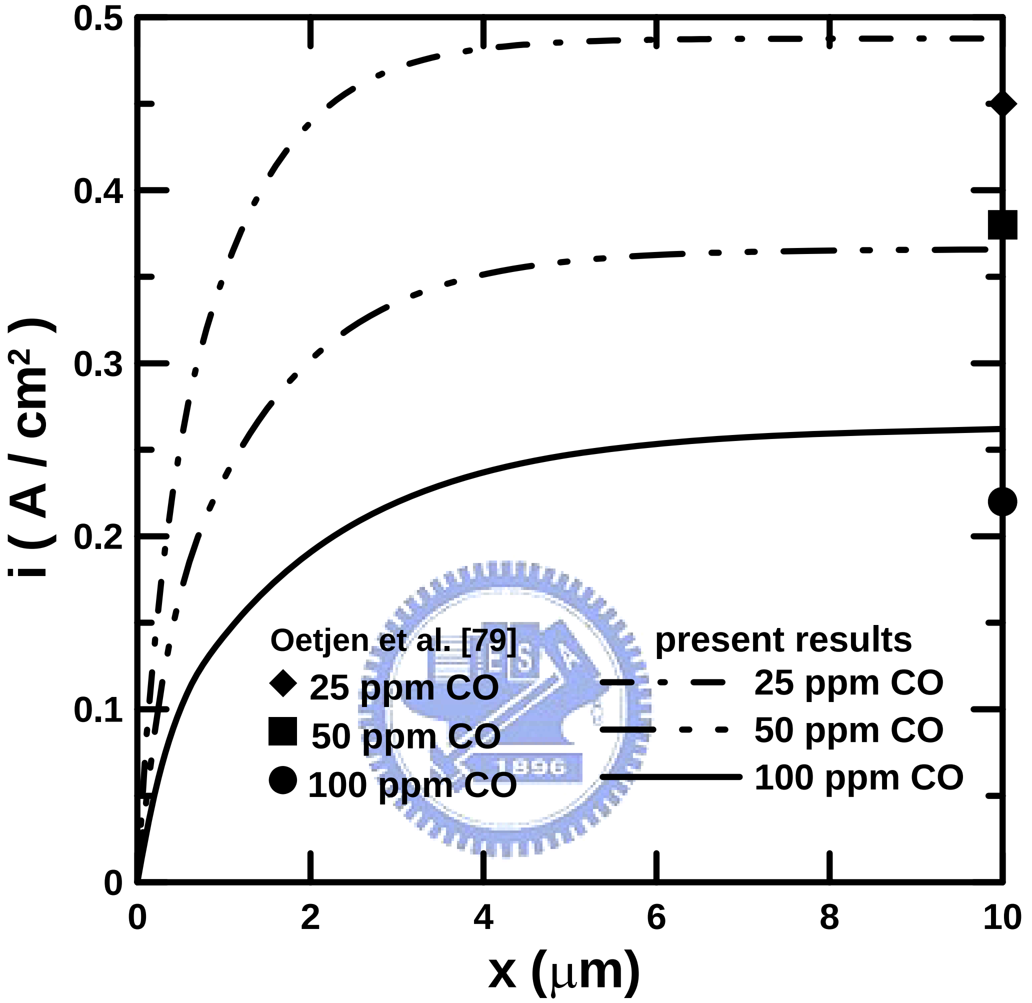

Fig. 2.9 Distributions of current density at steady state across anode catalyst layer for different CO concentration with ε_{CL}=0.4, η=0.01, and L_c=10μm.

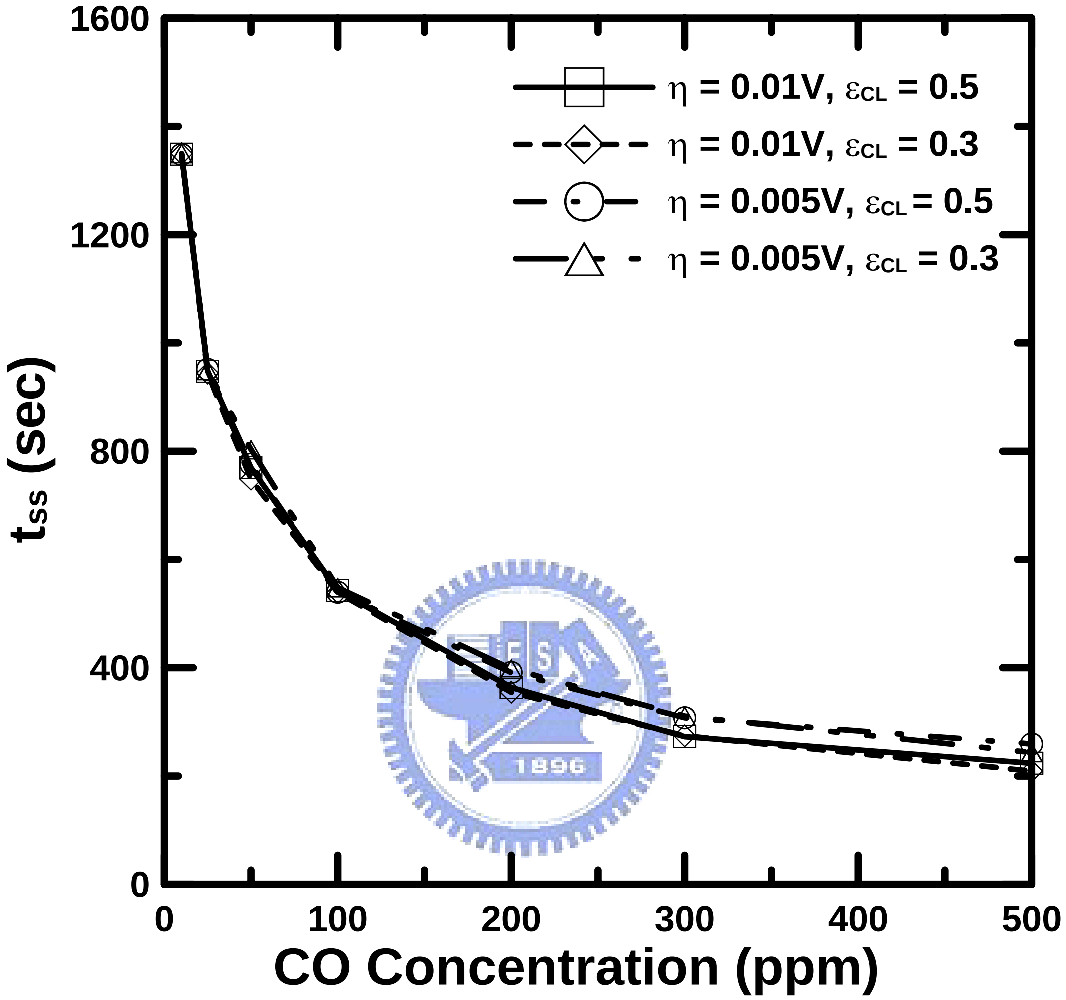

Fig. 2.10 Effects of the ppm CO concentration on the response time interval for different anode overpotential η and gas porosity ε_{CL} with L_c=10μm.

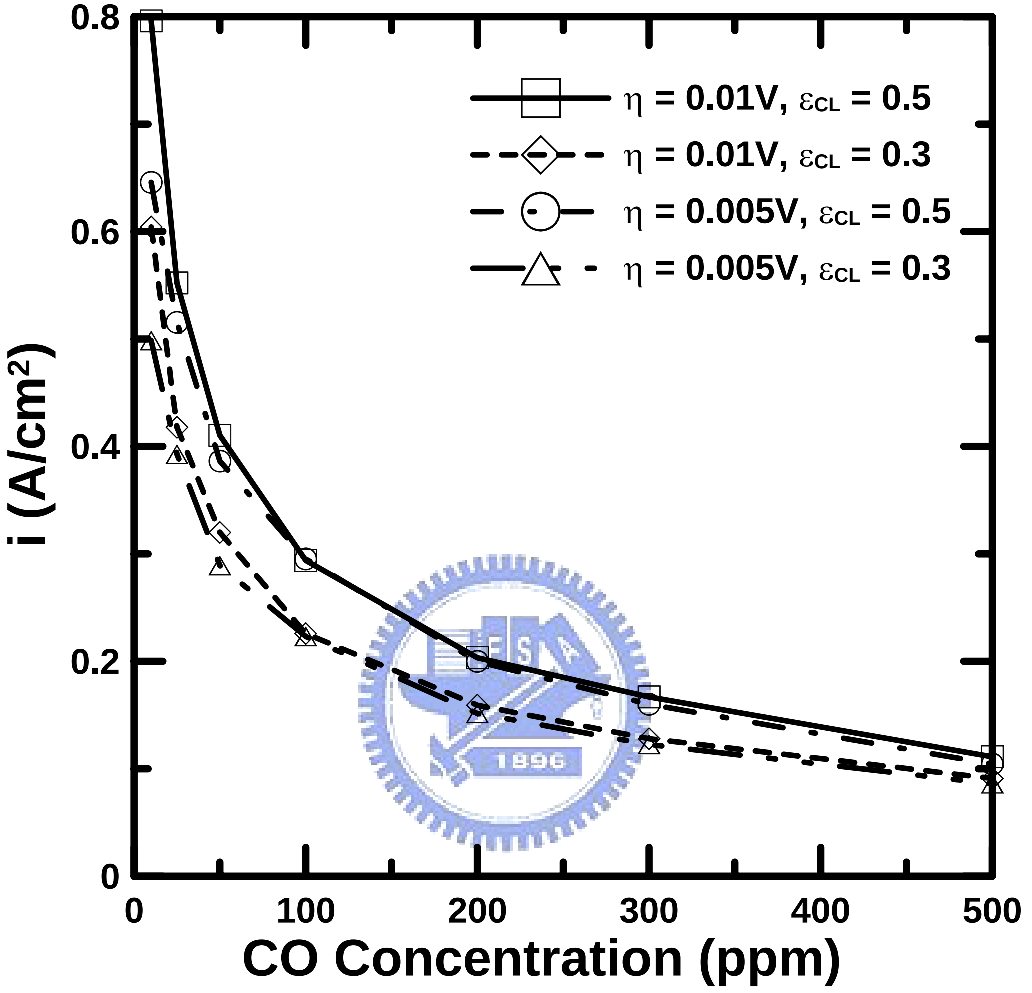

Fig. 2.11 Effects of the ppm CO concentration on the current density for different anode overpotential η and gas porosity ε_{CL} with L_c=10μm.

3. Two-Phase Modeling of a PEMFC with CO Poisoning Effect Using Dilute Hydrogen Feed

In this chapter, we extended our previous study to a one-dimensional, two-phase mathematical model to analyze the poisoning effect of anode CO kinetics on the performance of a PEM fuel cell using dilute hydrogen feed. Both vapor and liquid water transport are examined inside the cell. Figure 3.1 illustrates the presented simulation model of the PEM fuel cell, including the anode catalyst layer, the membrane and the cathode catalyst layer. Some basic assumptions were made as following:

1. Steady state.
2. One dimensional Cartesian coordinate system.
3. Isothermal and isobaric.
4. Ideal gas.
5. Catalyst layer and membrane are isotropic.
6. Only diffusion mechanism is considered.
7. Permeability is constant
8. Physical domain includes anode catalyst layer, membrane and cathode catalyst layer.

3.1 Theoretical Model

The two-phase theoretical CO poisoning behavior is investigated. Table 3.1 presents the governing equations which were used in the theoretical model where gaseous hydrogen concentration C_{H2}; the gaseous oxygen concentration C_{O2}; the gaseous carbon monoxide concentration C_{CO}; the vapor concentration C_{wg}; the concentration of liquid water in the Nafion phase C_{wn}; the saturation of liquid water s and the ionic potential ϕ. The variables must be solved for simultaneously. The steady state hydrogen coverage θ_H and carbon monoxide coverage θ_{CO} are expressed as

$$\begin{aligned} &k_{fH} \mathrm{X}_{H_2} P\left(1-\theta_{H_2}-\theta_{CO}\right) \\ &-b_{fH} k_{fH} \theta_{H_2} - 2k_{eH} \theta_{H_2} \sinh\left(\frac{n_{H_2} F\left(\phi_s - \phi - U_0\right)}{2RT}\right) = 0 \end{aligned} \tag{3-1}$$

$$\begin{aligned} &k_{fCO} \mathrm{X}_{CO} P\left(1-\theta_{H}-\theta_{CO}\right) \\ &-b_{fCO} k_{fCO} \theta_{CO} - 2k_{eCO} \theta_{CO} \sinh\left(\frac{n_{CO} F\left(\phi_s - \phi - U_0\right)}{2RT}\right) = 0 \end{aligned} \tag{3-2}$$

in which ϕ_s is the phase potential of solid phase of electrode. The transport of fuel, oxidant and vapor water are expressed as

$$N_i = -D_i \left[\varepsilon_{CL}(1-s)\right]^{1.5} \nabla C_i \tag{3-3}$$

where N is the flux for fuel, oxidant and vapor water and ε_{CL} is the gaseous porosity. The water transfer rate between the gas and liquid interfacial phase used by He et al. [21] and Lin et al. [27] and is used herein.

$$R_w = k_c \frac{\varepsilon_{CL}(1-s) y_v}{RT} \left(y_v P - P_v^{sat}\right) q + k_v \frac{\varepsilon_{CL} s \rho_w}{M_w} \left(y_v P - P_v^{sat}\right)(1-q) \tag{3-4}$$

The first and second term on the right hand side represents the condensation and evaporation rates, respectively. The transport of liquid water in the membrane is driven by the combined effect of diffusion and electro-osmotic drag [80]:

$$N_w = -D_{wn} \frac{\partial C_{wn}}{\partial x} + \frac{i}{F} n_d \tag{3-5}$$

in which N_w is the flux of liquid water. The transport of liquid water in the catalytic layer is described by the simplified correlation $K_w(s)$ equals a constant value [21]. Equation (3-6) describes the liquid water transport in the cathode catalyst layer.

$$\frac{\rho_w K_{w,0}}{M_w \mu_w} \left(-\frac{dP_c}{ds}\right) \nabla^2 s + \left(4 n_{d,CL} + 2\right) R_{O_2} + R_w = 0 \tag{3-6}$$

in which ρ_w is the density of liquid water, μ_w is the viscosity, K_w is the permeability, M_w is the molecular weight, $n_{d,CL}$ is the coefficient of electro-osmotic drag, R_{O2} is the reaction rate of oxygen and P_c is the capillary pressure. In the present theoretical study $\left(-dP_c/ds\right)$ is treated as a constant and R_w is calculated from Eq. (3-4).

Protons were produced from hydrogen oxidation reactions at the anode catalyst layer and then transported toward fuel cell cathode through membrane. The current density at the membrane can be expressed as [27]:

$$i = -k_n \nabla \phi \tag{3-7}$$

Where k_n is the membrane conductivity. In the anode catalyst layer, the distributions of the current densities of hydrogen and carbon monoxide are

$$\frac{di_{H_2}}{dx} = 2ak_{eH}\theta_{H_2}\sinh\left(\frac{n_{H_2}F(\phi_s-\phi-U_0)}{2RT}\right) \tag{3-8}$$

$$\frac{di_{CO}}{dx} = 2ak_{eCO}\theta_{CO}\sinh\left(\frac{n_{CO}F(\phi_s-\phi-U_0)}{2RT}\right) \tag{3-9}$$

where k_{eH} and k_{eCO} are the hydrogen and CO electro-oxidation rate constants [53]; ϕ represents the electrolytic phase potential and U_0 is the thermodynamic equilibrium potential [81]. The reaction rates of hydrogen, CO and oxygen within in the catalytic layers are

$$R_{H_2} = (1-s)\frac{di_{H_2}}{dz}\left(\frac{\gamma_{H_2}}{n_{H_2}F}\right) \tag{3-10}$$

$$R_{CO} = (1-s)\frac{di_{CO}}{dz}\left(\frac{\gamma_{CO}}{n_{CO}F}\right) \tag{3-11}$$

$$R_{O_2} = \frac{1}{4F}\left(1-\bar{\theta}_{CO}\right)(1-s)ai_0\left[\frac{C_{O_2}}{C_{O_2 ref}}\exp\left(\frac{-F(\phi_s-\phi-U_0)}{RT}\right)\right] \tag{3-12}$$

where $\bar{\theta}_{CO}$ is the average value of CO coverage which was calculated from the anode CO coverage θ_{CO}. Table 3.2 lists all of the boundary conditions used in this simulation model.

3.2 Numerical Method

In this chapter, the governing equations in table 3.1 are second order ordinary differential equations. Central difference scheme is applied to solve the dependent variables. The transport equations for hydrogen and carbon monoxide can be rewritten as:

$$D_{H_2}\varepsilon_{CL}^{1.5}\left[(1-s_i)^{1.5}\frac{C_{H_2,i+1}-2C_{H_2,i}+C_{H_2,i-1}}{\Delta x^2}-1.5(1-s_i)^{0.5}\frac{s_{i+1}-s_{i-1}}{2\Delta x}\frac{C_{H_2,i+1}-C_{H_2,i-1}}{2\Delta x}\right]-R_{H_2,i}=0 \tag{3-13}$$

$$D_{CO}\varepsilon_{CL}^{1.5}\left[(1-s_i)^{1.5}\frac{C_{CO,i+1}-2C_{CO,i}+C_{CO,i-1}}{\Delta x^2}-1.5(1-s_i)^{0.5}\frac{s_{i+1}-s_{i-1}}{2\Delta x}\frac{C_{CO,i+1}-C_{CO,i-1}}{2\Delta x}\right]-R_{CO,i}=0 \tag{3-14}$$

The dependent variables must be solved simultaneously. Other variables such as oxygen, proton, vapor and liquid water can be treated by using the same finite difference method.

3.3 Results and Discussion

A one-dimensional, two-phase mathematical model under various CO concentrations and hydrogen dilutions are employed to simulate hydrogen fuels from the reformer, and thus elucidate the poisoning effect on the performance of the fuel cell. The reactant gas distribution, the coverage and the liquid water distribution are investigated under the CO poisoning. The feed streams were fully saturated with water at 80° C at both the anode and the cathode inlets. Table 3.3 presents the parameters used in this work.

Figure 3.2 plots the hydrogen coverage across the anode catalyst layer with various CO concentrations and hydrogen dilutions. The hydrogen coverage, θ_{H2}, decreases with CO concentration increases because increasing the CO concentration increases the rate of adsorption of CO onto the sites of the catalyst. When the anode inlet flow contains hydrogen dilution, θ_H also falls with increasing the dilute of hydrogen. Further, reduces the number of catalytic sites available for the electro-oxidation of hydrogen. From the figure hydrogen dilution significantly affects the hydrogen coverage, especially at low ppm CO. During poisoning, adding pure hydrogen fuel increase more reaction sites for hydrogen, especially at low CO concentration. Figure 3.3 shows opposite trend of CO coverage on the catalytic sites, because the Pt catalyst has a strong affinity for CO. The accumulation of CO at the catalytic sites is sustained, inhibiting the electro-oxidation of hydrogen.

Figure 3.4 shows the liquid water saturation profiles across the anode catalyst layer. The effect of the electro-osmotic drag is proportional to the cell current density, which was generated by the electro-chemical reaction of fuel gas. The coverage of hydrogen falls, so the current density was reduced, weakening the effect of electro-osmotic drag. However, the oxygen reduction reactions are also suppressed, reducing the diffusion of water from the cathode to the anode. Therefore, the saturation level of liquid water across the anode catalyst layer decreases with amount of CO and hydrogen dilution increase. The distribution of liquid water saturation level depends more strongly on the CO concentration than on dilution of hydrogen.

Figure 3.5 plots the liquid water distribution across the membrane. The gradient of the liquid water distribution declines with CO contents, because, as the amount of CO increases, the rate of the reaction decreases on both the anode and the cathode sides. The effect of electro-osmotic drag and the diffusion of liquid water from the cathode to the anode are also weakened, reducing the slope of the liquid water distribution across the membrane. At 100 ppm CO, 40%H_2, the effect of the electro-osmotic drag is small and less liquid water is generated at the cathode catalyst layer, causing the liquid water distribution to have a smallest slop. Consequently, the CO concentration significantly influences the distribution of liquid water across the membrane.

Figure 3.6 reveals that the amount of liquid water saturation level of the cathode catalyst layer greatly exceeds that on the anodic side of the catalyst. The small electro-osmotic drag and the generation of less liquid water cause the drops of liquid saturation level. Figure 3.7 presents the ionic potential profile across the MEA. In the catalytic layers, the ionic potential distribution is nonlinear, because chemical reactions consume fuel gas. Under poisoning, the ionic potential loss decreases, because CO poisoning reduces the output current density. As discussed above, increasing the CO level or diluting the hydrogen seriously reduces the saturation level of liquid water and the loss of ionic potential.

Figure 3.8 compares the present simulation results with experimental data reported by Bhatia and Wang [58] or four gas compositions fed into the anode. The simulation results show that the cell performance and durability depends strongly on the dilution of hydrogen and CO concentration. Increasing hydrogen dilution and CO concentration degrades the performance of the cell. The predicted CO poisoning results agree closely with the experimental values. Increasing the amount of pure hydrogen drastically increases cell current density for a wide range of CO contents, promoting the tolerance for CO. Figure 3.9 plots the effect of various hydrogen dilutions and CO contents on the performance of the fuel cell. As shown in the polarization curve, the theoretical results indicate that a higher CO concentration and hydrogen dilution results in large drop in the cell performance. The presence of CO in the anodic inlet flow inhibits the reactions on both anode and cathode side. The performance of the fuel cell depends more strongly on the CO concentration than on dilution of hydrogen. Increasing hydrogen dilution and CO concentration further degrades the performance of the fuel cell. In order to promote the tolerance for CO, increasing the amount of pure hydrogen drastically increases current density for a wide range of CO contents.

Table 3.1. Governing equations

Variables	ACL	MEM	CCL
C_{H_2}	$-\nabla \cdot N_{H_2} - R_{H_2} = 0$	N/A	N/A
C_{O_2}	N/A	N/A	$-\nabla \cdot N_{O_2} - R_{O_2} = 0$
C_{CO}	$-\nabla \cdot N_{CO} - R_{CO} = 0$	N/A	N/A
C_{wg}	$-\nabla \cdot N_{wg} - R_w = 0$	N/A	$-\nabla \cdot N_{wg} - R_w = 0$
C_{wn}	$\nabla C_{wn} = 0$	$D_{wn}\nabla^2 C_{wn} = 0$	$\nabla C_{wn} = 0$
s	$\frac{\rho_w K_{w,0}}{M_w \mu_w}\left(-\frac{dP_c}{ds}\right)\nabla^2 s + R_w = 0$	N/A	$\frac{\rho_w K_{w,0}}{M_w \mu_w}\left(-\frac{dP_c}{ds}\right)\nabla^2 s$ $+\left(4n_{d,CL}+2\right)R_{O_2} + R_w = 0$
ϕ	$k_{n,eff}\nabla^2\phi - \left(R_{H_2} + R_{CO}\right) = 0$	$k_n \nabla^2 \phi = 0$	$k_{n,eff}\nabla^2\phi - R_{O_2} = 0$

Table 3.2. Boundary Conditions

Variables	$x = 0$	$ACL\,/\,MEM$	$MEM\,/\,CCL$	$x = L$
C_{H_2}	$C_{H_2} = C_{H_2}^{in}$	$N_{H_2} = 0$	N/A	N/A
C_{O_2}	N/A	N/A	$N_{O_2} = 0$	$C_{O_2} = C_{O_2}^{in}$
C_{CO}	$C_{CO} = C_{CO}^{in}$	$N_{CO} = 0$	N/A	N/A
C_{wg}	$C_{wg} = C_{wg}^{in}$	$N_{wg} = 0$	$N_{wg} = 0$	$C_{wg} = C_{wg}^{in}$
C_{wn}	N/A	$\sigma(C_a - C_{wn}) = N_w$	$\frac{i}{2F} + \sigma(C_c - C_{wn}) = -N_w$	N/A
s	$s = 0$	$N_s = N_w$	$N_w = N_s$	$s = 0$
ϕ	$\phi = 0$	$k_{n,eff}\nabla\phi = k_n\nabla\phi$	$k_{n,eff}\nabla\phi = k_n\nabla\phi$	$\nabla\phi = 0$

Table 3.3 The parameters used in the present model [57,58,81].

Temperature	T	353 K
Pressure	P	1 atm
Diffusion coefficient of hydrogen in gas phase	D_{H_2}	1.1028 $(\mathrm{cm}^2\ \mathrm{s}^{-1})$
Diffusion coefficient of oxygen in gas phase	D_{O_2}	$0.1775\times(\mathrm{T}/273.15)^{1.823}$ $(\mathrm{cm}^2\ \mathrm{s}^{-1})$
Diffusion coefficient of vapor in gas phase	D_{wg}	$0.256\times(\mathrm{T}/307.15)^{2.334}$ $(\mathrm{cm}^2\ \mathrm{s}^{-1})$
Thickness of catalyst layer	δ_{CL}	16 (μm)
Thickness of membrane	δ_{MEM}	50 (μm)
Gas porosity in catalyst layer	ε_{CL}	0.4
Volumetric fraction of Nafion in membrane	ε_{MEM}	0.4
Membrane conductivity	k_n	0.17 $(\mathrm{mho}\ \mathrm{cm}^{-1})$

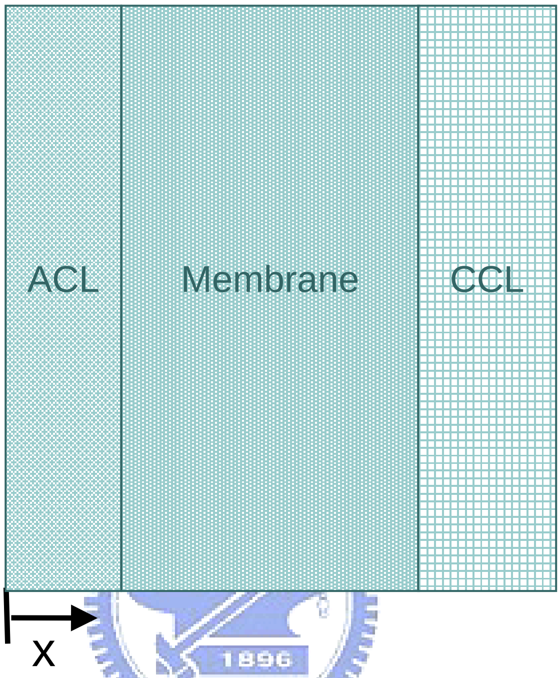

Fig. 3.1 A schematic model of MEA of the PEM fuel cell.

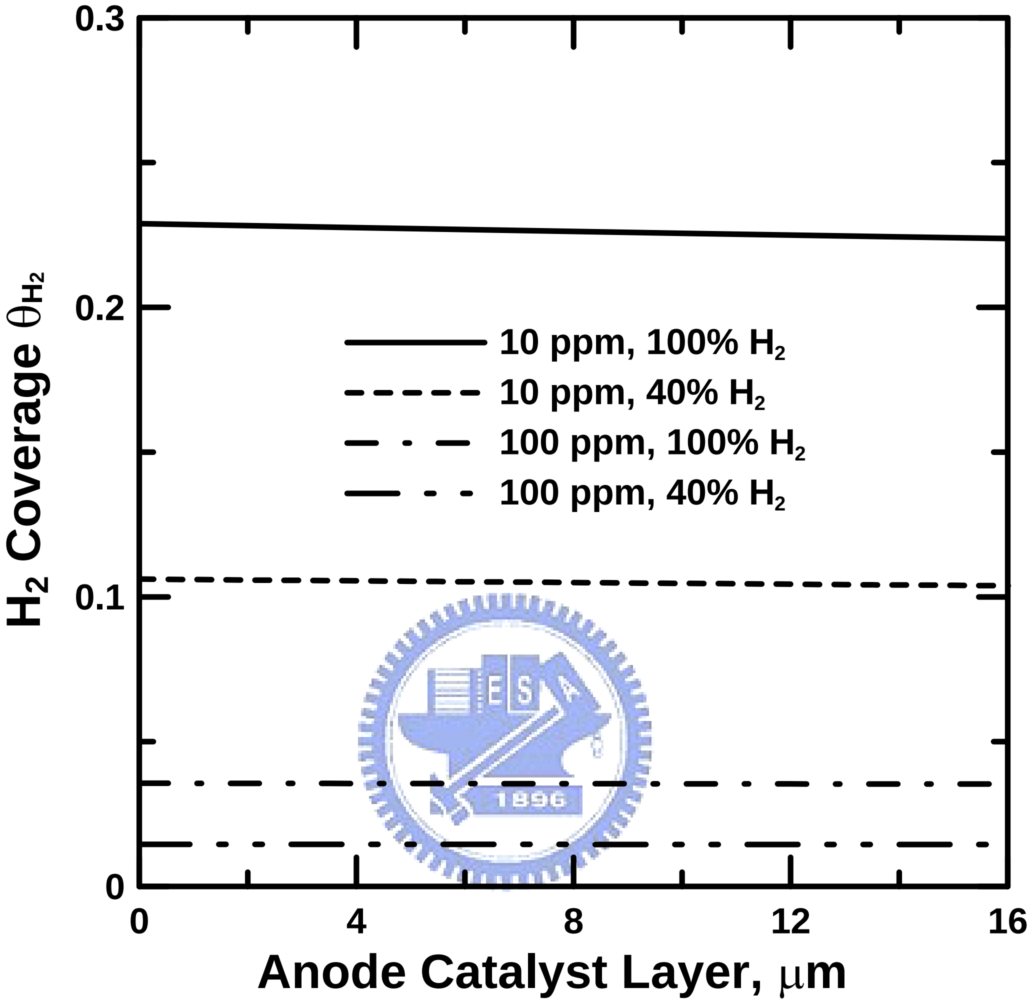

Fig. 3.2 The effect of various CO concentrations and hydrogen dilutions on the distribution of hydrogen coverage across the anode catalyst layer at 0.6 V.

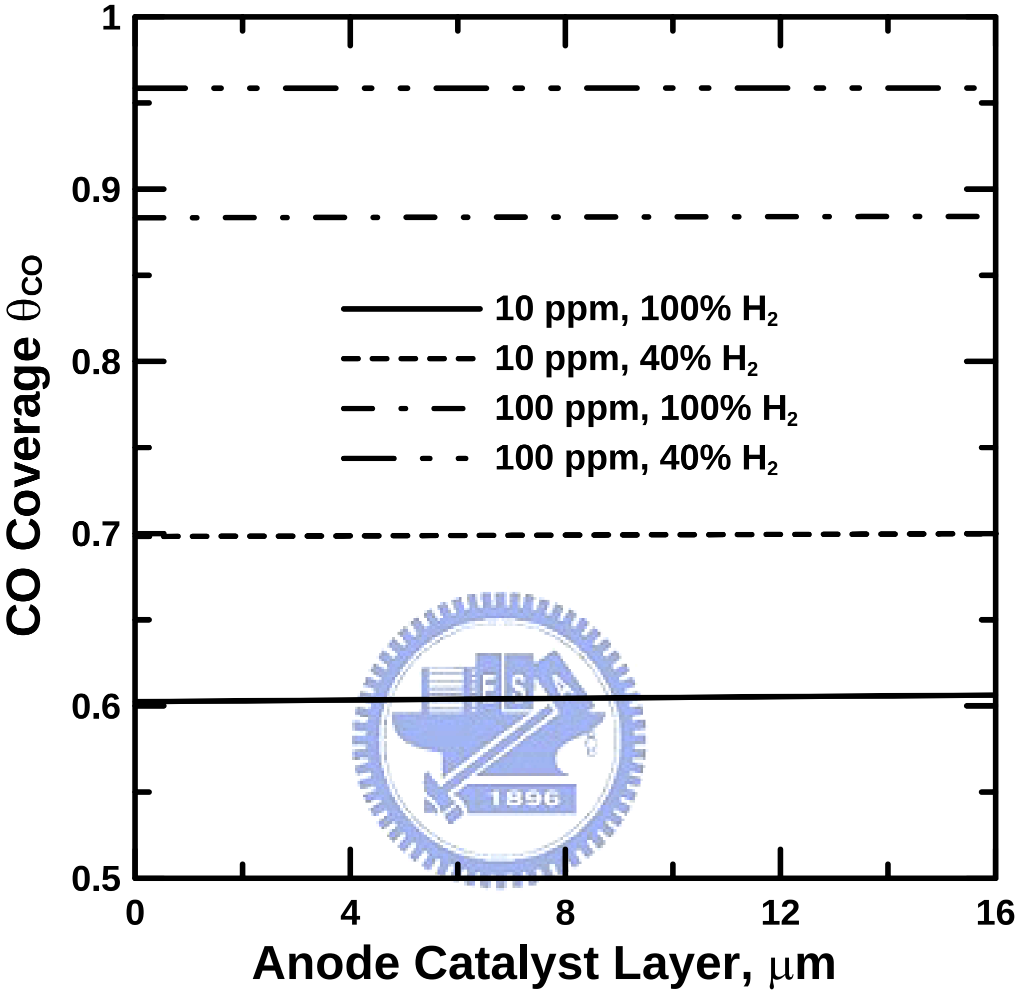

Fig. 3.3 The effect of various CO concentrations and hydrogen dilutions on the distribution of CO coverage across the anode catalyst layer at 0.6 V.

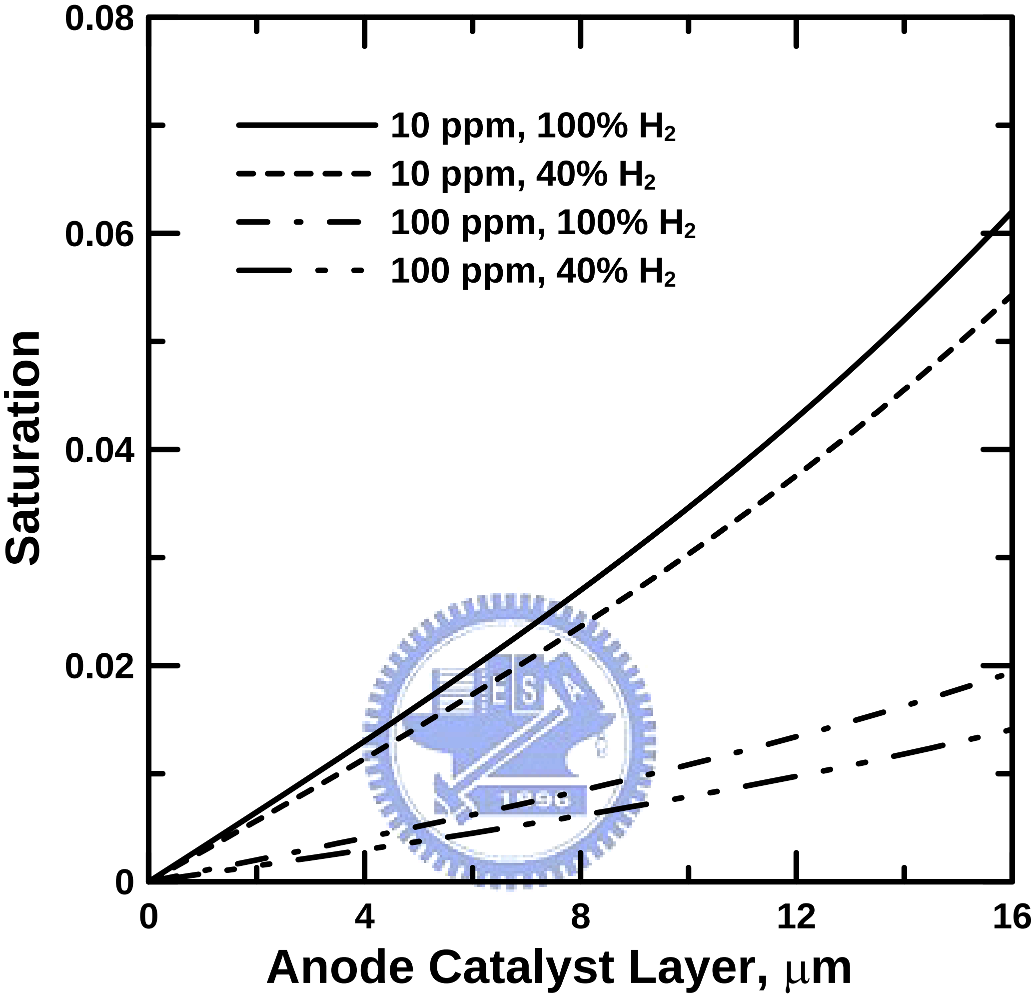

Fig. 3.4 The effect of various CO concentrations and hydrogen dilutions on the distribution of liquid water saturation across the anode catalyst layer at 0.6 V.

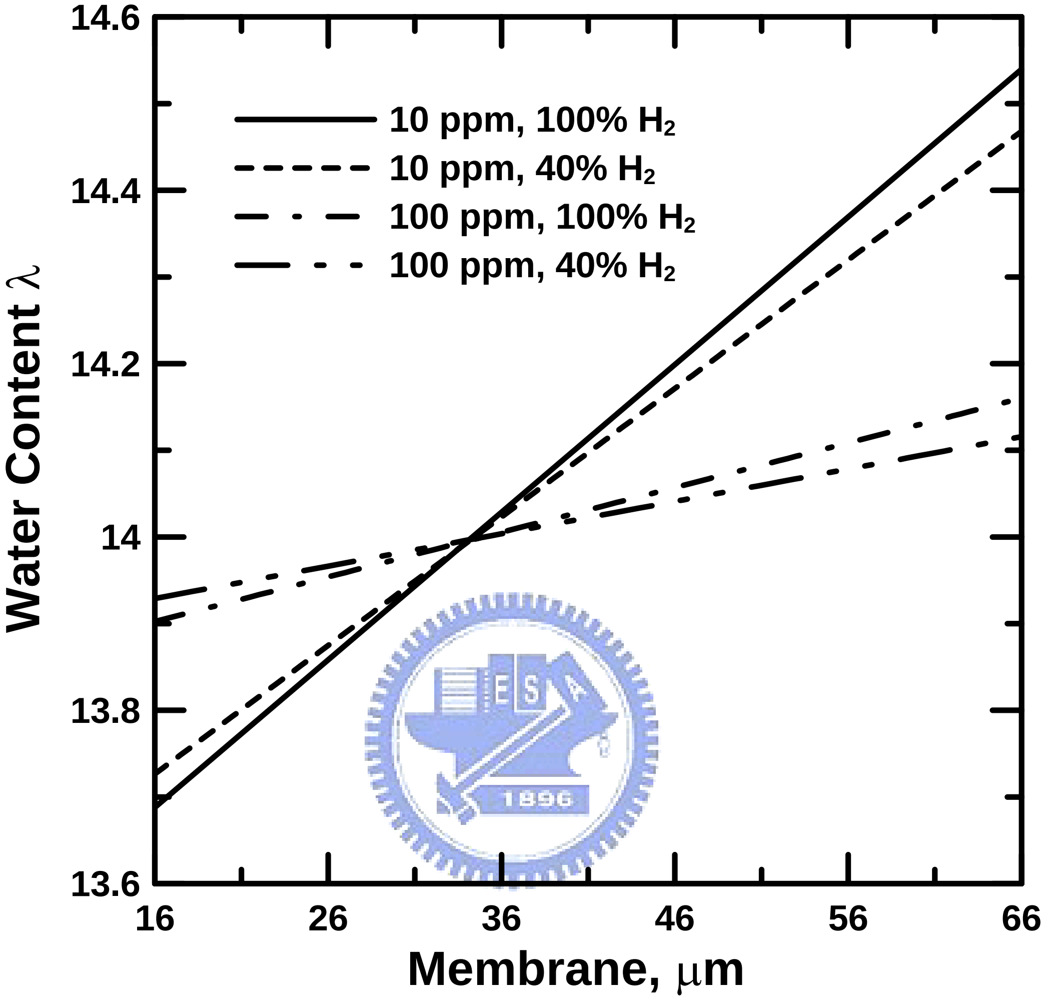

Fig. 3.5 The effect of various CO concentrations and hydrogen dilutions on the distribution of water content across the membrane at 0.6 V.

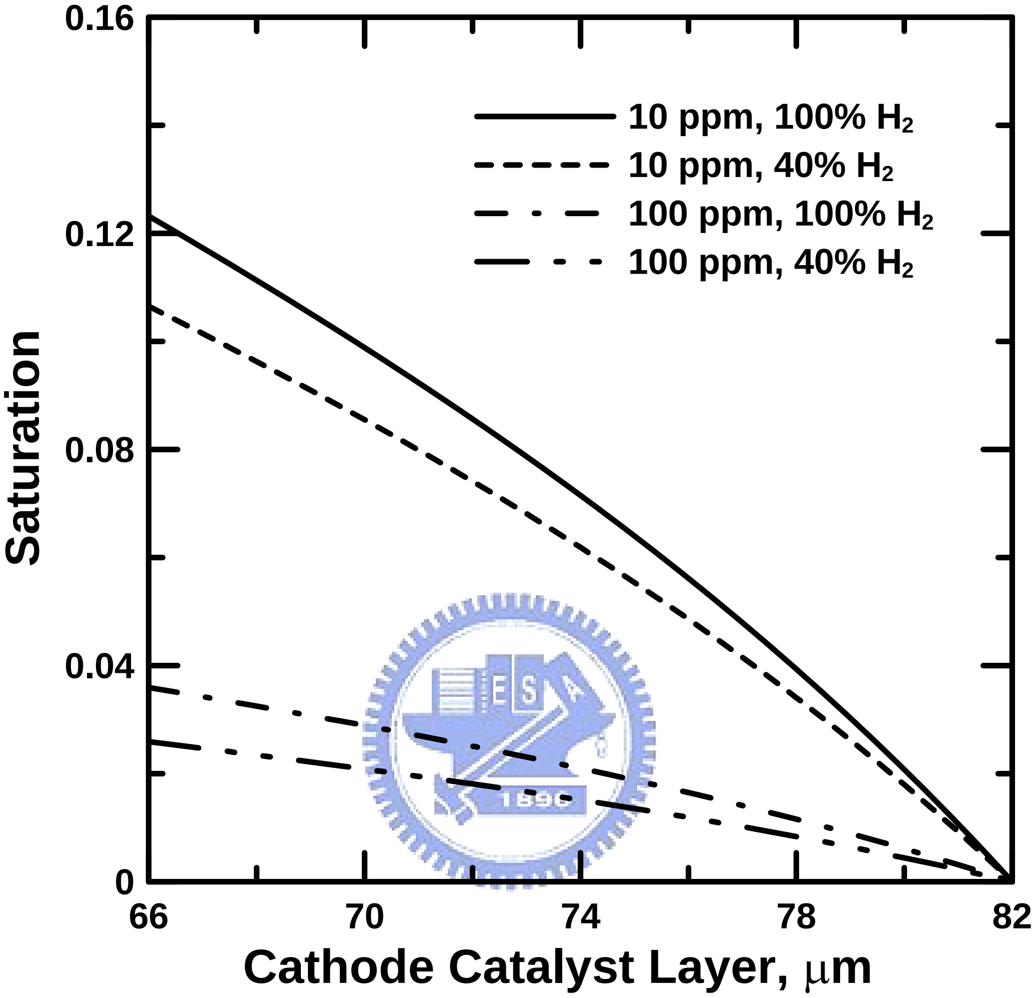

Fig. 3.6 The effect of various CO concentrations and hydrogen dilutions on the distribution of liquid water saturation across the cathode catalyst layer at 0.6 V.

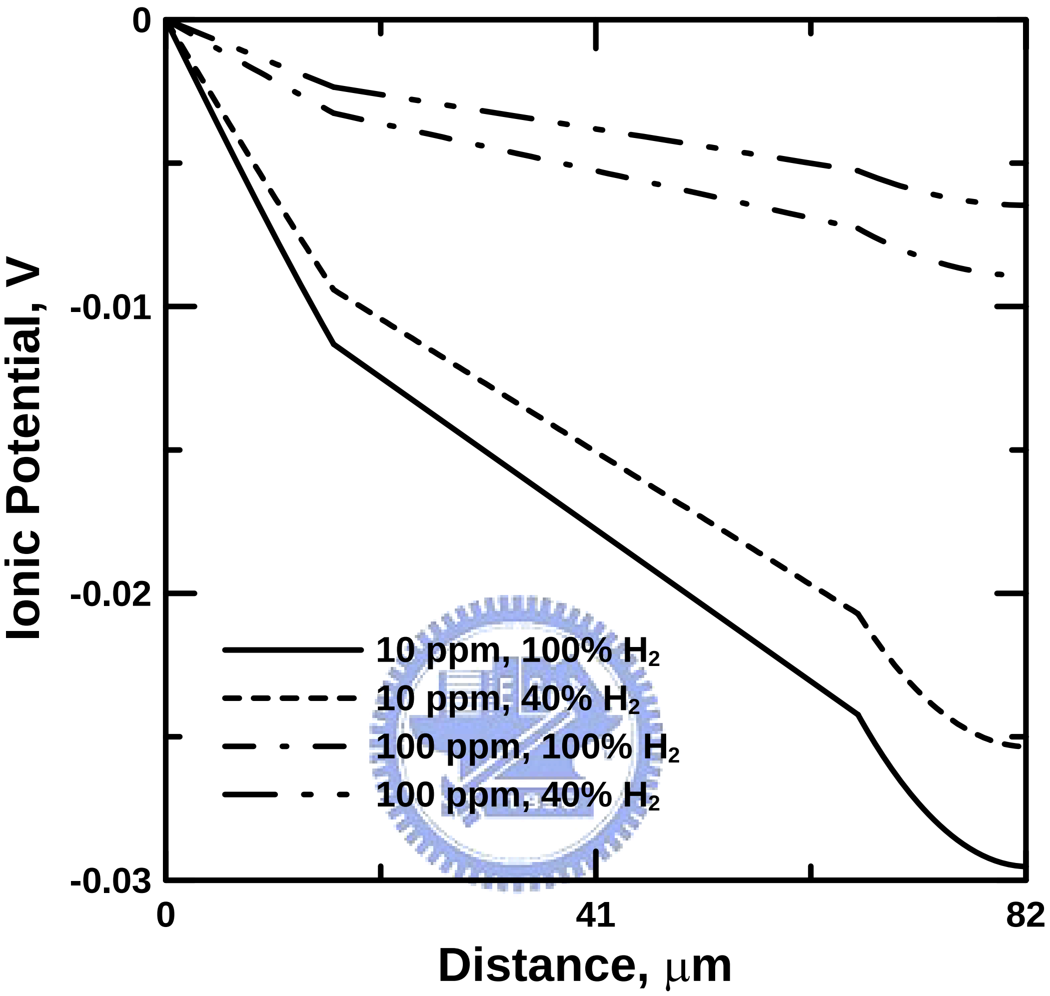

Fig. 3.7 The effect of various CO concentrations and hydrogen dilutions on the distribution of ionic potential across the MEA at 0.6 V.

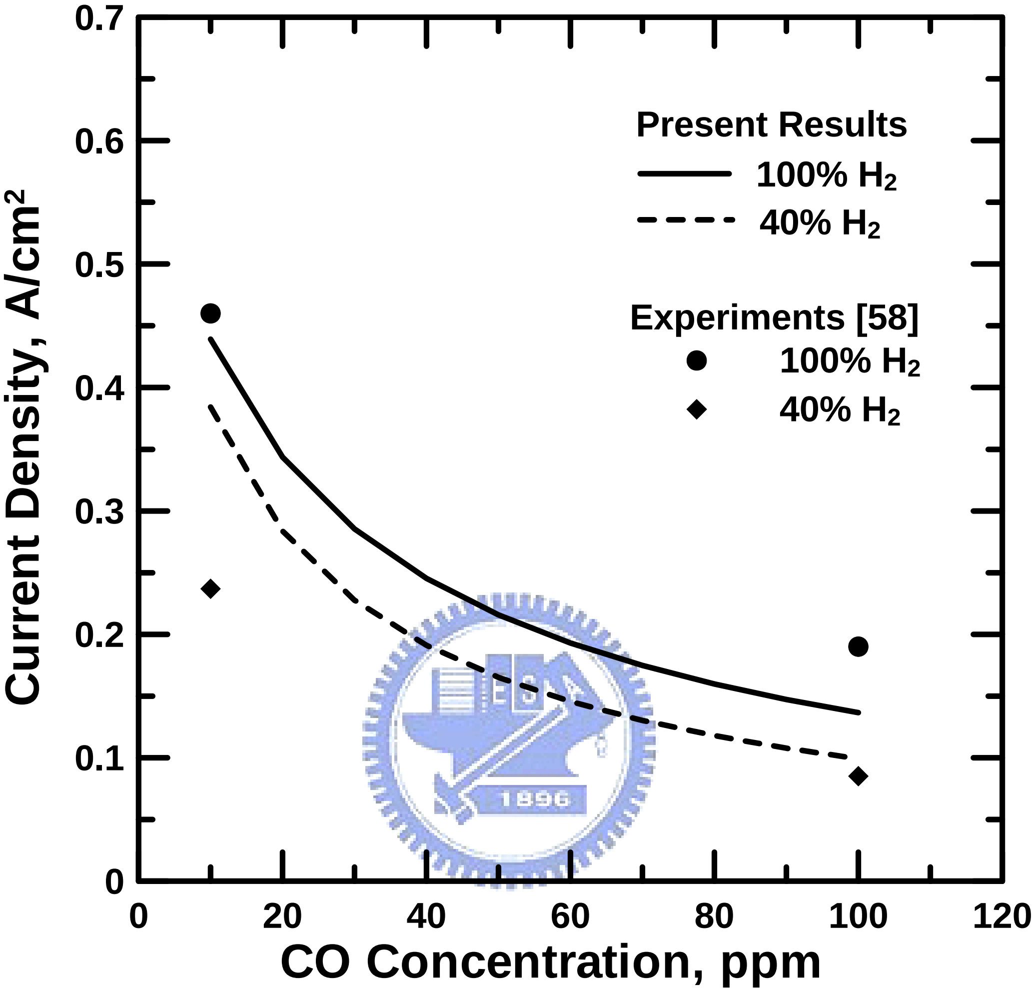

Fig. 3.8 The present simulation results compare with experimental data at 0.6 V.

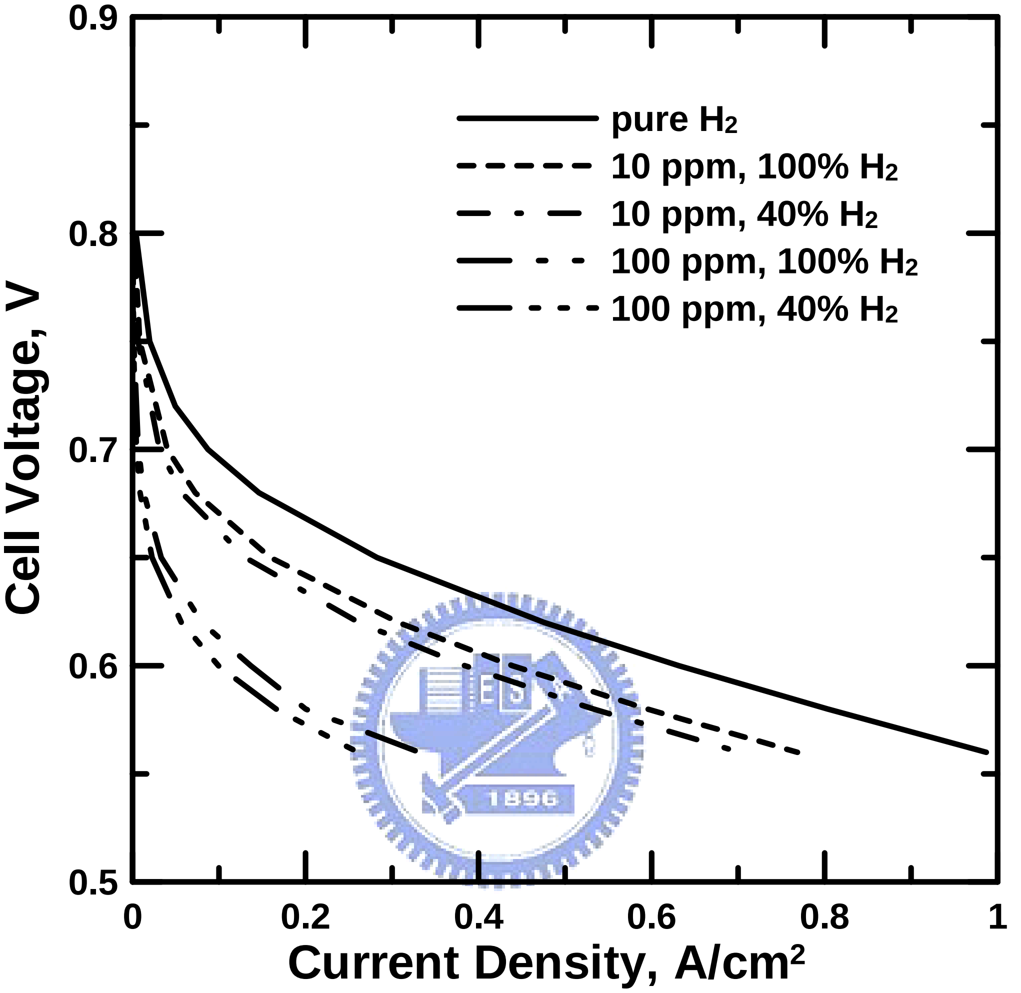

Fig. 3.9 The effect of various hydrogen dilutions and CO contents on the performance of the fuel cell.

4. Transient Analysis of Multicomponent Transport with Carbon Monoxide Poisoning Effect of a PEM Fuel Cell

A one-dimensional, two-phase, transient mathematical model was developed to analyze how carbon monoxide poisoning affects the performance of a PEM fuel cell. This work examines both vapor and liquid water transport inside the cell. Although the fuel cell performance exhibited transient variations at different CO concentrations, the actual transient coverage profile and the reactant gas distribution over the catalyst layer are not presented. In this work, a transient two-phase mathematical model of the poisoning effect of PEM fuel cells by CO is investigated. Various parameters are considered to promote the tolerance for CO and analyze the effect on the characteristic time t_{ss}, and thus elucidate transport phenomena inside the cell and improve its performance. Some basic assumptions were made as following:

1. Unsteady state.
2. One dimensional Cartesian coordinate system.
3. Isothermal and isobaric.
4. Ideal gas.
5. Catalyst layer and membrane are isotropic.
6. Only diffusion mechanism is considered.
7. Permeability is function of liquid water saturation.
8. Physical domain includes anode catalyst layer, membrane and cathode catalyst layer.

4.1 Theoretical Model

Physical model was shown in Fig. 4.1, including the anode catalyst layer, the membrane and the cathode catalyst layer. Base on our previous studies in chapter 3, a transient, two-phase theoretical model was developed to analyze CO poisoning process. Table 4.1 presents the governing equations used in this study. The governing equations must be solved simultaneous for the dependent variables. Fuel, oxidant and vapor water transport are expressed as

$$\frac{\partial}{\partial t}\left[(1-s)\varepsilon_{CL}C_i\right] = -\nabla\cdot\left\{-D_i\left[\varepsilon_{CL}(1-s)\right]^{1.5}\nabla C_i\right\} - R_i \tag{4-1}$$

The first term on the left hand side represents time evolution of the species concentrations. When s equals zero, equation (4-1) can be reduced to single phase model. The second term on the right hand side is the source term for hydrogen, carbon monoxide, vapor water and oxygen, respectively. The water transfer rate between the gas and liquid interfacial phase used by Lin et al. [27] and He et al. [21] is used herein.

$$R_W = k_c\frac{\varepsilon_{CL}(1-s)y_v}{RT}\left(y_v P - P_v^{sat}\right)q + k_v\frac{\varepsilon_{CL}s\rho_W}{M_W}\left(y_v P - P_v^{sat}\right)(1-q) \tag{4-2}$$

where y_v represents mole fraction of vapor water, k_c and k_v represent condensation and evaporation rate constant, P_v^{sat} is the water vapor saturation pressure. In equation (4-2), q is the switch function which was expressed as [21]:

$$q = \frac{1+\left|\left(y_v^p - p_v^{sat}\right)\right|/\left(y_v^p - p_v^{sat}\right)}{2} \tag{4-3}$$

The transport equation of liquid water in the membrane is driven by the combined effect of diffusion and electro-osmotic drag [80]:

$$N_w = -D_{wn}\frac{\partial C_{wn}}{\partial x} + \frac{i}{F}n_d \tag{4-4}$$

in which N_w is the flux of liquid water; D_{wn} is the diffusion coefficient of liquid water; i is the flux of the charges; n_d is the electro-osmotic drag coefficient, and F is the Faraday constant. The transport of liquid water in the catalytic layer is described by the simplified correlation $K_w(s) = K_{w,0}s$, which elucidates the relationship between the permeability to liquid water and the saturation of liquid water [27]. At the anode side, the transport equation of liquid water is expressed as

$$\frac{\varepsilon_{CL}\rho_w}{M_w}\frac{\partial s}{\partial t} = \frac{\rho_w K_{w,0}}{M_w \mu_w}\left(-\frac{dP_c}{ds}\right)\left(s\nabla^2 s + (\nabla \cdot s)^2\right) + R_w \tag{4-5}$$

in which ρ_w is the density of liquid water, μ_w is the viscosity, K_w is the permeability, M_w is the molecular weight and P_c is the capillary pressure. In the present mathematical model $\left(-dP_c/ds\right)$ is treated as a constant and R_w is calculated from Eq. (4-2).The time-dependent coverage of θ_{H_2} and θ_{CO} are extended from equations (3-1) and (3-2).

$$\begin{aligned}\xi\frac{d\theta_{H_2}}{dt} &= k_{fH} \mathrm{X}_{H_2} P\left(1-\theta_{H_2}-\theta_{CO}\right) \\ &-b_{fH}k_{fH}\theta_{H_2} - 2k_{eH}\theta_{H_2}\sinh\left(\frac{n_{H_2}F(\phi_s-\phi-U_0)}{2RT}\right)\end{aligned} \tag{4-6}$$

$$\begin{aligned}\xi\frac{d\theta_{CO}}{dt} &= k_{fCO} \mathrm{X}_{CO} P\left(1-\theta_{H_2}-\theta_{CO}\right) \\ &-b_{fCO}k_{fCO}\theta_{CO} - 2k_{eCO}\theta_{CO}\sinh\left(\frac{n_{CO}F(\phi_s-\phi-U_0)}{2RT}\right)\end{aligned} \tag{4-7}$$

where ξ is the molar area density of the catalyst sites; X_{H2} is the molar fraction of hydrogen; X_{CO} is the CO molar fraction, and P is the total pressure. The reaction rates of hydrogen and CO within the anode catalyst layer are

$$R_{H_2} = (1-s)\frac{di_{H_2}}{\mathrm{dx}}\left(\frac{\gamma_{H_2}}{n_{H_2}F}\right) \tag{4-8}$$

$$R_{CO} = (1-s)\frac{di_{CO}}{dx}\left(\frac{\gamma_{CO}}{n_{CO}F}\right) \tag{4-9}$$

where γ is the stoichiometric coefficient, n is the number of electrons. At the cathode catalyst layer, the reaction rate of oxygen is given by

$$R_{O_2} = \frac{1}{4F}\left(1-\bar{\theta}_{CO}\right)\left(1-s\right)ai_0\left[\frac{C_{O_2}}{C_{O_2\,ref}}\exp\left(\frac{-F\left(\phi_s-\phi-U_0\right)}{RT}\right)\right] \tag{4-10}$$

where $\bar{\theta}_{CO}$ is the mean CO coverage, which was calculated from the anodic CO coverage θ_{CO}. The factor *(1-s)* represents the effect of liquid water saturation in the catalyst layers. The initial conditions are all steady-state without zero CO. Table 4.2 lists all of the boundary conditions used in this simulation model. Without consideration for the gas diffusion layer, the liquid water saturation is assumed to be zero at the boundaries (*x=0* and *x=L*). The governing equations in table 4.1 were solved by using implicit scheme. The 4th order Runge Kutta method was applied to solved hydrogen and carbon monoxide coverage.

4.2 Numerical Method

The governing equations are the parabolic partial differential equations which list in table 4.1. In this study, governing equations were solved by using implicit method. The above equation for hydrogen can be rewritten as:

$$-\varepsilon_{CL}C_{H_2,i}^{n+1}\frac{s_i^{n+1}-s_i^n}{\Delta t}+\left(1-s_i^{n+1}\right)\varepsilon_{CL}\frac{C_{H_2,i}^{n+1}-C_{H_2,i}^{n}}{\Delta t}=D_{H_2}\varepsilon_{CL}^{1.5}$$
$$\left[\left(1-s\right)^{1.5}\frac{C_{H_2,i+1}^{n+1}-2C_{H_2,i}^{n+1}+C_{H_2,i-1}^{n+1}}{\Delta x^2}-1.5\left(1-s_i^{n+1}\right)^{0.5}\frac{s_{i+1}^{n+1}-s_{i-1}^{n+1}}{2\Delta x}\frac{C_{H_2,i+1}^{n+1}-C_{H_2,i-1}^{n+1}}{2\Delta x}\right]-R_{H_2,i} \tag{4-11}$$

The transport equations of oxygen, carbon monoxide, vapor and liquid water are solved by using the same numerical scheme. The transport equation of liquid water saturation *s* shows a nonlinear form of parabolic type partial differential equation. For the nonlinear term, s can be solved by iterations until the relative error of liquid water saturation reaches 10^{-4}. The steady-state condition is defined as pertaining when the relative error of the output current density reaches 10^{-3} (A/cm^2).

$$\frac{i^{n+1}-i^{n}}{i^{n}} \le 10^{-3} \tag{4-12}$$

in which $i(n)$ is the current density at the nth min.

4.3 Results and Discussion

Various CO concentrations and hydrogen dilutions are employed to simulate a wide range of hydrogen fuels from the reformer, and thus elucidate the transient behavior associated with poisoning. The feed vapor water is fully saturated at 80^{o} C at both the anode and the cathode inlets. The reactant gas distribution, the coverage, the liquid water distribution and the time to reach steady state are investigated. The initial condition is started in the absence of CO. Table 4.3 presents the parameters used in this work.

Figure 4.2 plots the transient evolution of the hydrogen coverage across the anode catalyst layer with 10 ppm CO, 100%H_2 and 0.6 V. The simulation begins in the steady state without CO poisoning. Consequently, the hydrogen coverage, θ_H, decreases with time because CO is adsorbed on the Pt catalyst, reducing the number of catalytic sites available for the electro-oxidation of hydrogen. Figure 4.3 shows that during poisoning CO is adsorbed on the catalytic sites, because the Pt catalyst has a strong affinity for CO. The accumulation of CO at the catalytic sites is sustained, inhibiting the electro-oxidation of hydrogen. Hence, the hydrogen and CO coverage takes 100 min to reach a steady state.

Figure 4.4 shows the liquid water saturation profiles across the anode catalyst layer at different times, with 100 % H2, 10 ppm CO and 0.6 V. The effect of the electro-osmotic drag is proportional to the current density, which was generated by the electro-chemical reaction of hydrogen and oxygen. The coverage of hydrogen falls with time, so the current density was reduced, weakening the effect of electro-osmotic drag. However, the oxygen reduction reactions are also suppressed, reducing the diffusion of water from the cathode to the anode. Therefore, the saturation by liquid water across the anode catalyst layer decreases with time. During poisoning, the diffusion of liquid water from cathode to anode dominates the amount of liquid water at saturation in the anode catalyst layer.

Figure 4.5 plots the unsteady variations of the liquid water distribution across the membrane at various times. The gradient of the liquid water distribution declines with time, because, as the duration of poisoning increases, the rate of the reaction decreases with time on both the anode and the cathode sides. The effect of electro-osmotic drag and the diffusion of liquid water from the cathode to the anode are also weakened, reducing the slope of the liquid water distribution across the membrane. Figure 4.6 reveals that the amount of liquid water at saturation of the cathode catalyst layer greatly exceeds that on the anodic side of the catalyst. The small electro-osmotic drag and the generation of less liquid water cause the saturation level to drop with time.

Figure 4.7 presents the ionic potential profile across the MEA at various times. No gas fuel is consumed in the membrane phase, so the ionic potential distribution plotted in Fig. 4.7 is a straight line. In the catalytic layers, and especially in the cathode catalyst layer, the ionic potential distribution is nonlinear, because reduction reactions consume oxygen. During poisoning, the ionic potential falls with time reducing the output current density.

Figure 4.8 depicts the steady state hydrogen coverage profile across the anode catalyst layer at various CO concentrations and hydrogen dilutions at 0.6 V. The results indicate that at 10 ppm CO, t_{ss} is longer than at 100 ppm CO, for both 40% H_2 and 100% H_2. The hydrogen coverage is also higher at lower CO concentration, because increasing the CO concentration increases the rate of adsorption of CO onto the sites of the catalyst. Figure 4.9 plots the opposite trend. Hence, hydrogen dilution significantly affects the hydrogen coverage, especially at low ppm CO. During poisoning, adding pure hydrogen fuel increase more reaction sites for hydrogen, especially at low CO concentration. As shown in Figure 8 and 9, when an anodic inlet flow containing an H_2/CO mixture was fed into the fuel cell, CO was accumulated on the catalytic sites. The coverage of CO is much higher with 100 ppm CO, results higher total surface coverage. Nevertheless, reduces effective available catalyst sites θ_H for electro-oxidation of hydrogen.

Figure 4.10 plots the effect of CO concentration and hydrogen dilution on the distribution of liquid water saturation across the anodic catalytic layer. Figure 10 reveals that when cells are operated with 10 ppm CO, the amount of liquid water saturation greatly exceeds that when 100 ppm CO is used, at both 40% and 100% hydrogen. The presence of CO in the anodic inlet flow inhibits the reduction reactions on cathode side and declines the diffusion of water from the cathode to anode. The distribution of liquid water saturation depends more strongly on the CO concentration than on dilution of hydrogen in the anodic catalytic layer. Figure 4.11 plots the liquid water distribution across the membrane. At 10 ppm CO, 100%H_2, the effect of the electro-osmotic drag is strong and much liquid water is generated at the cathode catalyst layer, causing the liquid water distribution to have a large slop. Consequently, the CO concentration significantly influences the distribution of liquid water across the membrane. The dilution of hydrogen by the fuel reduces the gradient of the liquid water distribution because the electro-osmotic drag is small and less water is generated in the cathode catalyst layer. An increase in the CO concentration effectively reduces the gradient of liquid water distribution across the membrane.

Figure 4.12 presents the profile of liquid water saturation across the cathode catalyst layer. This figure shows that an increase in CO concentration markedly affects the liquid water saturation profile because the oxygen reduction reaction drops in the cathode catalyst layer. As the CO level increases, or the hydrogen becomes more dilute, the saturation profile becomes lower shown in Fig. 4.12, the CO content strongly affects the liquid saturation at the cathode catalyst layer. Figure 4.13 plots the ionic potential at various CO levels and hydrogen dilutions. As discussed above, the loss of ionic potential reduces the output current density. Therefore, increasing the CO level or diluting the hydrogen seriously reduces the loss of ionic potential.

Figure 4.14 compares the presented simulation results with experimental data reported by Bhatia and Wang [58]. There are four gas compositions fed into the anode. The simulation results show that the cell performance and durability depends strongly on the dilution of hydrogen and CO concentration, considerably reducing the current density and the time t_{ss} required to reach a steady state. Increasing hydrogen dilution and CO concentration degrades the performance of the cell and reduces the time t_{ss}. At a low level of CO (10 ppm CO), the cell performance depends more strongly on the dilution of hydrogen, considerably reducing the current density. The predicted CO poisoning results agree closely with the experimental values, except from the case for 10 ppm, 40% H_2. The discrepancy may be attributed without consideration for the gas diffusion layer. The assumption may probably influence the distribution of liquid water in the catalyst layers. This may explain the discrepancy between the predicted simulation results and experiments.

Figure 4.15 plots the influence of CO concentration on the time to reach the steady state for two hydrogen dilutions and cell voltages. The theoretical results indicate that a higher CO concentration results in large drop in the time to reach steady state t_{ss}. The dropping rate of t_{ss} becomes small at a large CO content. Hydrogen dilution substantially increases time t_{ss} under a wide range of CO content. At high cell voltages, a large time t_{ss} is obtained, especially at small CO content, because only a small amount of hydrogen is used at low current density, so its effect on the CO adsorption rate in the anode catalyst layer is weak. However, the cell voltage only weakly influences the time t_{ss} at high CO content. In this study, increasing the amount of pure hydrogen drastically increases t_{ss} for a wide range of CO contents.

The results for pure and 40% hydrogen at two CO contents are plotted for comparison in Figure 4.16. A higher CO content corresponds to lower t_{ss}. At 100 ppm CO, the cell voltage does not clearly affect t_{ss}. A large time t_{ss} can be achieved using pure hydrogen. At 10 ppm CO, a small difference on t_{ss} is observed at low cell voltage for pure and 40% hydrogen. Thereafter, the time t_{ss} increases markedly as the cell voltage increases for pure and 40% hydrogen at 10 ppm CO. Figure 16 reveals that a long t_{ss} can be achieved containing pure hydrogen at 10 ppm CO, especially at high cell voltage.

Table 4.1 Governing equations

Variables	ACL	MEM	CCL
C_{H_2}	$\frac{\partial}{\partial t}\left[(1-s)\varepsilon_{CL}C_{H_2}\right] = -\nabla\cdot N_{H_2} - R_{H_2}$	N/A	N/A
C_{O_2}	N/A	N/A	$\frac{\partial}{\partial t}\left[(1-s)\varepsilon_{CL}C_{O_2}\right] = -\nabla\cdot N_{O_2} - R_{O_2}$
C_{CO}	$\frac{\partial}{\partial t}\left[(1-s)\varepsilon_{CL}C_{CO}\right] = -\nabla\cdot N_{CO} - R_{CO}$	N/A	N/A
C_{wg}	$\frac{\partial}{\partial t}\left[(1-s)\varepsilon_{CL}C_{wg}\right] = -\nabla\cdot N_{wg} - R_w$	N/A	$\frac{\partial}{\partial t}\left[(1-s)\varepsilon_{CL}C_{wg}\right] = -\nabla\cdot N_{wg} - R_w$
C_{wn}	$\nabla C_{wn} = 0$	$\varepsilon_{MEM}\frac{\partial C_{wn}}{\partial t} = D_{wn}\nabla^2 C_{wn}$	$\nabla C_{wn} = 0$
s	$\frac{\varepsilon_{CL}\rho_w}{M_w}\frac{\partial s}{\partial t} = \frac{\rho_w K_{w,0}}{M_w\mu_w}\left(-\frac{dP_c}{ds}\right)\left(s\nabla^2 s + (\nabla\cdot s)^2\right) + R_w$	N/A	$\frac{\varepsilon_{CL}\rho_w}{M_w}\frac{\partial s}{\partial t} = \frac{\rho_w K_{w,0}}{M_w\mu_w}\left(-\frac{dP_c}{ds}\right)\left(s\nabla^2 s + (\nabla\cdot s)^2\right) + (4n_{d,CL}+2)R_{O_2} + R_w$
ϕ	$k_{n,eff}\nabla^2\phi - \left(R_{H_2} + R_{CO}\right) = 0$	$k_n\nabla^2\phi = 0$	$k_{n,eff}\nabla^2\phi - R_{O_2} = 0$

Table 4.2. Boundary Conditions

Variables	$x=0$	$ACL\,/\,MEM$	$MEM\,/\,CCL$	$x=L$
C_{H_2}	$C_{H_2}=C_{H_2}^{in}$	$N_{H_2}=0$	N/A	N/A
C_{O_2}	N/A	N/A	$N_{CO}=0$	$C_{O_2}=C_{O_2}^{in}$
C_{CO}	$C_{CO}=C_{CO}^{in}$	$N_{CO}=0$	N/A	N/A
C_{wg}	$C_{wg}=C_{wg}^{in}$	$N_{wg}=0$	$N_{wg}=0$	$C_{wg}=C_{wg}^{in}$
C_{wn}	N/A	$\sigma(C_a-C_{wn})=N_w$	$\frac{i}{2F}+\sigma(C_c-C_{wn})=-N_w$	N/A
s	$s=0$	$N_s=N_w$	$N_w=N_s$	$s=0$
ϕ	$\phi=0$	$k_{n,eff}\nabla\phi=k_n\nabla\phi$	$k_{n,eff}\nabla\phi=k_n\nabla\phi$	$\nabla\phi=0$

Table 4.3 The parameters used in the present model [57,58,81].

Temperature	T	353 K
Total pressure	P	1 atm
Diffusion coefficient of hydrogen in gas phase	D_{H_2}	1.1028 $(\mathrm{cm^2\ s^{-1}})$
Diffusion coefficient of oxygen in gas phase	D_{O_2}	$0.1775\times(\mathrm{T}/273.15)^{1.823}$ $(\mathrm{cm^2\ s^{-1}})$
Diffusion coefficient of vapor in gas phase	D_{wg}	$0.256\times(\mathrm{T}/307.15)^{2.334}$ $(\mathrm{cm^2\ s^{-1}})$
Thickness of catalyst layer	δ_{CL}	16 (μm)
Thickness of membrane	δ_{MEM}	50 (μm)
Gas porosity in catalyst layer	ε_{CL}	0.4
Volumetric fraction of Nafion in membrane	ε_{MEM}	0.4
Ionic conductivity	k_n	0.17 $(\mathrm{mho\ cm^{-1}})$
hydrogen adsorption rate constant	k_{fH}	100 $(\mathrm{A\ cm^{-2}\ atm^{-1}})$
ratio of forward to backward of CO adsorption	b_{fCO}	1.7×10^{-6} (atm)

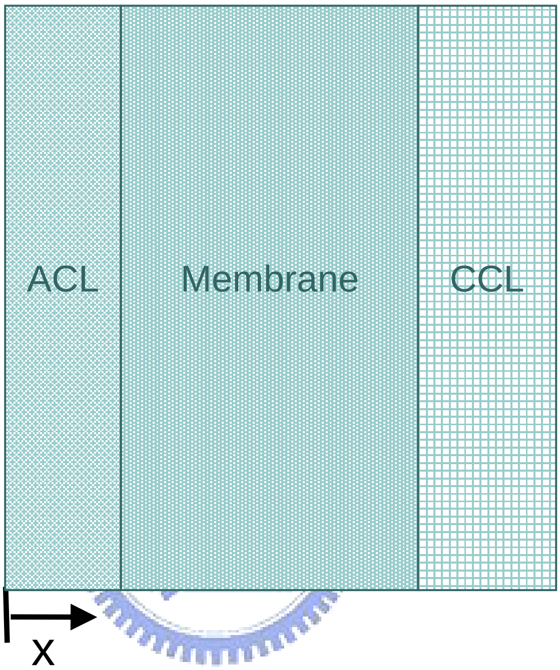

Fig. 4.1 A schematic model of the MEA of the PEM fuel cell.

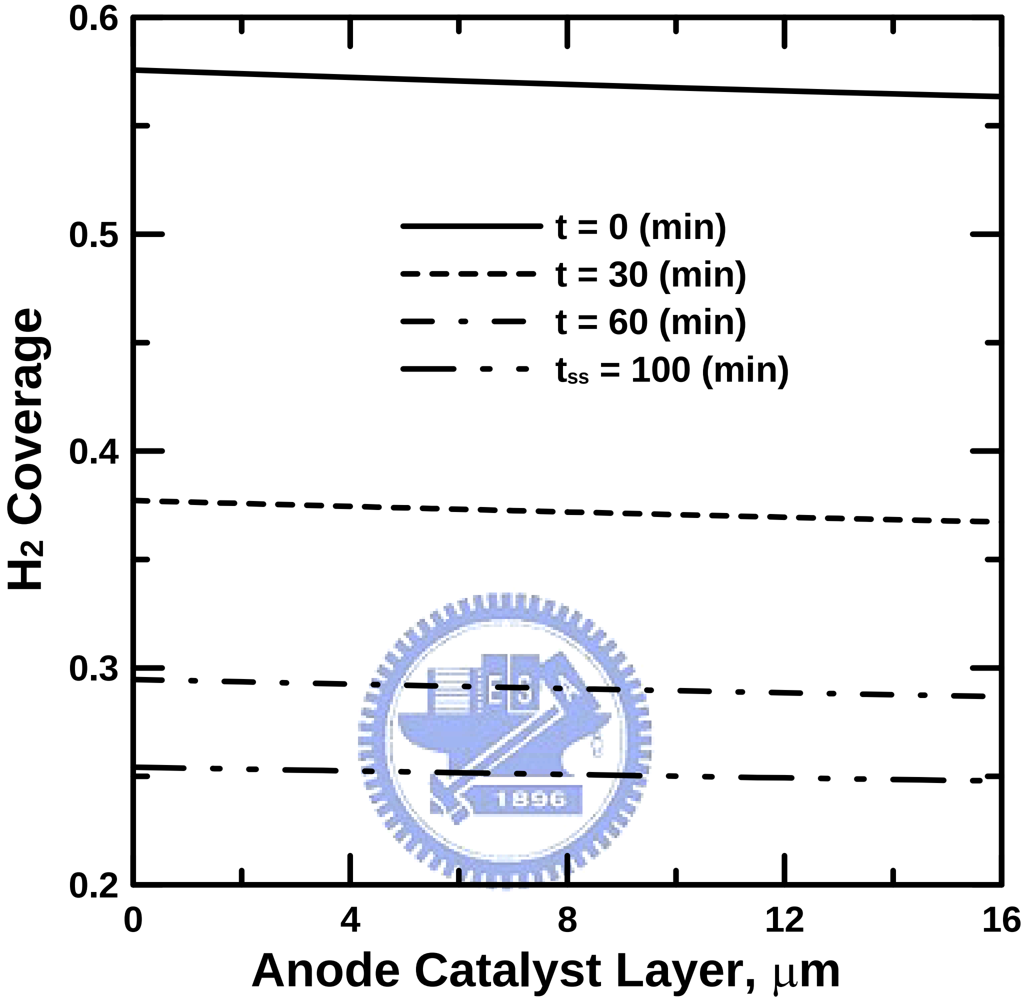

Fig. 4.2 The transient evolution of the hydrogen coverage profile across the anode catalyst layer, with 100 % H2, 10 ppm CO, 0.6 V.

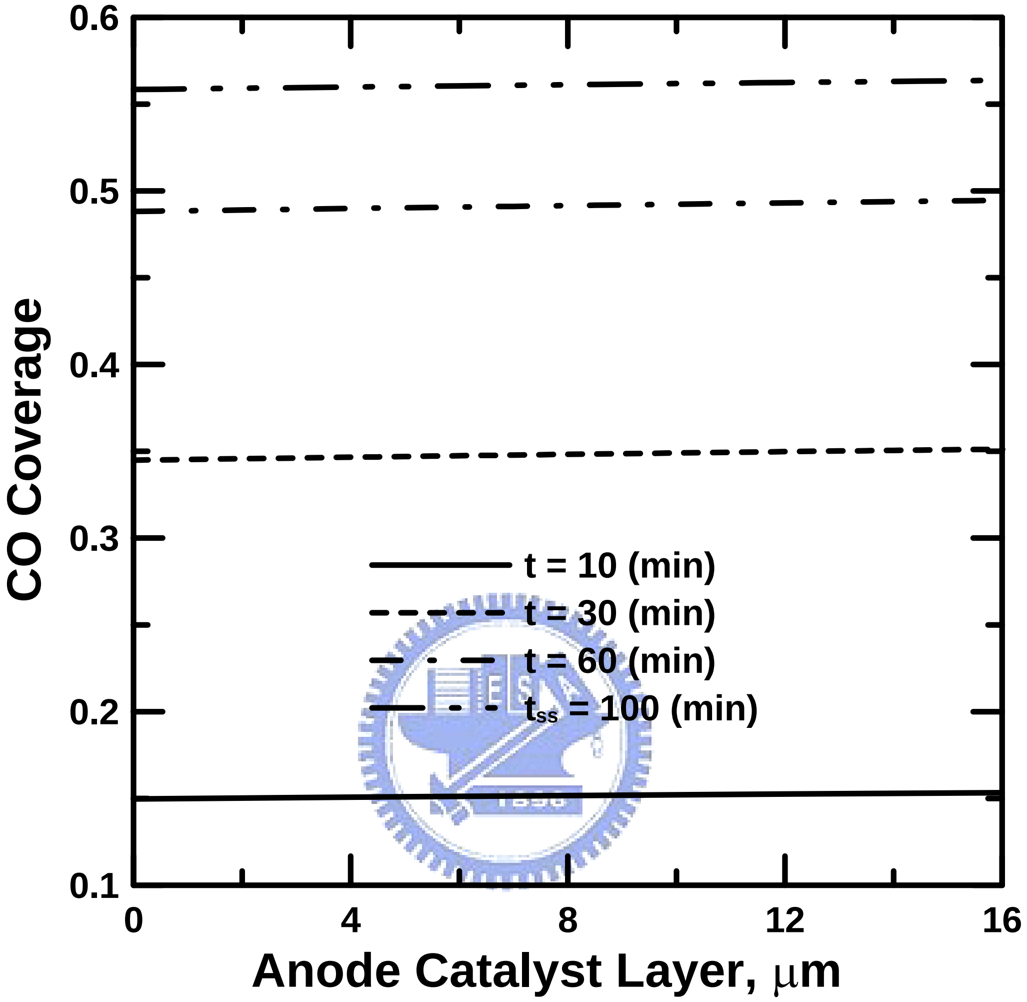

Fig. 4.3 The transient evolution of the CO coverage profile across the anode catalyst layer, with 100 % H2, 10 ppm CO, 0.6 V.

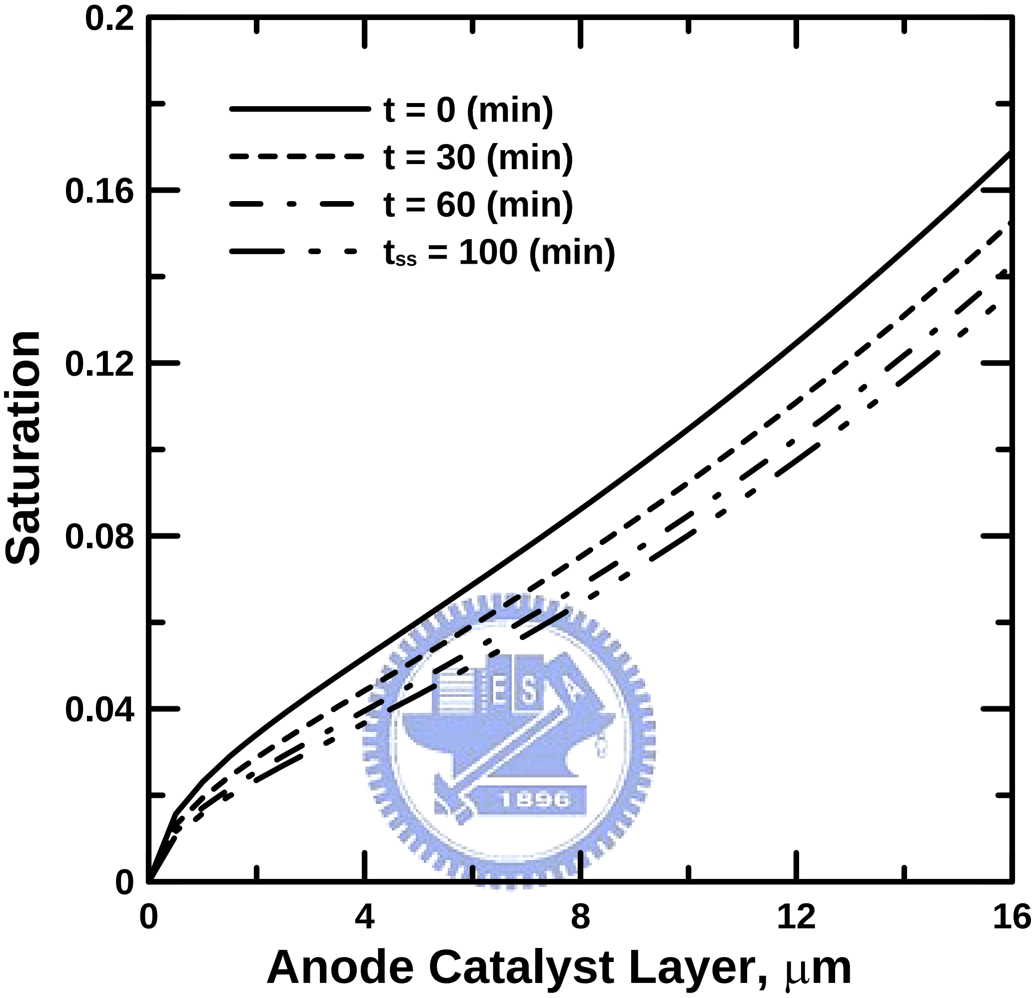

Fig. 4.4 The transient evolution of the liquid water saturation profile across the anode catalyst layer, with 100 % H2, 10 ppm CO, 0.6 V.

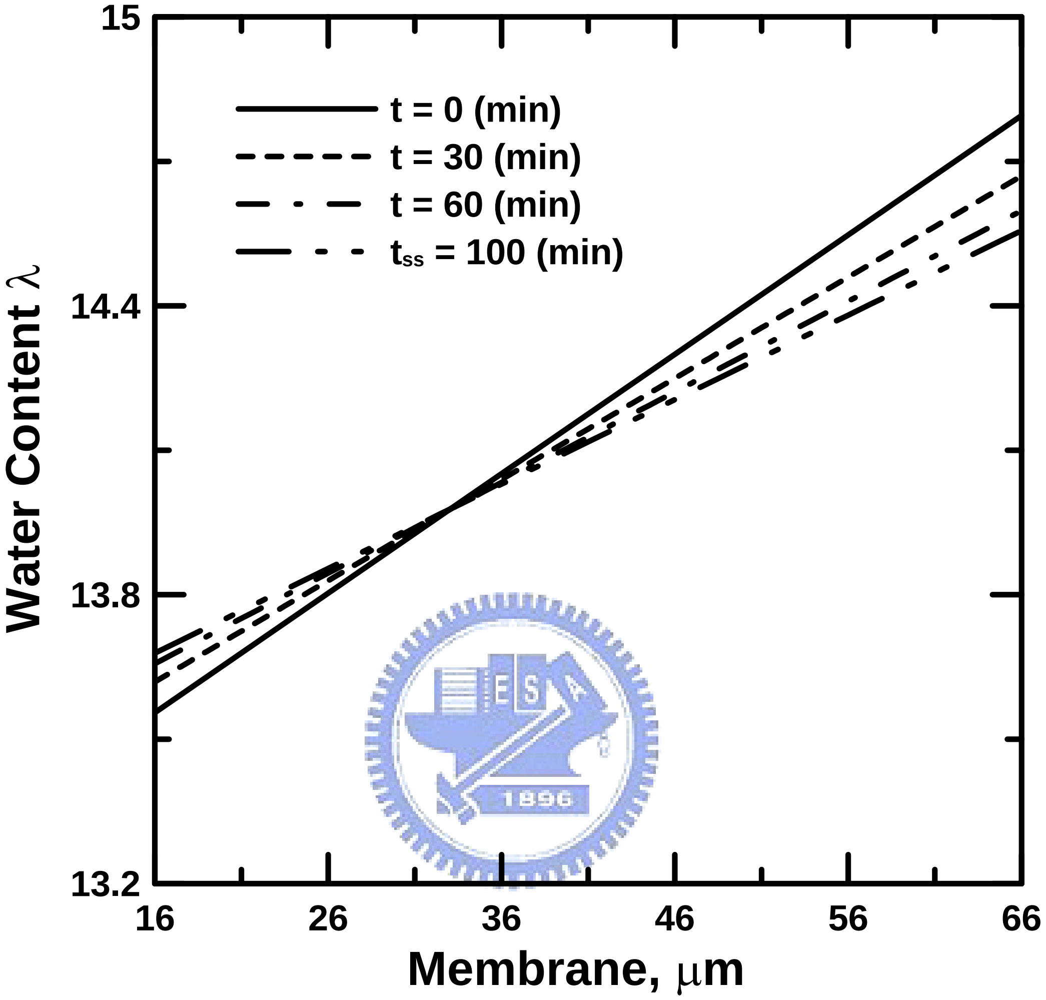

Fig. 4.5 The transient evolution of the water content profile across the membrane, with 100 % H2, 10 ppm CO, 0.6 V.

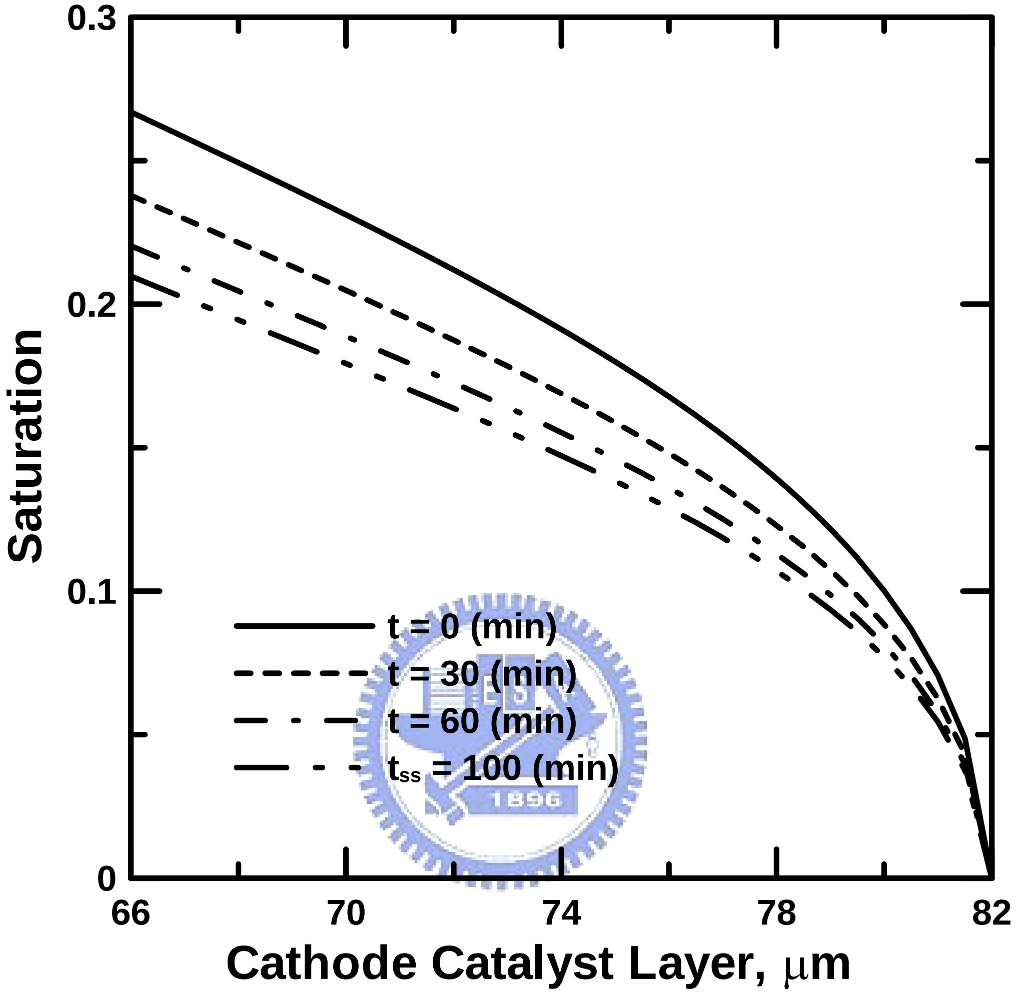

Fig. 4.6 The transient evolution of the liquid water saturation profile across the cathode catalyst layer, with 100 % H2, 10 ppm CO, 0.6 V.

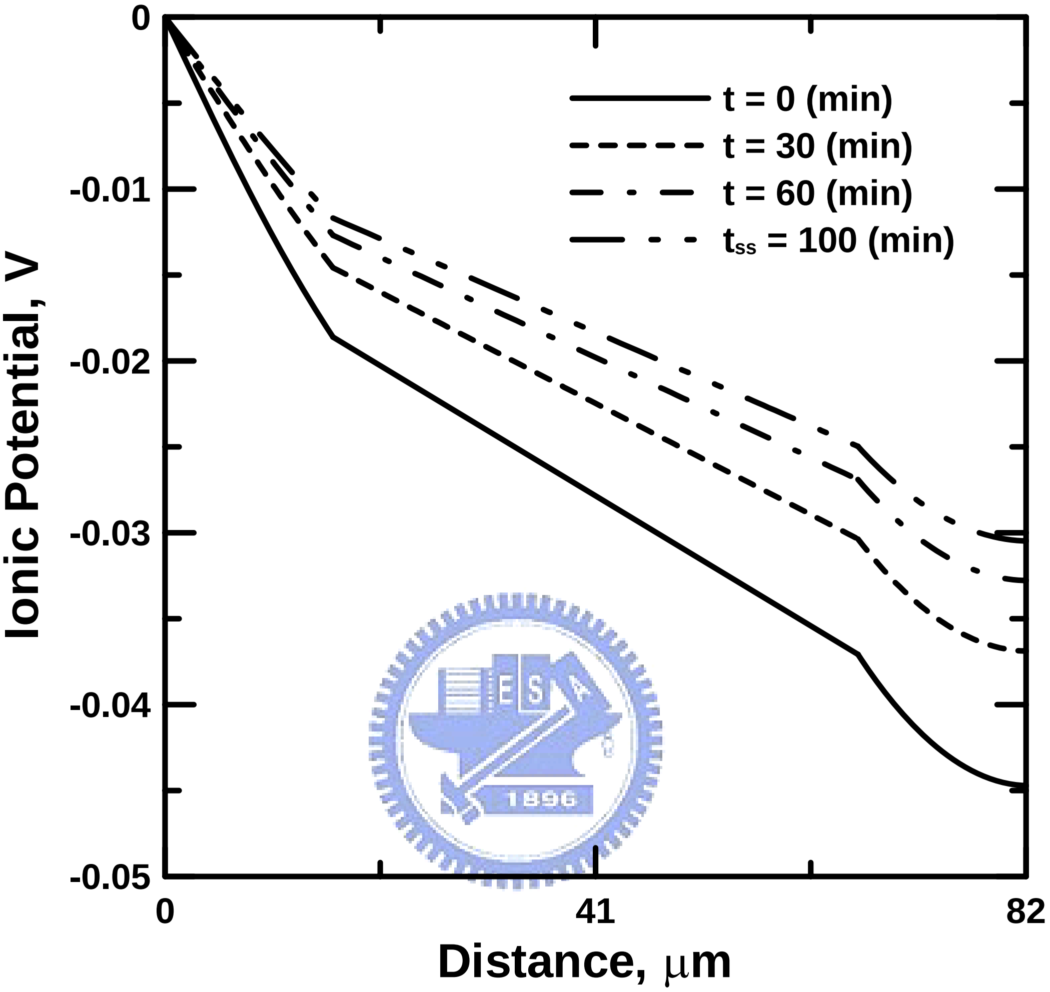

Fig. 4.7 The transient evolution of the ionic potential profile across the MEA, with 100 % H2, 10 ppm CO, 0.6 V.

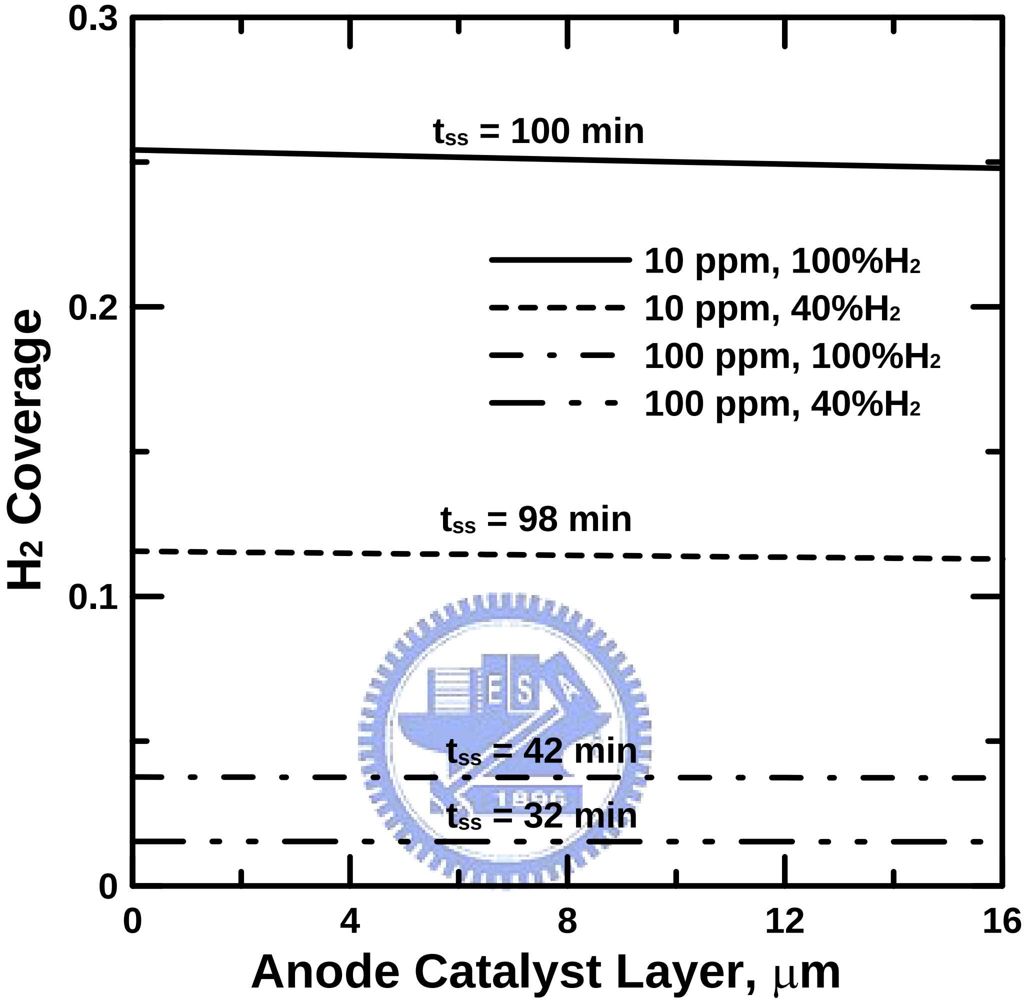

Fig. 4.8 The steady state hydrogen coverage profile across the anode catalyst layer at various CO concentrations and hydrogen dilutions at 0.6 V.

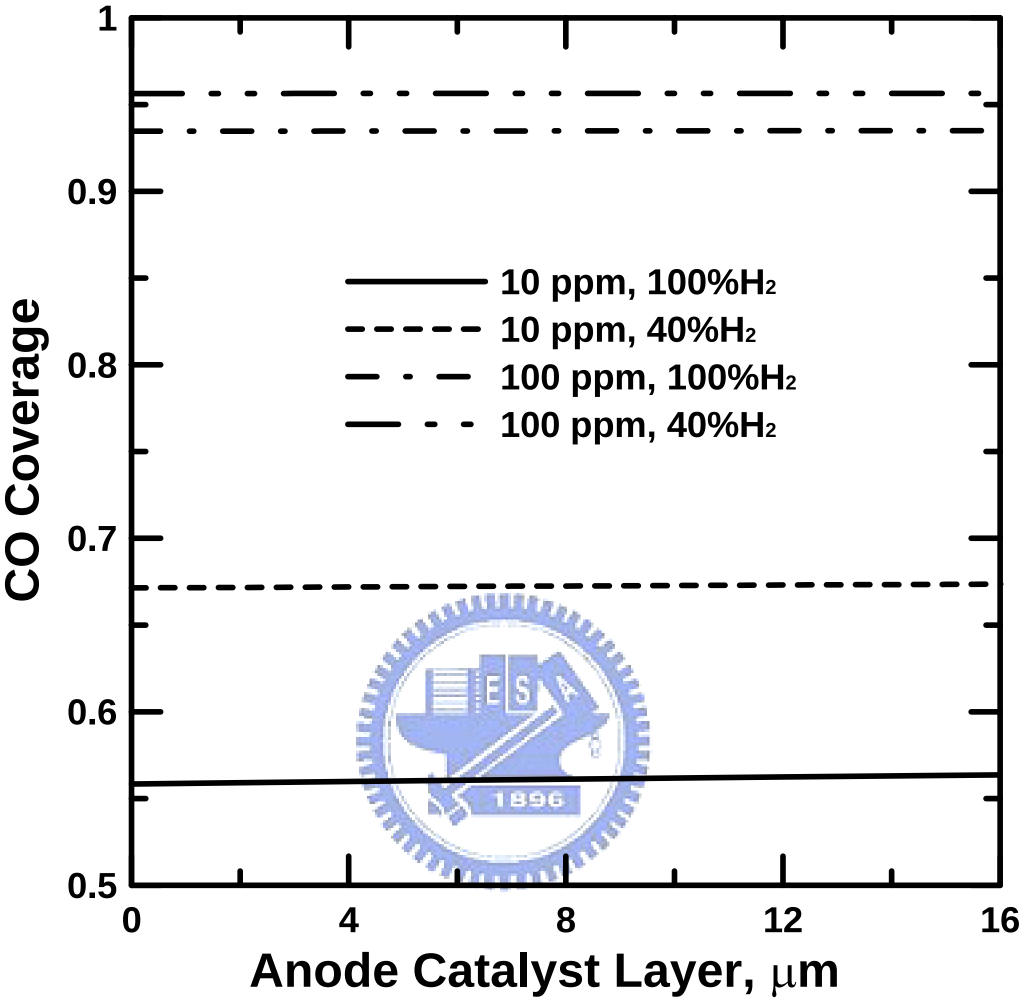

Fig. 4.9 The steady state CO coverage profile across the anode catalyst layer at various CO concentrations and hydrogen dilutions at 0.6 V.

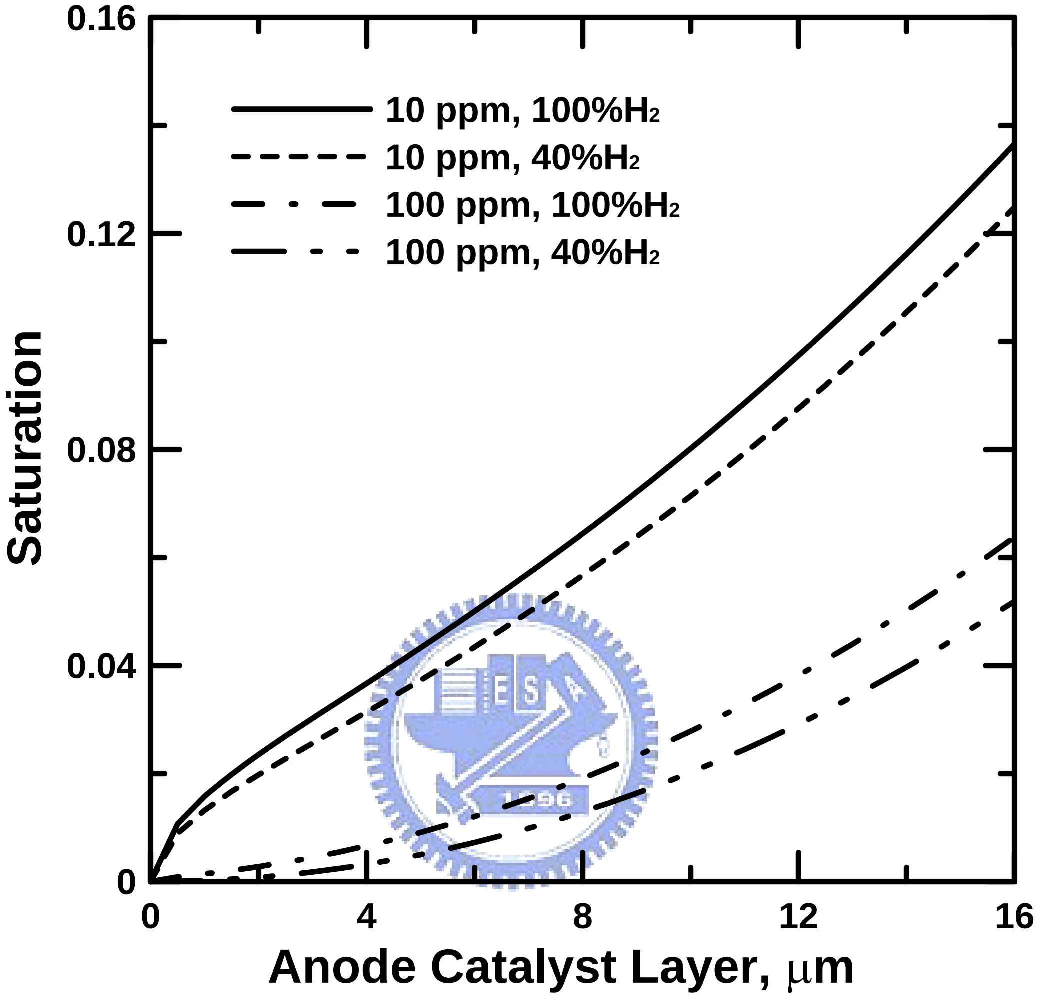

Fig. 4.10 The steady state liquid water saturation profile across the anode catalyst layer at various CO concentrations and hydrogen dilutions at 0.6 V.

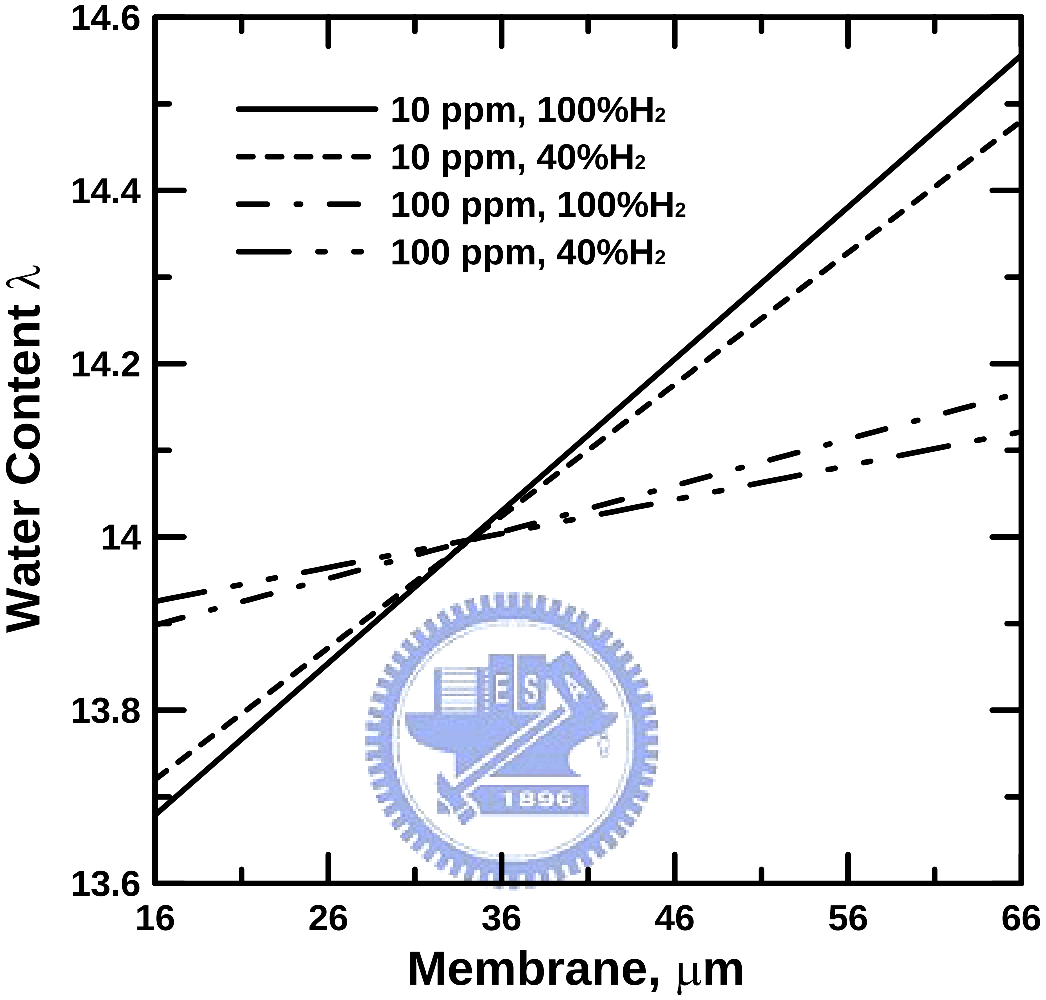

Fig. 4.11 The steady state water content profile across the membrane at various CO concentrations and hydrogen dilutions at 0.6 V.

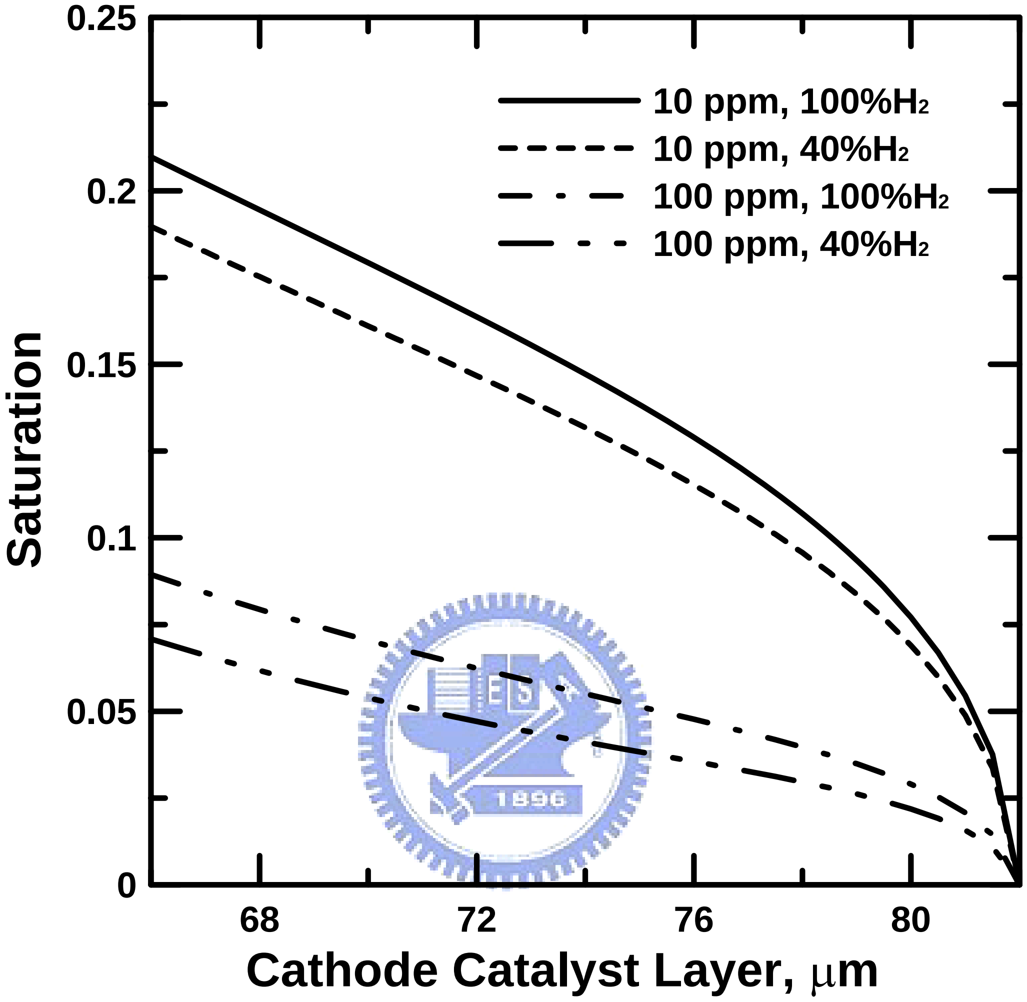

Fig. 4.12 The steady state liquid water saturation profile across the cathode catalyst layer at various CO concentrations and hydrogen dilutions at 0.6 V.

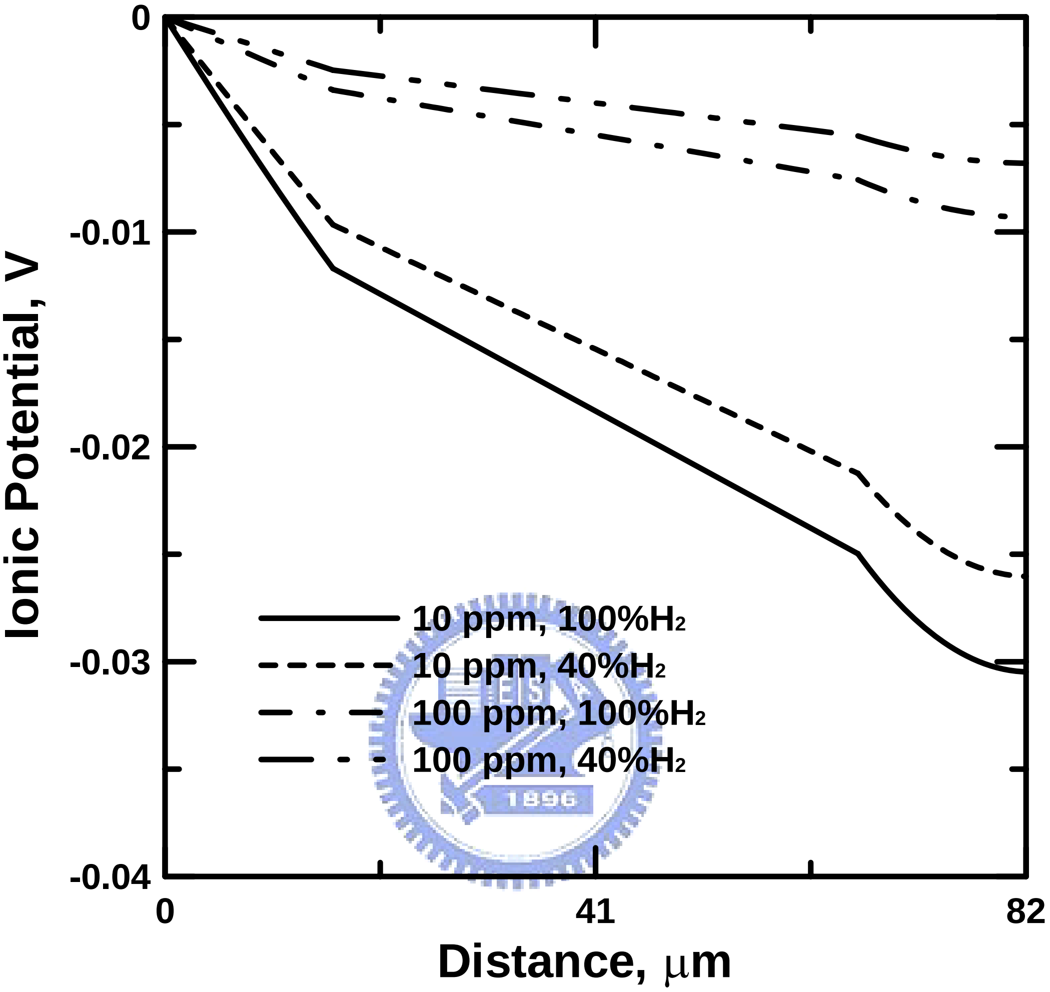

Fig. 4.13 The steady state ionic potential profile across the MEA at various CO concentrations and hydrogen dilutions at 0.6 V.

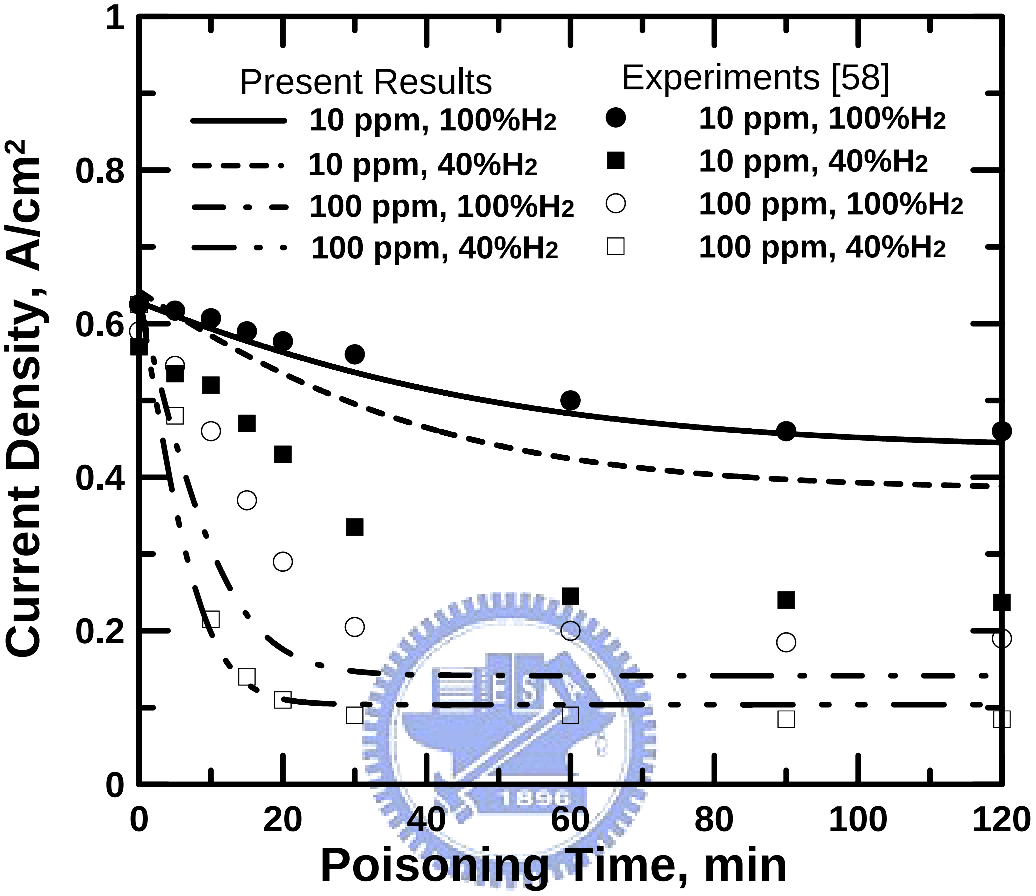

Fig. 4.14 The present simulation results compare with experimental data at 0.6 V.

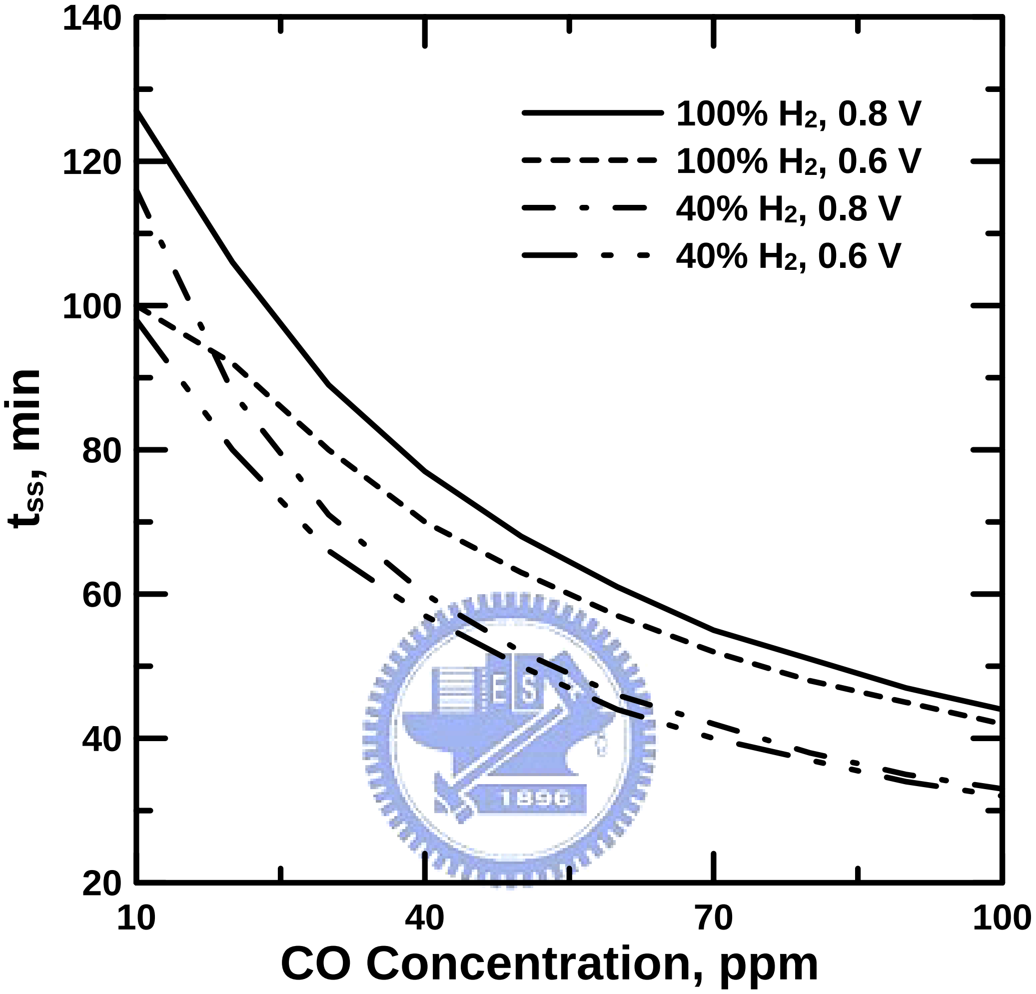

Fig. 15 The influence of CO concentration on the time to reach steady state for two hydrogen dilutions and cell voltages.

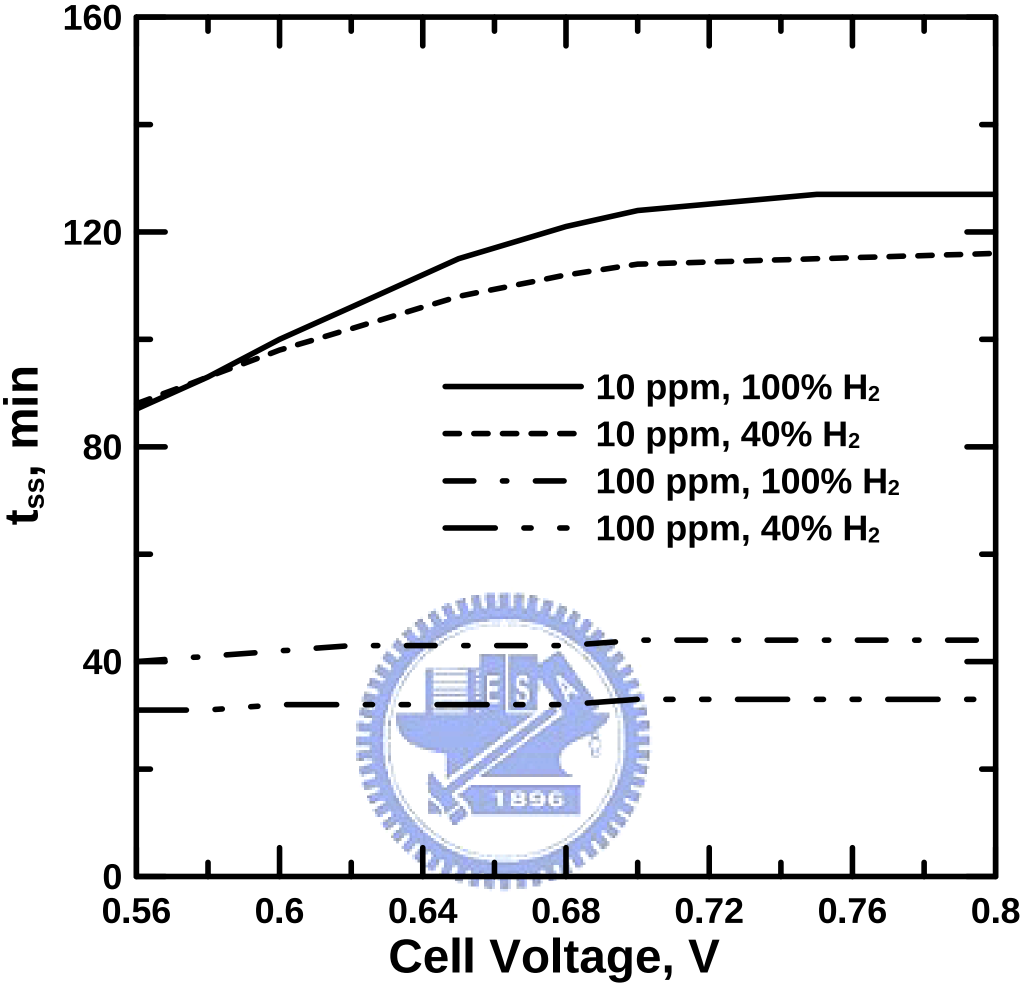

Fig. 4.16 The effect of cell voltage on the time to reach steady state for two hydrogen dilutions and CO concentrations.

5. Transient Evolution of Carbon Monoxide Poisoning Effect of PBI Membrane Fuel Cells

High temperature polybenzimidazole membrane fuel cells are the focus of attention due to high CO tolerance and overcoming water managements. This study develops a transient, one-dimensional mathematical model to predict CO tolerance, and validates it with experiments. Experimental results are measured at different temperatures. Fuel cell performance degradations with time are also measured under various fuel compositions. Transient evolutions of current density, H_2 coverage, CO coverage, and ionic potential are shown during the CO poisoning process. The theoretical results show that hydrogen coverage decreases with time, reducing hydrogen oxidation reactions and dropping ionic potential loss. The effects of temperature, CO contents, and H_2 dilutions on fuel cell performance and the time to reach steady t_{ss} are all investigated. Predictions of fuel cell current density degradation also show good agreement with experimental results.

5.1 Experiments

The experiments use a five-layered membrane electrode assembly with PBI membrane, Pt catalyst, and carbon papers. Total thickness of the MEA is 971 μm and a 45.2 cm^2 active area. Figure 5.1 shows the component diagram of a single cell. The end plates were made by aluminum alloy with isolated treatment to give rigid support. The serpentine flow channels were manufactured on graphite plates with 1×1 mm^2 channel sizes.

The experimental setup schematic diagram for a single cell is shown in Figure 5.2. Inlet gases are supplied via model PC-540 mass flow controller (Protec Instruments, Inc.). High power electronic load model 3316-04 is made by Prodigit Electronics Co., Ltd. The ITRI test station measures polarization curves and other experimental results. The total mean square error is about ± 1.497 % as shown in table 5.1. Fuel cells are operated without gas humidification, resulting in simpler operation processes and avoiding water management problems, such as flooding and membrane dehydration. Fuel cell operating temperature is around 120~180^{o}C through YSC (GX-36) temperature controllers to maintain desired operating temperature. Temperature below water boiling temperature can cause phosphoric acid dissolution in liquid water and drop membrane conductivity. The time required for MEA activation is generally 30~50 hours at a given constant current density (0.2 A/cm^2) with a maximum stoichiometric of λ=2.5 during start-up for both the anode and cathode side.

Fuel cell testing is performed under various gas mixtures, 1~3%CO, 40~55%H_2, 20%CO_2, otherwise N_2. Pure hydrogen and air are applied to anode and cathode respectively until fuel cell reaches steady state. Then, a CO mixed stream replaces pure hydrogen.

5.2 Theoretical model

A three layer mathematical model developed in this work analyzes the transient CO poisoning process of high temperature PBI membrane fuel cells. An MEA schematic model is shown in Figure 4.1, representing the anode catalyst layer, membrane, and cathode catalyst layer. Some basic assumptions were made as following:

1. Unsteady state.
2. One dimensional Cartesian coordinate system.
3. Isothermal and isobaric.

4. Ideal gas.
5. Catalyst layer and membrane are isotropic.
6. Only diffusion mechanism is considered.
7. Physical domain includes anode catalyst layer, membrane and cathode catalyst layer.
8. Water inside the fuel cell can be treated as a vapor phase.

Table 5.2 represents all the governing equations. Gas species transport at the catalyst layers is described as

$$N_i = -D_i \varepsilon_{CL}^{1.5} \nabla C_i \tag{5-1}$$

where N_i represents flux of gas species including hydrogen, oxygen, and carbon monoxide, ε_{CL} is the porosity at both the anode and the cathode catalyst layer and C_i expresses concentration of gases. Fuel, oxidant and carbon monoxide transport can be expressed as

$$\frac{\partial}{\partial t}\left[\varepsilon_{CL} C_i\right] = -\nabla \cdot N_i - R_i \tag{5-2}$$

Protons are produced from hydrogen oxidation reactions at the anode catalyst layer and then transport toward the fuel cell cathode through the membrane. Current density at the membrane can be expressed as:

$$i = -k_n \nabla \phi \tag{5-3}$$

in which k_n is the membrane conductivity and ϕ is the electrolytic phase potential [27]. Water inside the fuel cell can be treated as a vapor phase because PBI membrane fuel cells work higher than 120°C. Thus, the represented hydrogen and carbon monoxide current densities can be modified from [56]:

$$\frac{di_{H_2}}{dx} = 2ak_{eH}\theta_{H_2} \sinh\left(\frac{n_{H_2} F\left(\phi_s - \phi - U_0\right)}{2RT}\right) \tag{5-4}$$

$$\frac{di_{CO}}{dx} = 2ak_{eCO}\theta_{CO}\sinh\left(\frac{n_{CO}F\left(\phi_s-\phi-U_0\right)}{2RT}\right) \tag{5-5}$$

where k_{eH} and k_{eCO} are the rate constants of hydrogen and CO electro-oxidation, The calculations of unsteady state θ_{H2} and θ_{CO} can be referred to [56]. The forward rate constant of hydrogen k_{fH} and CO adsorption-to-desorption rate ratios b_{fc} are expressed as:

$$k_{fH} = k_{fH0}\cdot\exp\left[-\frac{\delta\left(\varDelta E_H\right)}{RT}\left(1-\exp\left(\frac{\lambda\theta_{CO}}{\theta_{CO}-1}\right)\right)\right] \tag{5-6}$$

$$b_{fCO} = b_{fCO0}\cdot\exp\left[\frac{\delta\left(\varDelta G_{CO}\right)}{RT}\theta_{CO}\right] \tag{5-7}$$

The reaction rates of hydrogen and carbon monoxide are expressed as:

$$R_{H_2} = \frac{di_{H_2}}{dz}\left(\frac{\gamma_{H_2}}{n_{H_2}F}\right) \tag{5-8}$$

$$R_{CO} = \frac{di_{CO}}{dz}\left(\frac{\gamma_{CO}}{n_{CO}F}\right) \tag{5-9}$$

where γ and n represent stoichiometric ratio and number of electrons, respectively. Oxygen reaction rate at the cathode catalyst layer is given by:

$$R_{O_2} = \frac{1}{4F}\left(1-\bar{\theta}_{CO}\right)ai_0\left[\frac{C_{O_2}}{C_{O_2\,ref}}\exp\left(\frac{-F\left(\phi_s-\phi-U_0\right)}{RT}\right)\right] \tag{5-10}$$

Table 5.3 lists the corresponding boundary conditions applied in the numerical computation. Table 5.4 shows the parameters used in this work. The steady-state condition is defined as the relative error of current density reaches:

$$\frac{i^{n+1}-i^{n}}{i^{n}} \le 10^{-3} \tag{5-11}$$

in which i^n represents current density at nth minute. The governing equations were solved by using implicit scheme. The 4th order Runge Kutta method was applied to solved hydrogen and carbon monoxide coverage.

5.3 Results and Discussion

Higher temperature fuel cells are expected to have higher CO tolerance because faster chemical kinetics facilitate CO desorption on the Pt catalyst. Further advantages such as without water-gas-shift reaction, preferential oxidation, and water management can obviously simplify the fuel cell system and lower cost. Theoretical and experimental studies both investigated the transportation of phosphoric acid doped PBI membrane fuel cells. Figure 5.3 shows the transient evolution of hydrogen coverage in the anode catalyst layer with time under 55% H_2 containing 1% CO. Fuel cell operates without carbon monoxide poisoning when time equals zero. Hydrogen currently occupies the highest reaction surface on platinum catalysts, gradually decreasing with time. Strong chemical bonding favors CO adsorption on the Pt catalyst. At t=0, hydrogen coverage decreases from 0.52 to 0.37 at steady state. Thus, cell performance decreases with decreasing hydrogen coverage. Figure 5.4 shows opposite trends and depicts CO coverage across the anode catalyst layer. CO coverage is initially at zero and reaches 0.29 until steady state.

Figure 5.5 depicts variations of ionic potential profiles across MEA with time. Linear ionic potential profiles are shown since constant ionic conductivity is assumed and protons are not consumed across the membrane. Ionic potential shows nonlinear profiles in the cathode catalyst layer due to oxidant consumption by reduction reactions. Ionic potential loss decreases with time during the CO poisoning process, lowering cell current density. Figure 5.6 represents the distribution of θ_{H2} under various hydrogen dilutions with 1% CO in the anode catalyst layer. At 40% hydrogen, θ_{H2} has the lowest value and obviously increases with hydrogen content. A larger amount of hydrogen can cover more catalyst reaction surfaces. Increased hydrogen content at higher hydrogen dilution can increase a greater amount of hydrogen coverage than at lower hydrogen dilution. CO coverage under various hydrogen contents reveals opposite trends shown in Figure 5.7. At lower hydrogen content, CO has more opportunity to cover Pt catalysts. Hydrogen dilution by comparison, has much more significant effect on θ_{H2} than on θ_{CO}.

Inlet fuel containing CO can decrease cell performance with time. Figure 5.8 illustrates time to reach steady state t_{ss} under different fuel compositions. CO concentration amounts range from 0.1% to 3% with 40% to 80% hydrogen content. The figure shows that t_{ss} dramatically decreases with increased CO content. High CO concentrations greater than 1% show a much smaller drop rate of t_{ss}. Different hydrogen contents show similar trends. Inlet fuel containing more than 1% CO shows only slight difference in time to reach steady state. Hydrogen dilution effect at low CO concentrations does not show significant difference on time t_{ss}, but gradually increases with CO amount. Increasing hydrogen amount, especially at higher CO concentrations, can obviously increase the time t_{ss}.

Figure 5.9 plots CO and hydrogen concentration influence on cell current density. Theoretical results show that increased CO concentrations from 0.1% to 3% can dramatically drop cell current density due to greater CO adsorption on Pt catalysts. Also, CO desorption does not easily occur due to strong chemical bonding between CO and Pt, thus accumulating on the catalysts. Increased hydrogen content does not cause significant fuel cell performance improvement with 0.1% CO. However, hydrogen dilution effect becomes much more significant with increasing CO concentration. At 3% CO, a significant increase of fuel cell current density is obtained with increasing hydrogen content from 40% to 80%. Similar hydrogen dilution trends are also shown on time t_{ss}. Figure 5.10 shows percentage of energy loss of fuel cell power density under various fuel compositions. A wide range of fuel compositions, including CO and hydrogen content, are considered as important design parameters of methanol reformers. This figure allows for easy reformer specification and convenient performance prediction of designing fuel cells.

Experimental measurements of PBI membrane fuel cell polarization curves at temperature 120, 140, 160 and 180^{o}C are depicted in Figure 5.11. Experiments were all conducted under atmospheric pressure. Fuel and oxidant were fed into the cell directly without extra humidification. The measurements were performed at a stoichiometric ratio of 2.0 of the anode and cathode. Fuel and oxidant were applied with pure hydrogen and air, respectively. Highest performance is seen at temperature 180^{o}C and significantly decreases with temperature drop. This is because membrane conductivity increases at higher temperature. Electrode kinetics also becomes faster at higher temperature. Membrane dehydration is not shown at elevated temperature of PBI membrane fuel cell. Figure 5.12 plots simulation result comparisons with experimental data. Fuel cell performance degradation with time is shown under various fuel compositions containing 1 to 3% CO and 40 to 55% H_2. Transient evolutions of cell performance are accurately predicted from simulations and also measured by experiments. Current density drops with time and reaches steady state in a few minutes. Good agreements are plotted in this figure. The simulation from this work can accurately predict fuel cell performance under various fuel compositions and realize transient degradations of fuel cell performance, thus providing sufficient information for the designing reformer and fuel cell system. Experimental studies provide further understanding of the PBI membrane fuel cell and demonstrate the theoretical results.

Table 5.1 Error analysis of the ITRI test station.

	Range	Error
Voltage	0~60 V	± 0.05 %
Current	0~60 A	± 0.167 %
Mass flow controller	10~2000 sccm	± 1 %
Temperature controller	120~180°C	± 1.1 %
Total mean square error	± 1.497 %	

Table 5.2 Governing equations

Variables	ACL	MEM	CCL
C_{H_2}	$\frac{\partial}{\partial t}\left[\varepsilon_{CL} C_{H_2}\right] = -\nabla \cdot N_{H_2} - R_{H_2}$	N/A	N/A
C_{O_2}	N/A	N/A	$\frac{\partial}{\partial t}\left[\varepsilon_{CL} C_{O_2}\right] = -\nabla \cdot N_{O_2} - R_{O_2}$
C_{CO}	$\frac{\partial}{\partial t}\left[\varepsilon_{CL} C_{CO}\right] = -\nabla \cdot N_{CO} - R_{CO}$	N/A	N/A
ϕ	$k_{n,eff} \nabla^2 \phi - \left(R_{H_2} + R_{CO}\right) = 0$	$k_n \nabla^2 \phi = 0$	$k_{n,eff} \nabla^2 \phi - R_{O_2} = 0$

Table 5.3 Boundary Conditions

Variables	$x=0$	$ACL\,/\,MEM$	$MEM\,/\,CCL$	$x=L$
C_{H_2}	$C_{H_2}=C_{H_2}^{in}$	$N_{H_2}=0$	N/A	N/A
C_{O_2}	N/A	N/A	$N_{O_2}=0$	$C_{O_2}=C_{O_2}^{in}$
C_{CO}	$C_{CO}=C_{CO}^{in}$	$N_{CO}=0$	N/A	N/A
ϕ	$\phi=0$	$k_{n,eff}\nabla\phi=k_n\nabla\phi$	$k_{n,eff}\nabla\phi=k_n\nabla\phi$	$\nabla\phi=0$

Table 5.4 The parameters used in the present theoretical model [58,77,81].

Temperature	T	453 K
Total pressure	P	1 atm
Diffusion coefficient of hydrogen in gas phase	D_{H_2}	1.1028 (cm^2 s^{-1})
Diffusion coefficient of oxygen in gas phase	D_{O_2}	$0.1775\times(T/273.15)^{1.823}$ (cm^2 s^{-1})
Thickness of catalyst layer	δ_{CL}	20 (μm)
Thickness of membrane	δ_{MEM}	30 (μm)
Gas porosity in catalyst layer	ε_{CL}	0.4
Ionic conductivity	k_n	0.09 (mho cm^{-1})

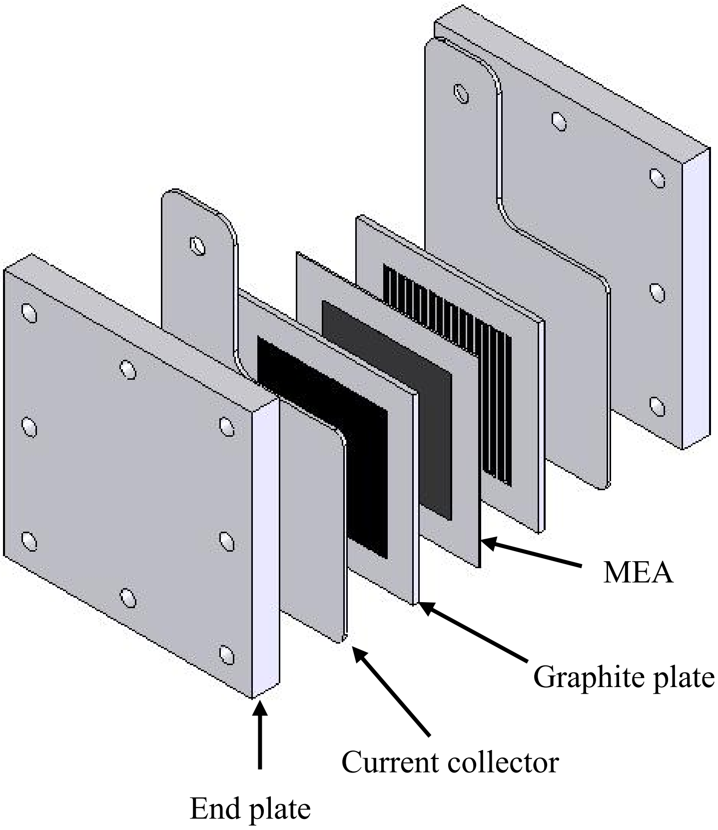

Fig. 5.1 Component diagram of a single cell

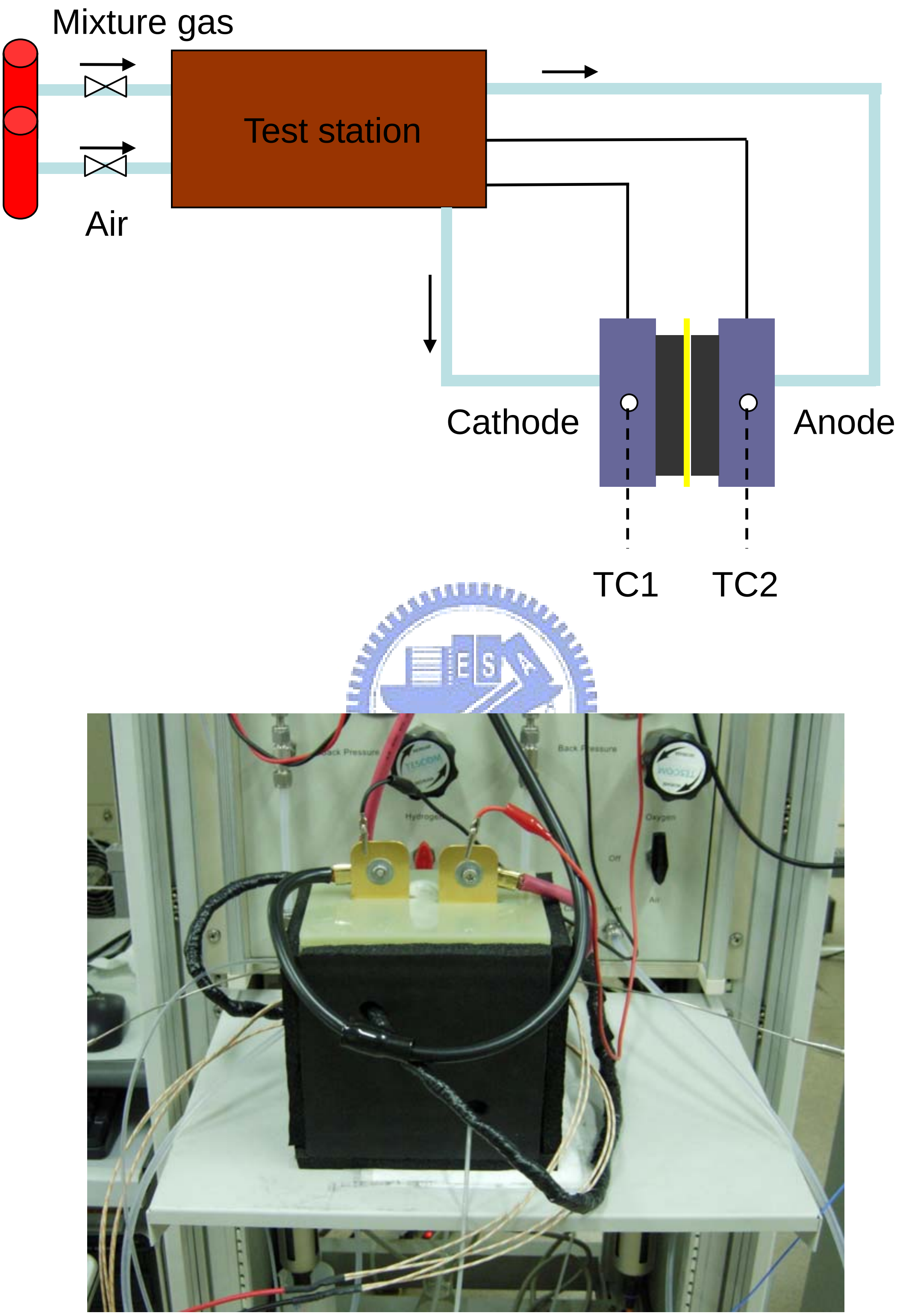

Fig. 5.2 Schematic of the experimental setup

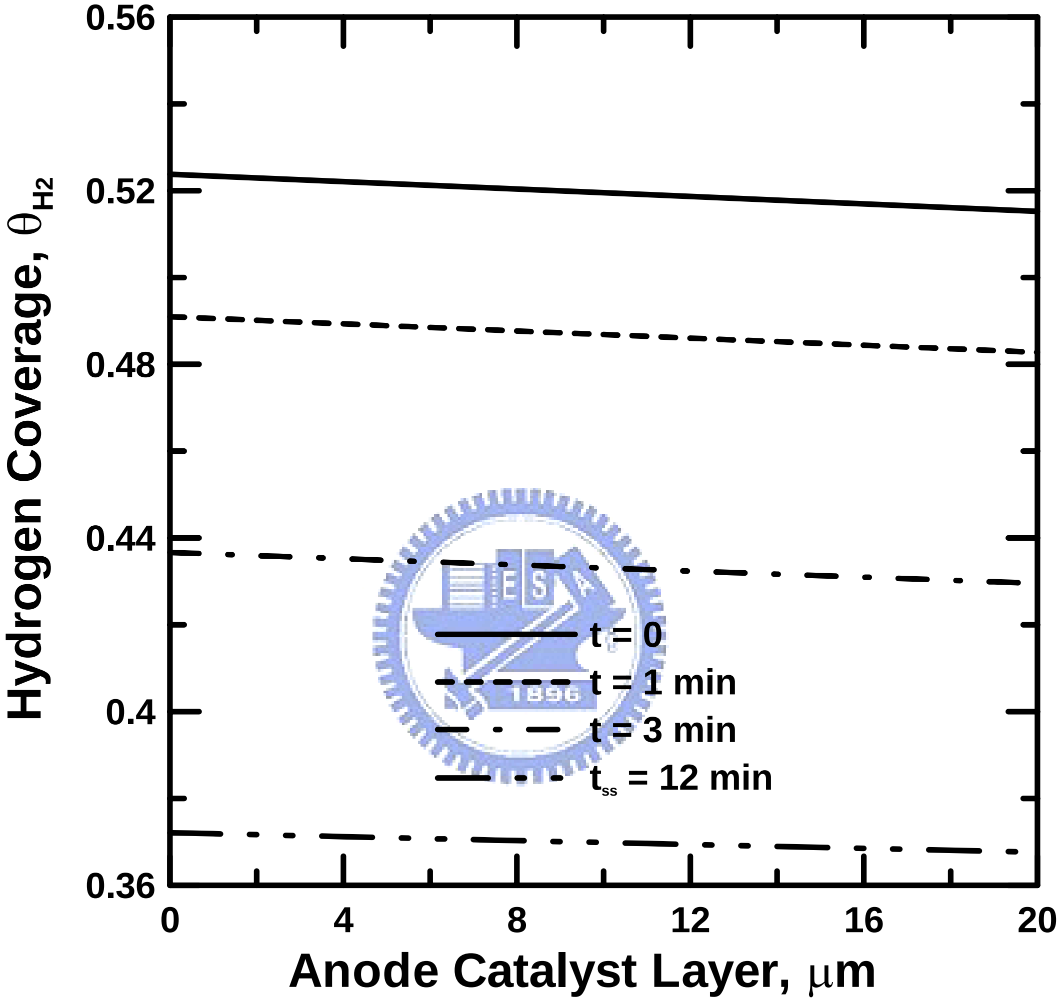

Fig. 5.3 Transient evolution of hydrogen coverage profiles across anode catalyst layer with 1% CO, 55% H_2 at 0.6 V, 180°C.

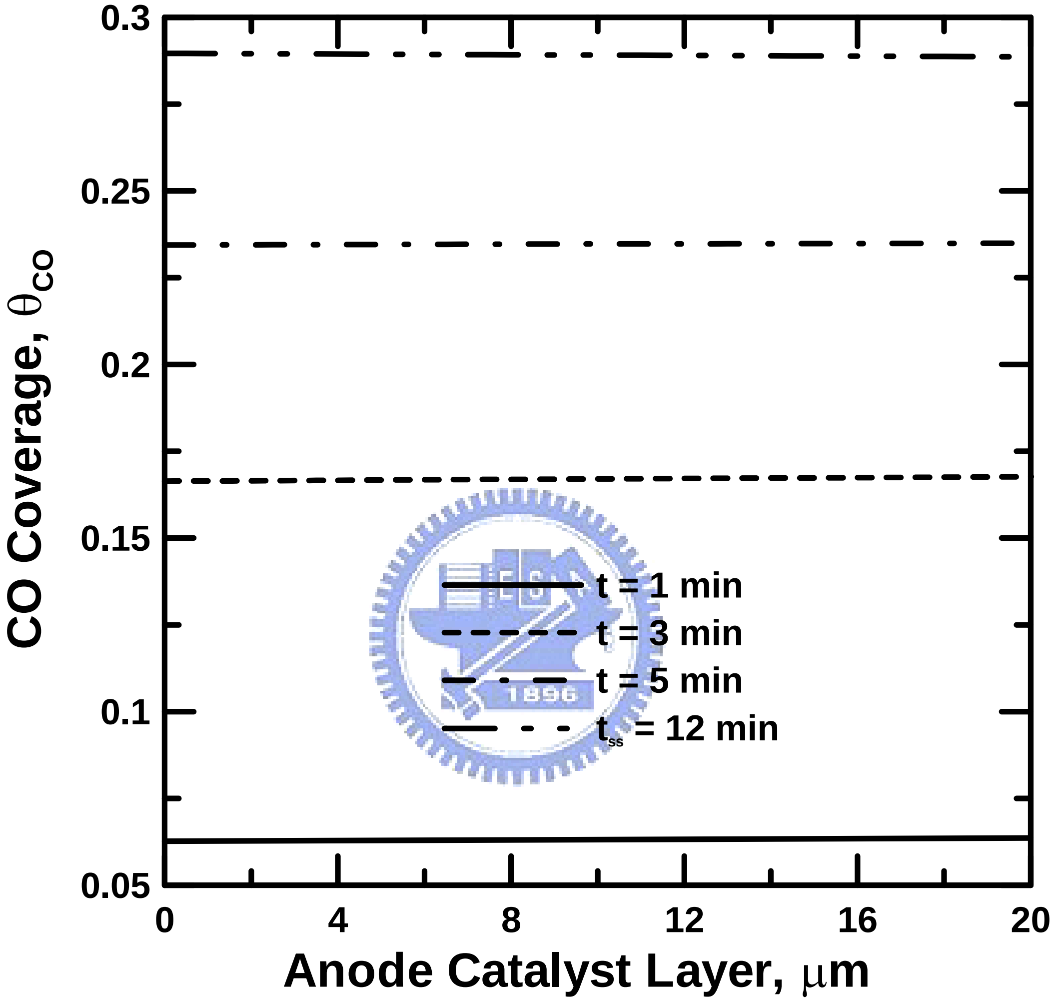

Fig. 5.4 Transient evolution of CO coverage profiles across anode catalyst layer with 1% CO, 55% H_2 at 0.6 V, 180°C.

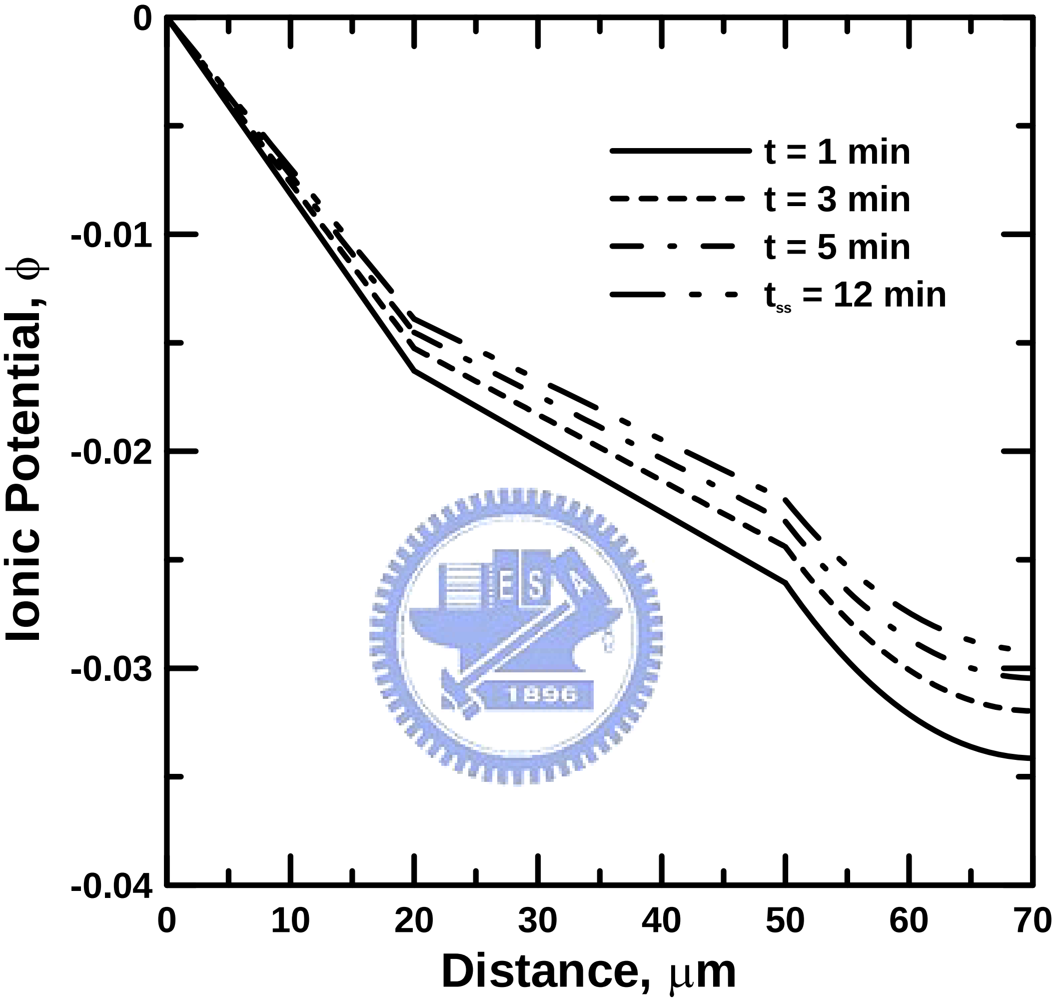

Fig. 5.5 The distributions of ionic potential loss with time across MEA with 1% CO, 55% H_2 at 0.6 V, 180°C.

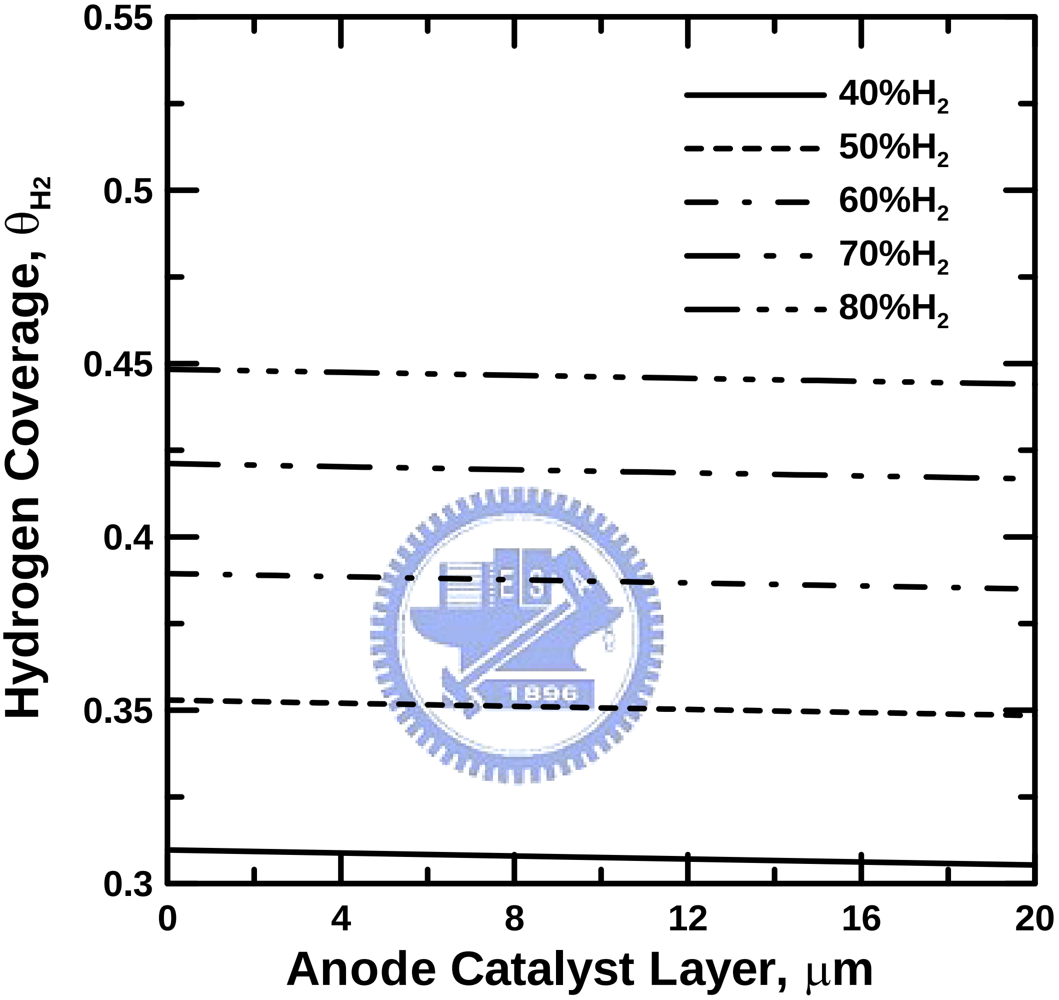

Fig. 5.6 Hydrogen coverage profiles across anode catalyst layer under various hydrogen contents with 1% CO at 0.6 V, 180°C.

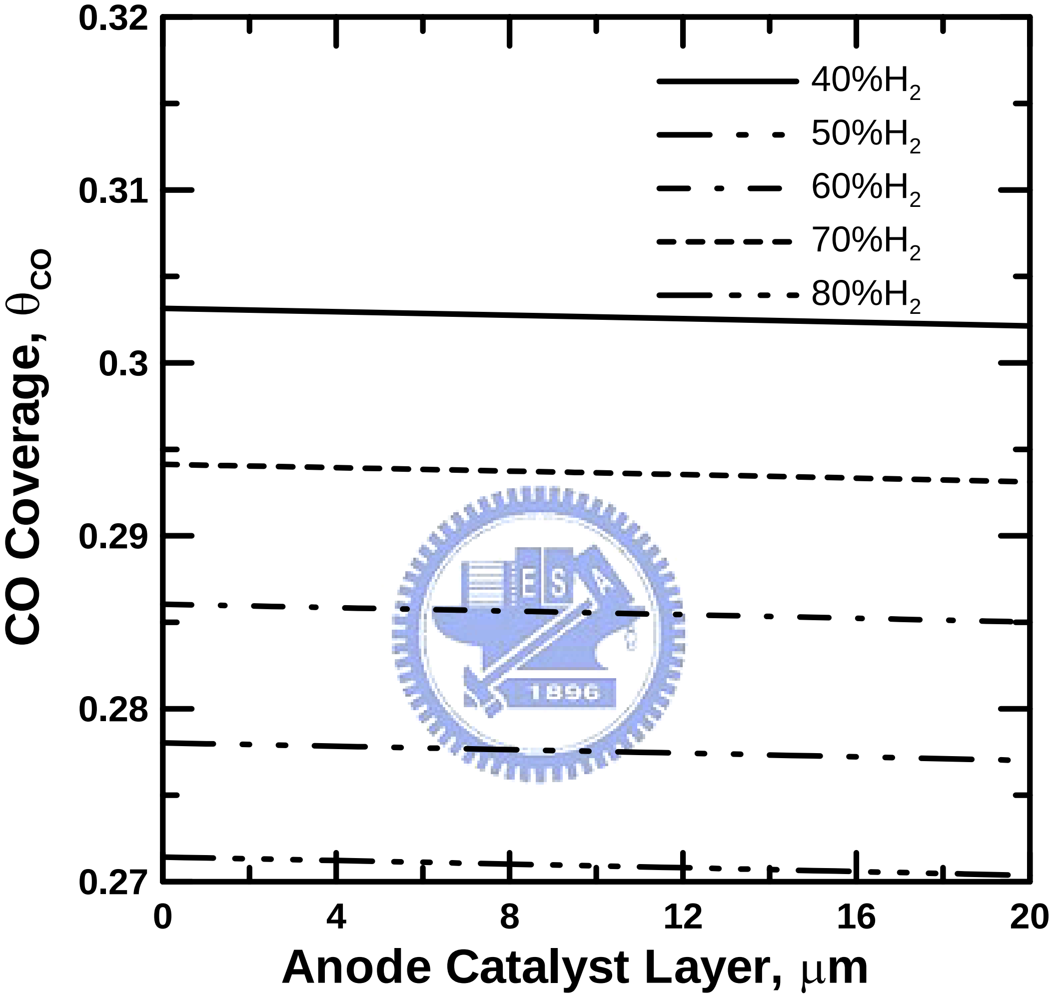

Fig. 5.7 CO coverage profiles across anode catalyst layer under various hydrogen contents with 1% CO at 0.6 V, 180°C.

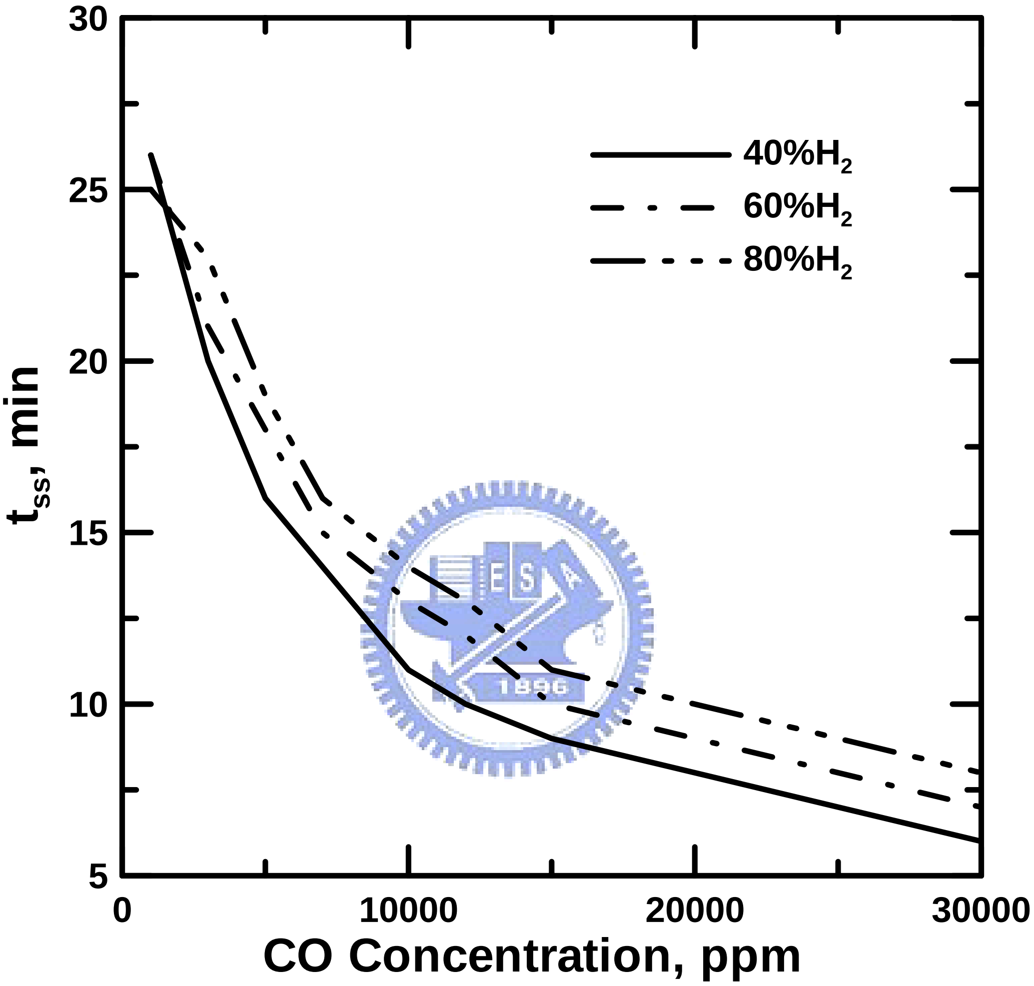

Fig.5.8 Effects of CO contents on the time to reach steady state under various hydrogen dilutions at 0.6 V, 180^{o}C.

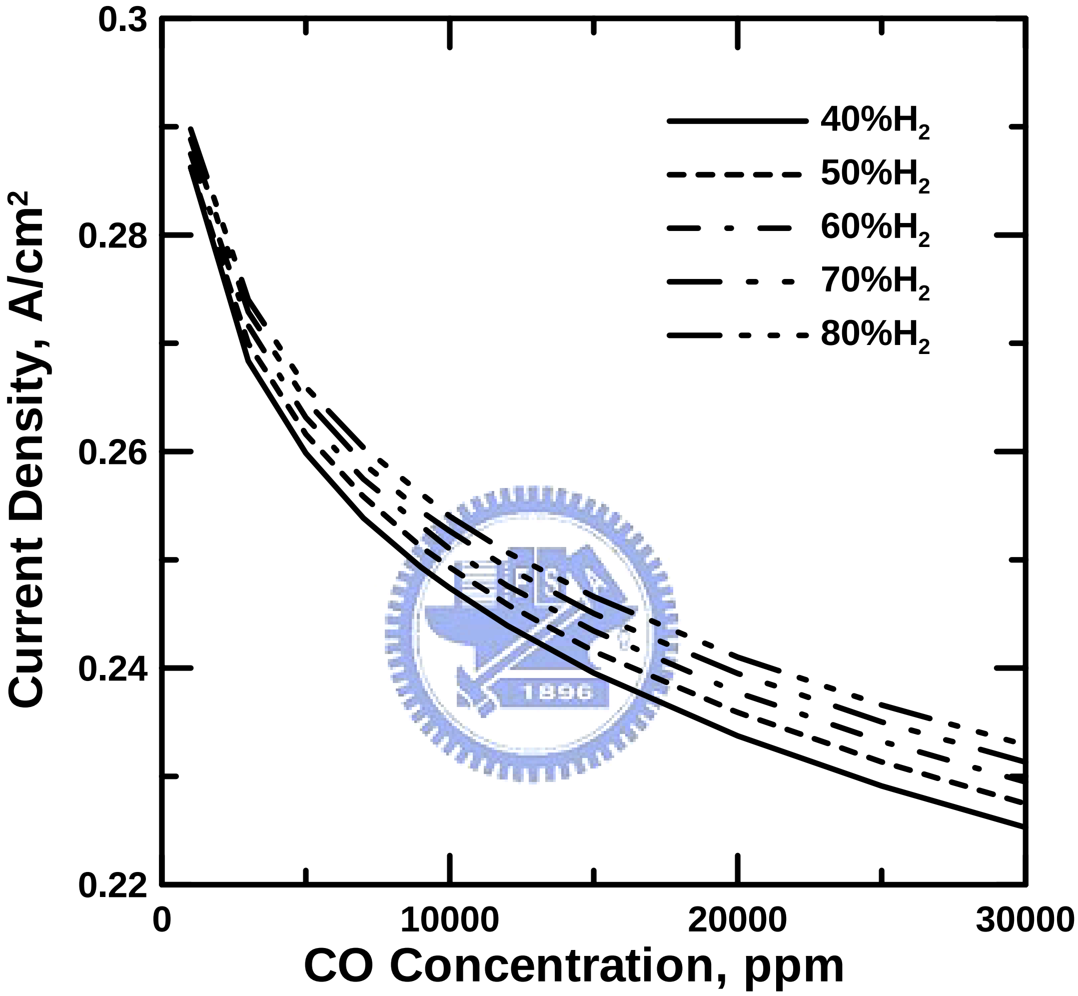

Fig. 5.9 Effects of CO contents on the current density under various hydrogen concentrations at 0.6 V, 180°C.

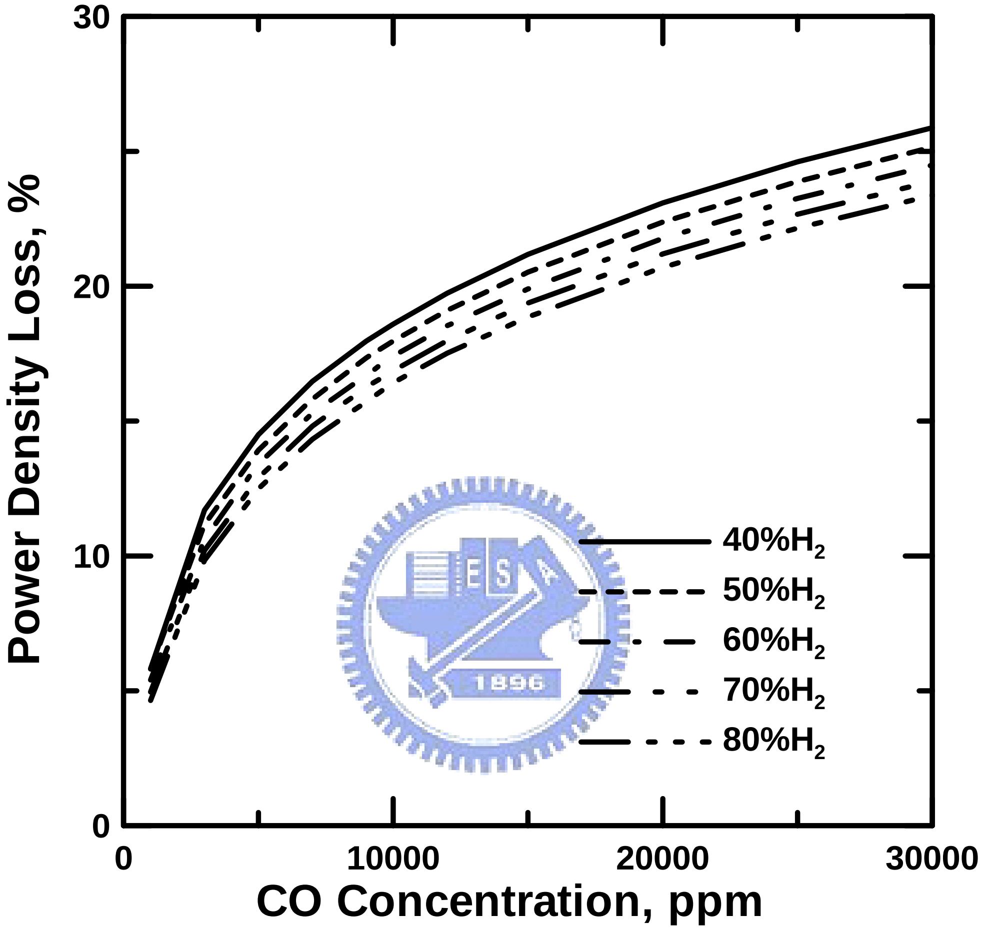

Fig. 5.10 Percentage of power density loss under various CO and hydrogen contents at 0.6 V, 180°C.

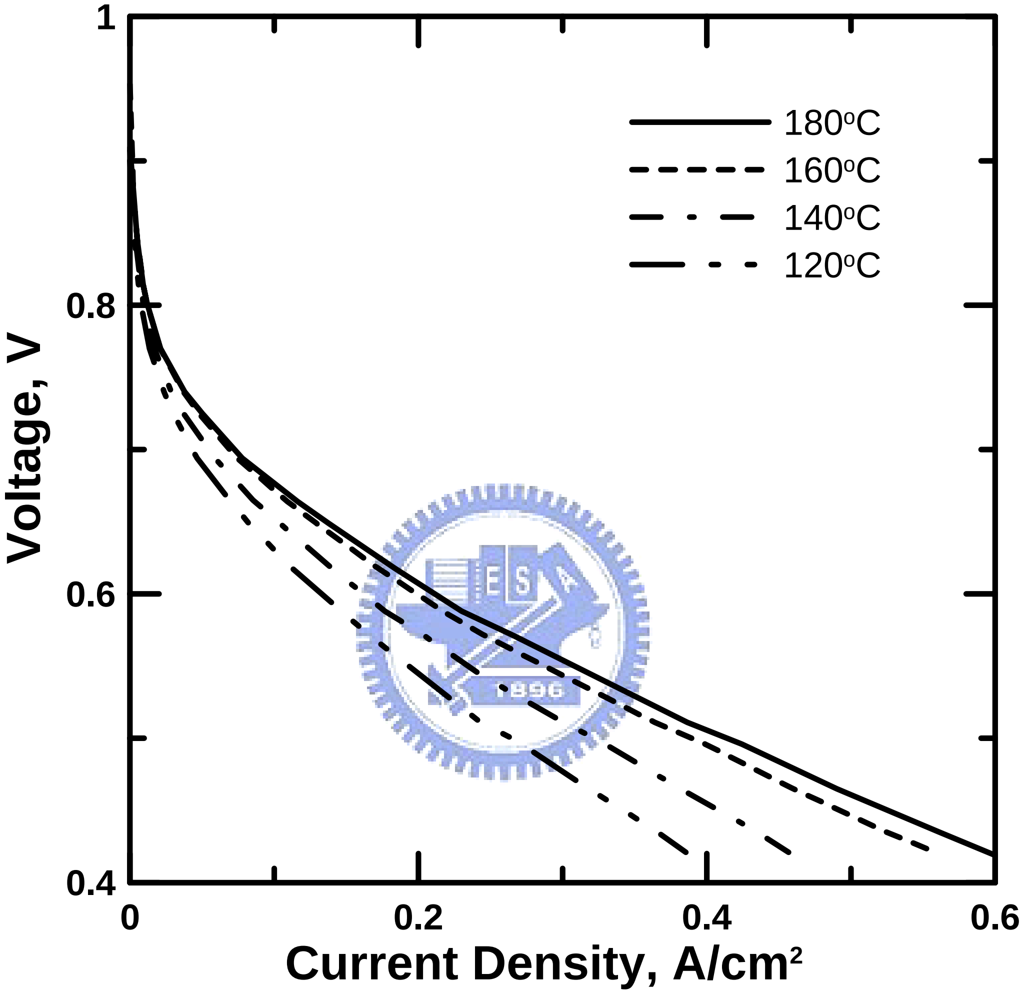

Fig. 5.11 Experimental measurements of polarization curves of the PBI membrane fuel cell at temperature 120, 140, 160 and 180°C.

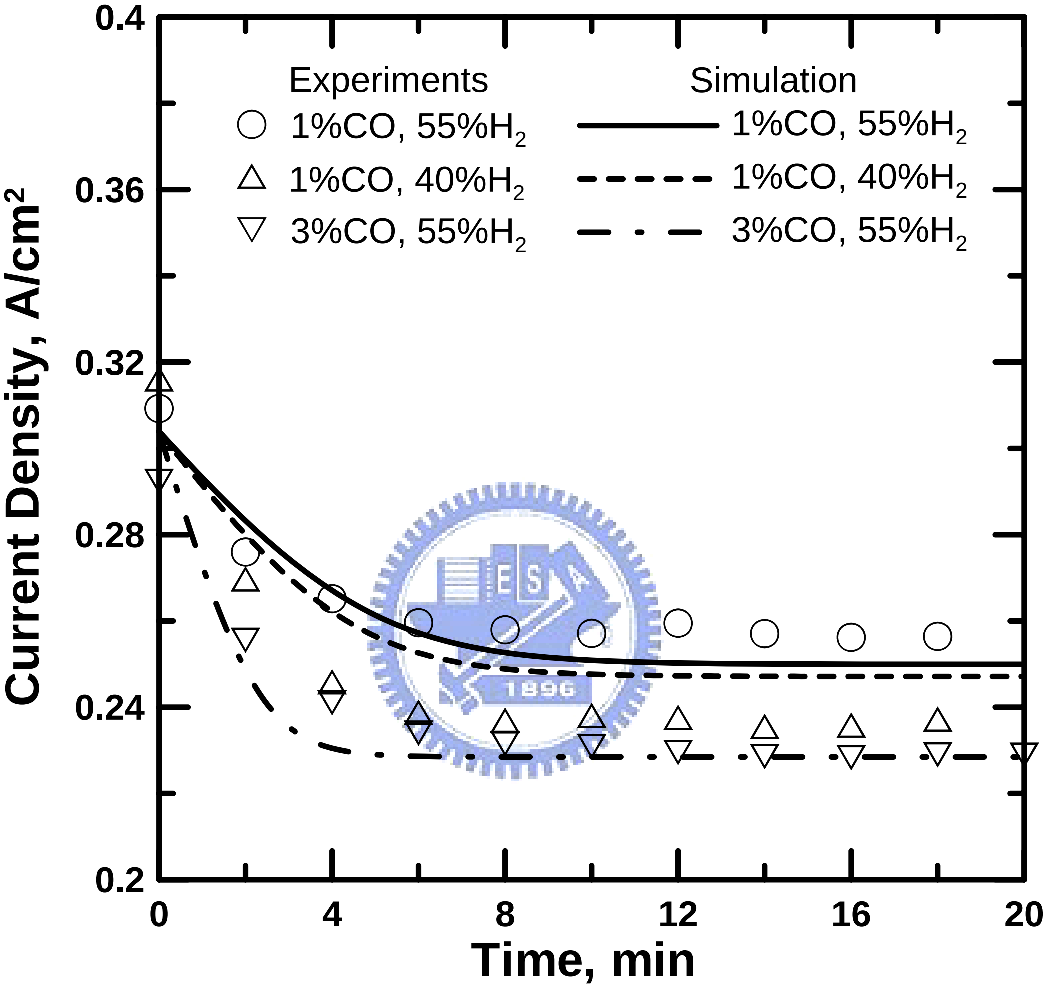

Fig. 5.12 The comparisons of simulation results with experimental data at 0.6 V, 180°C.

6 Conclusions and Recommendation

The present study investigates CO poisoning effect of Nafion and PBI membrane fuel cells. The CO kinetic model is developed and extended to simulate transient characteristics of the CO poisoning process. The transportation of hydrogen, CO, oxygen, proton, liquid and vapor water are all discussed. This work can accurately predict fuel cell performance under various fuel compositions and realize transient degradations of fuel cell performance, thus giving the following conclusions:

First, the catalyst layer is treated as a thin film instead of an interface to investigate the response time interval required to reach the steady state under different conditions. Even more current density distribution, reactant gas distribution, and coverage across the anode catalyst layer are also investigated. As a result, the θ_H decreases with increasing CO concentration, which in turn, causes a low hydrogen electro-oxidation. The time interval needed to reach steady state t_{ss} is strongly influenced by CO concentrations. This is due to the fact that the CO electro-oxidation is insufficient to free up the catalyst sites. Therefore, it is easy to accumulate on the Pt catalyst site with a high level CO concentration and then decrease the hydrogen oxidation, which in turn, cause a decrease in the response time interval t_{ss}. A better cell performance can be obtained for a system with a higher overpotential or gas porosity, especially at low level CO concentration. This is because that for a case with a high porosity, the hydrogen fuel can be easily fed into the catalyst layer and a high anode overpotential can free up the catalyst sites for hydrogen oxidation by bringing about the great CO oxidation. Finally, effects of the CO levels have a significant impact on the response time interval, especially for the low level ppm CO.

Next, we modified and extended our previous study from single-phase to two-phase model. A much more comprehensive mathematical model was developed to gain a further understanding of CO poisoning process. The transportation of hydrogen, carbon monoxide, proton, vapor and liquid water were all considered in this work across the MEA of the PEMFC. The hydrogen coverage and liquid water saturation decreases as the CO concentration and the dilute of hydrogen increase. Increasing the amount of CO and hydrogen dilution also drop the gradient of the liquid water distribution across the membrane and fall the loss of ionic potential. The distribution of liquid water depends more strongly on the CO concentration than on dilution of hydrogen in the MEA of the fuel cell. The theoretical results indicate that a large dropping rate of the current density is observed in the range between 10-50 ppm CO. In this study, increasing the amount of pure hydrogen can drastically increase the cell current density for a wide range 10~100 ppm of CO, promoting the tolerance for CO of the fuel cell.

In order to realize the transient nature of poisoning from carbon monoxide across the MEA of the PEMFC, we modified the previous steady state two-phase model. Platinum catalyst has a strong affinity for CO, inhibiting the electro-oxidation of hydrogen. The hydrogen coverage and liquid water saturation declines as the reaction proceeded. The gradient of the liquid water distribution across the membrane and the ionic potential also fell with time. The distribution of liquid water depends more strongly on the CO concentration than on dilution of hydrogen in the MEA of the fuel cell. The theoretical results indicate that a higher CO concentration results in large drop in the time to reach steady state t_{ss}. In this study, increasing the amount of pure hydrogen drastically increases t_{ss} for a wide range 10~100 ppm of CO contents. At 100 ppm CO, the cell voltage does not clearly affect t_{ss}. A large time t_{ss} can be achieved by increasing the amount of hydrogen. At 10 ppm CO, the influence of hydrogen dilution on the time t_{ss} is weak at cell voltage below 0.6 V. Thereafter, the time t_{ss} increases markedly by increasing hydrogen content. In this work, the transient decay of fuel cell performance under various fuel compositions was predicted accurately. The theoretical results showed good agreement with experiments.

High temperature PBI membrane is a potential option to solve water management and tolerance of CO. The present study develops a transient, one-dimensional mathematical model to analyze PBI membrane fuel cells. Various fuel compositions are considered to realize the effect of fuel composition such as CO concentration and hydrogen dilution of the fuel cell. Chemical bonding is much stronger between CO and the Pt catalyst than hydrogen. Thus, hydrogen coverage rapidly declines with time. Higher CO content and hydrogen dilution also cause significant increase on CO coverage. Ionic potential loss decreases with time during the CO poisoning process. The polarization curves of PBI membrane fuel cell were measured at temperature 120~180^{o}C. Simulation results show good agreement with experimental data. The simulation from this work can accurately predict fuel cell performance under various fuel compositions and realize transient degradations of fuel cell performance, thus providing sufficient information for the designing reformer and fuel cell system.

Different types of alloy catalyst such as Pt/Ru, Pt/Mo should be considered in the future work. Chemical kinetics of alloy catalyst is still absent to investigate the CO tolerance under various fuel compositions. Theoretical studies are required to gain a further understanding of chemical kinetics of anode composite electrocatalysts. A complete set of experimental data under various RHs, temperatures and fuel compositions of PBI membrane fuel cells is also absent. These studies are definitely required for the designing fuel cell systems. In addition, an integration of PBI membrane fuel cells with methanol steam reformer is desired in the future works.

References

1. R. C. Urian, A. F. Gulla, S. Mukerjee, 2003, “Electrocatalysis of Reformate Tolerance in Proton Exchange Membranes Fuel Cells: Part I,” Journal of Electroanalytical Chemistry, 554-555, pp. 307-324.
2. J. Zhang, R. Datta, 2002, “Sustained Potential Oscillations in Proton Exchange Membrane Fuel Cells with PtRu as Anode Catalyst,” Journal of the Electrochemical Society, 149, pp. A1423-1431.
3. B. N. Grgur, N. M. Markovic, P. N. Ross, 1999, “The Electro-Oxidation of H_2 and H_2/CO Mixtures on Carbon-Supported Pt_xMo_y Alloy Catalysts,” Journal of the Electrochemical Society, 146, pp. 1613-1619.
4. S. J. Lee, S. Mukerjee, E. A. Ticianclli, J. McBreen, 1999, “Electrocatalysis of CO Tolerance in Hydrogen Oxidation Reaction in PEM Fuel Cells,” Electrochimica Acta, 44, pp. 3283-3293.
5. M. Murthy, M. Esayian, A. Hobson, S. Mackenzie, W. Lee, J. W. Van Zee, 2001, “Performance of a Polymer Electrolyte Membrane Fuel Cell Exposed to Transient CO Concentrations,” Journal of the Electrochemical Society, 148, pp. A1141-A1147.
6. J. Larminie, A. Dicks, 2003, “Fuel Cell Systems Explained,” 2nd ed. Wiley.
7. J. Kim, S. M. Lee, S. Srinivasan, C. E. Chamberlin, 1995, “Modeling of Proton Exchange Membrane Fuel Cell Performance with an Empirical Equation,” Journal of the Electrochemical Society, 142, pp. 2670-2674.
8. D. R. Sena, E. A. Ticianelli, V. A. Paganin, E. R. Gonzalez, 1999, “Effect of Water Transport in a PEFC at Low Temperatures Operating with Dry Hydrogen,” Journal of Electroanalytical Chemistry, 477, pp. 164-170.

9. L. Pisani, G. Murgia, M. Valentini, B, D'Aguanno, 2002, "A New Semi-Empirical Approach to Performance Curves of Polymer Electrolyte Fuel Cells," Journal of Power Sources, 108, pp. 192-203.
10. E. Passalacqua, F. Lufrano, G. Squadrito, A. Patti, L. Giorgi, 2001, "Nafion Content in the Catalyst Layer of Polymer Electrolyte Fuel Cells: Effects on Structure and Performance," Electrochimica Acta, 46, pp. 799-805.
11. A. Z. Weber, J. Newman, 2004, "Modeling Transport in Polymer-Electrolyte Fuel Cells," Chemical Reviews, 104, pp. 4679-4726.
12. A. A. Kulikovsky, 2003, "Quasi-3D Modeling of water transport in Polymer Electrolyte Fuel Cells," Journal of the Electrochemical Society, 150, pp. A1432-A1439.
13. N. P. Siegel, M. W. Ellis, D. J. Nelson, M. R. von Spakovsky, 2003, "Single Domain PEMFC Model Based on Agglomerate Catalyst Geometry," Journal of Power Sources, 115, pp. 81-89.
14. D. M. Bernardi, M. W. Verbrugge, 1992, "A Mathematical Model of the Solid-Polymer-Electrolyte Fuel Cell," Journal of the Electrochemical Society, 139, pp. 2477-2491.
15. D. M. Bernardi, M. W. Verbrugge, 1991, "Mathematical Model of a Gas Diffusion Electrode Bounded to a Polymer Electrolyte," AICHE Journal, 37, pp. 1151-1163.
16. G. Murgia, L. Pisani, M. Valentini, B. D'Aguanno, 2002, "Electrochemistry and Mass Transport in Polymer Electrolyte Membrane Fuel Cells," Journal of the Electrochemical Society, 149, pp. A31-A38.
17. A. Rowe, X. G. Li, 2001, "Mathematical Modeling of Proton Exchange Membrane Fuel Cells," Journal of Power Sources, 102, pp. 82-96.

18. A. A. Kulikovsky, J. Divisek, A. A. Kornyshev, 1999, “Modeling the Cathode Compartment of Polymer Electrolyte Fuel Cells: Dead and Active Reaction Zones,” Journal of the Electrochemical Society, 146, pp. 3981-3991.
19. V. Gurau, F, Barbir, H. Liu, 2000, “An Analytical Solution of a Half-Cell Model for PEM Fuel Cells,” Journal of the Electrochemical Society, 147, pp. 2468-2477.
20. H. S. Chu, C. Yeh, F. Lin, 2002, “Effects of Porosity Change of Gas Diffuser on Performance of Proton Exchange Membrane Fuel Cell,” Journal of Power Sources, 123, pp. 1-9.
21. W. He, J. S. Yi, T. V. Nguyen, 2000, “Two-Phase Flow Model of the Cathode of PEM Fuel Cells Using Interdigitated Flow Fields,” AICHE Journal, 46, pp. 2053-2064.
22. D. Natarajan, T. V. Nguyen, 2003, “Three-Dimensional Effects of Liquid Water Flooding in the Cathode of a PEM Fuel Cell,” Journal of Power Sources, 115, pp. 66-80.
23. L. You, H. Liu, 2002, “A Two-Phase Flow and Transport Model for the Cathode of PEM Fuel Cells,” International Journal of Heat and Mass Transfer, 45, pp. 2277-2287.
24. U. Pasaogullari, C. Y. Wang, 2005, “Two-Phase Modeling and Flooding Prediction of Polymer Electrolyte Fuel Cells,” Journal of the Electrochemical Society, 152, pp. A380-A390.
25. .L. Pisani, G. Murgia, .M. Valentini, B. D’Aquanno, 2002, “A Working Model of Polymer Electrolyte Fuel Cells,” Journal of the Electrochemical Society, 149, pp. A898-A904.
26. L. Pisani, M. Valentini, G. Murgia, 2003, “Analytical Pore Scale Modeling of the Reactive Regions of Polymer Electrolyte Fuel Cells,” Journal of the Electrochemical Society, 150, pp. A1549-A1559.

27. G. Lin, W. He, T. V. Nguyen, 2004, "Modeling Liquid Water Effects in the Gas Diffusion and Catalyst Layers of the Cathode of a PEM Fuel Cell," Journal of the Electrochemical Society, 151, pp. A1999-A2006.
28. R. B. Bird, W. E. Stewart, E. N. Lightfoot, 2002, "Transport Phenomena," 2nd ed., John Wiley & Sons, New York.
29. H. S. Fogler, 1992, "Elements of Chemical Reaction Engineering," 2nd ed., Prentice-Hall.
30. T. Okada, N. Nakamura, M. Yuasa, I. Sekine, 1997, "Ion and Water Transport Characteristics in Membranes for Polymer Electrolyte Fuel Cells Containing H^+ and Ca^{2+} Cations," Journal of the Electrochemical Society, 144, pp. 2744-2750.
31. T. Okada, S. Moller-Holst, O. Gorseth, S. Kjelstrup, 1998, "Transport and Equilibrium Properties of Nafion Membranes with H^+ and Na^+ Ions," Journal of Electroanalytical Chemistry, 442, pp. 137-145.
32. T. Okada, Y. Ayato, M. Yuasa, I. Sekine, 1999, "The Effect of Impurity Cations on the Transport Characteristics of Perfluorosulfonated Ionomer Membranes," J. Phys. Chem. B, 103, pp. 3315-3322.
33. T. Okada, J. Dale, Y. Ayato, O. Andreas, M. Yuasa, I. Sekine, 1999, "Unprecedented Effect of Impurity Cations on the Oxygen Reduction Kinetics at Platinum Electrodes Covered with Perfluorinated Ionomer," Langmuir, 15, pp.8490-8496.
34. T. Okada, Y. Ayato, J. Dale, M. Yuasa, I. Sekine, O. Andreas, 2000, "Oxygen Reduction Kinetics at Platinum Electrodes Covered with Perfluorinated Inomer in the Presence of Impurity Cations Fe^{3+}, Ni^{2+} and Cu^{2+} ," Physical Chemistry Chemical Physics, 2, pp. 3255-3261.

35. T. Okada, Y. Ayato, H. Satou, M. Yuasa, I. Sekine, 2001, “The Effect of Impurity Cations on the Oxygen Reduction Kinetics at Platinum Electrodes Covered with Perfluorinated Ionomer,” J. Phys. Chem. B, 105, pp. 6980-6986.

36. T. Okada, H. Satou, M. Okuno, M. Yuasa, 2002, “Ion and Water Transport Characteristies of Perfluorosulfonated Ionomer Membranes with H^+ and Alkali Metal Cations,” J. Phys. Chem. B, 106, pp. 1267-1273.

37. T. Okada, H. Satou, M. Okuno, M. Yuasa, 2003, “Effect of Additives on Oxygen Reduction Kinetics at the Interface between Platinum and Perfluorinated Ionomer,” Langmuir, 19, pp. 2325-2332.

38. T. Okada, 1999, “Theory for Water Management in Membranes for Polymer Electrolyte Fuel Cells. Part 1. The Effect of Impurity Ions at the Anode Side on the Membrane Performances,” Journal of Electroanalytical Chemistry, 465, pp. 1-17.

39. T. Okada, 1999, “Theory for Water Management in Membranes for Polymer Electrolyte Fuel Cells. Part 2. The Effect of Impurity Ions at the Cathode Side on the Membrane Performances,” Journal of Electroanalytical Chemistry, 465, pp. 18-29.

40. F. Chen, Y. G. Su, C. Y. Soong, W. M. Yan, H. S. Chu, 2004, “Transient Behavior of Water Transport in the Membrane of a PEM Fuel Cell,” Journal of Power Sources, 566, pp. 85-93.

41. V. M. Schmidt, H.-F. Oetjen, J. Divisek, 1997, “Performance improvement of a PEMFC using fuels with CO by addition of oxygen-evolving compounds,” Journal of the Electrochemical Society, 144, pp. L237-L238.

42. J. Divisek, H.-F. Oetjen, V. Peinecke, V. M. Schmidt, U. Stimming, 1998, “Components for PEM fuel cell systems using hydrogen and CO containing fuels,” Electrochim. Acta, 43, pp. 3811-3815

43. Y. Si, R. Jiang, J. C. Lin, H. R. Kunz, J. M. Fenton, 2004, "CO tolerance of carbon-supported platinum-ruthenium catalyst at elevated temperature and atmospheric pressure in a PEM fuel cell," Journal of the Electrochemical Society, 151, pp. A1820-A1824.

44. J. Zhang, T. Thampan, R. Datta, 2002, "Influence of anode flow rate and cathode oxygen pressure on CO poisoning of proton exchange membrane fuel cells," Journal of the Electrochemical Society, 149, pp. A765-A772.

45. H. Yu, Z. Hou, B. Yi, Z. Lin, 2002, "Composite anode for CO tolerance proton exchange membrane fuel cells," Journal of Power Sources, 105, pp. 52-57.

46. E. I. Santiago, V. A. Paganin, M. do. Carmo, E. R. Gonzalez, E. A. Ticianelli, 2005, "Studies of CO tolerance on modified gas diffusion electrodes containing ruthenium dispersed on carbon," Journal of Electroanalytical Chemistry, 575, pp. 53-60.

47. X. Xue, J. Ge, C. Liu, W. Xing, T. Lu, 2006, "Novel chemical synthesis of Pt–Ru–P electrocatalysts by hypophosphite deposition for enhanced methanol oxidation and CO tolerance in direct methanol fuel cell," Electrochemistry Communications, 8, pp. 1280-1286.

48. Y. Liang, H. Zhang, H. Zhong, X. Zhu, Z. Tian, D. Xu, B. Yi, 2006, "Preparation and characterization of carbon-supported PtRuIr catalyst with excellent CO-tolerant performance for proton-exchange membrane fuel cells," Journal of Catalysis, 238, pp. 468-476.

49. Z. Qi, C. He, A. Kaufman, 2002, "Effect of CO in the Anode Fuel on the Performance of PEM Fuel Cell Cathode," Journal of Power Sources, 111, pp. 239-247.

50. P. A. Adock, S. V. Pacheco, K. M. Norman, F. A. and Uribe, 2005, "Transient Metal Oxides as Reconfigured Fuel Cell Anode Catalysts for Improved CO

Tolerance：Polarization Data," Journal of the Electrochemical Society, 152, pp. A459-A466.

51. A. H. Thomason, T. R. Lalk, A. J. Appleby, 2004, "Effect of Current Pulsing and Self-Oxidation on the CO Tolerance of a PEM Fuel Cell," Journal of Power Sources, 135, pp. 204-211.
52. L. P. L. Carrete, K. A. Friedrich, M. Hubel, U. Stimming, 2001, "Improvement of CO Tolerance of Proton Exchange Membrane Fuel Cells by a Pulsing Technique," Physical Chemistry Chemical Physics, 3, pp. 320-324.
53. S. Um, C. Y. Wang, K. S. Chen, 2000, "Computational fluid dynamics modeling of proton exchange membrane fuel cells," Journal of the Electrochemical Society, 147. pp. 4485-4493.
54. T. Gu, W. -K. Lee, J. W. Van Zee, M. Murthy, 2004, "Effect of reformate components on PEMFC performance," Journal of the Electrochemical Society, 151, pp. A2100-A2105.
55. J. H. Wee, K. Y. Lee, 2006, "Overview of the development of CO-tolerant anode electrocatalysts for proton-exchange membrane fuel cells," Journal of Power Sources, 157, pp. 128-135.
56. T. E. Springer, T. Rockward, T. A. Zawodzinski, S. Gottesfeld, 2001, "Model for Polymer Electrolyte Fuel Cell Operation on Reformate Feed," Journal of the Electrochemical Society, 148, pp. A11-A23.
57. S. H. Chan, S. K. Goh, S. P. Jiang, 2003, "A mathematical model of polymer electrolyte fuel cell with anode CO kinetics," Electrochimica Acta, 48, pp. 1905-1919.
58. K. K. Bhatia, C. Y. Wang, 2004, "Transient carbon monoxide poisoning of a polymer electrolyte fuel cell operating on diluted hydrogen feed," Electrochimica Acta, 49, pp. 2333-2341.

59. J. J. Baschuk. X. Li, 2003, "Modeling CO poisoning and O_2 bleeding in a PEM fuel cell anode," Int. J. Energy Res. 25, pp. 1095-1116.

60. J. S. Wainright, J. –T. Wang, R. F. Savinell, M. Litt, 1995, "Acid-Doped Polybenzimidazoles: A New Polymer Electrolyte," Journal of the Electrochemical Society, 142, pp. L121-L123.

61. J. –T. Wang, R. F. Savinell, J. S. Wainright, M. Litt, H. Yu, 1996, "A H_2/O_2 fuel cell using acid doped polybenzimidazole as polymer electrolyte," Electrochimica Acta, 41, pp. 193-197.

62. Q. Li, H. A. Hjuler, N, J. Bjerrum, 2001, "Phosphoric acid doped polybenzimidazole membranes: Physiochemical characterization and fuel cell applications," Journal of Applied Electrochemistry, 31, pp. 773-779.

63. R. He, Q. Li, G. Xiao, N. J. Bjerrum, 2003, "Proton conductivity of phosphoric acid doped polybenzimidazole and its composites with inorganic proton conductors," Journal of Membrane Science, 226, pp. 169-184.

64. Q. Li, R. He, R. W. Berg, H. A. Hjuler, N. J. Bjerrum, 2004, "Water uptake and acid doping of polybenzimidazoles as electrolyte membranes for fuel cells," Solid State Ionics, 168, pp. 177-185.

65. H. Pu, Q. Liu, G. Liu, 2004, "Methanol permeation and proton conductivity of acid-doped poly(N-ethylbenzimidazole) and poly(N-methylbenzimidazole)," Journal of Membrane Science, 241, pp. 169-175.

66. Y. –L. Ma, J. S. Wainright, M. H. Litt, R. F. Savinell, 2004, "Conductivity of PBI Membranes for High-Temperature Polymer Electrolyte Fuel Cells," Journal of the Electrochemical Society, 151, pp. A8-A16.

67. Z. Liu, J. S. Wainright, R. F. Savinell, 2004, "High-temperature polymer electrolytes for PEM fuel cells: study of the oxygen reduction reaction (ORR) at a Pt–polymer electrolyte interface," Chemical Engineering Science, 59, pp. 4833-

4838.

68. Z. Liu, J. S. Wainright, M. H. Litt, R. F. Savinell, 2006, “Study of the oxygen reduction reaction (ORR) at Pt interfaced with phosphoric acid doped polybenzimidazole at elevated temperature and low relative humidity,” Electrochimica Acta, 51, pp. 3914- 3923.
69. Q. Li, R. He, J. Gao, J. O. Jensen, N. J. Bjerrum, 2003, “The CO Poisoning Effect in PEMFCs Operational at temperatures up to 200°C,” Journal of the Electrochemical Society, 150, pp. A1599-A1605.
70. H. P. Dhar, L. G. Christner, A. K. Kush, H. C. Maru, 1986, “Performance Study of a Fuel Cell Pt-on-C Anode in Presence of CO and CO2, and Calculation of Adsorption Parameters for CO Poisoning,” Journal of the Electrochemical Society, 133, pp. 1574-1582.
71. H. P. Dhar, L. G. Christner, A. K. Kush, 1987, “Nature of CO Adsorption during H2 Oxidation in Relation to Modeling for CO Poisoning of a Fuel Cell Anode,” Journal of the electrochemical Society, 134, pp. 3021-3026.
72. J. D. Holladay, J. S. Wainright, E. O. Jones, S. R. Gano, 2004, “Power generation using a mesoscale fuel cell integrated with a microscale fuel processor,” Journal of Power Sources, 130, pp. 111-118.
73. D. J. Seo, W. L. Yoon, Y. G. Yoon, S. H. Park, G. G. Park, C. S. Kim, 2004, “Development of a micro fuel processor for PEMFCs,” Electrochimica Acta, 50, pp. 719–723.
74. G. G. Park, S. D. Yima, Y. G. Yoon, C. S. Kim, D. J. Seo, K. Eguchi, 2005, “Hydrogen production with integrated microchannel fuel processor using methanol for portable fuel cell systems,” Catalysis Today, 110, pp. 108–113.
75. C. Pan, R. He, Q. Li, J. O. Jensen, N. J. Bjerrum, H. A. Hjulmand, A. B. Jensen, 2005, “Integration of high temperature PEM fuel cells with a methanol reformer,”

Journal of Power Sources, 145, pp. 392-398.

76. Y, Kawamura, N. Ogura, T. Yamamoto, A. Igarashi, 2006, "Aminiaturized methanol reformer with Si-based microreactor for a small PEMFC," Chemical Engineering Science, 61, pp. 1092-1101.
77. D. Cheddie, N. Munroe, 2006, "Mathematical model of a PEMFC using a PBI membrane," Energy Conversion and Management, 47, pp. 1490-1504.
78. A. R. Korsgaard, R. Refshauge, M. P. Nielsen, M. Bang, S. K. Kær, 2006, "Experimental characterization and modeling of commercial polybenzimidazole-based MEA performance," Journal of Power Sources, 162, pp. 239-245.
79. H. F. Oetjen, V. M. Schmit, U. Stimming, F. Trila, 1996, "Performance Data of a Proton Exchange Membrane Fuel Cell Using H_2/CO as Fuel Gas," Journal of the Electrochemical Society, 143, pp. 3838-3842.
80. T. Okada, G. Xie, Y. Tanabe, 1996, "Theory of water management at the anode side of polymer electrolyte fuel cell membranes," Journal of Electroanalytical Chemistry, 413, pp. 49-65.
81. Y. Wang, C. Y. Wang, 2005, "Transient analysis of polymer electrolyte fuel cells," Electrochimica Acta, 50, pp. 1307-1315.

List of Publications

1. S. K. Wu, C. P. Wang, H. S. Chu, "Size Effects of the Heat Transfer for a Two-Layer Concentric Circular Tube with Interface Thermal Resistance," ***J. Chinese Society of Mechanical Engineers***, 2004, 25, 115-123.
2. H. S. Chu, C. P. Wang, W. C. Liao, W. M. Yan, "Transient Behaviors of CO Poisoning in the Anode Catalyst Layer of PEM Fuel Cell," ***J. Power Sources***, 2006, 159, 1071-1077.
3. C. P. Wang, H. S. Chu, "Transient Analysis of Multicomponent Transport with Carbon Monoxide Poisoning Effect of a PEM Fuel Cell," ***J. Power Sources***, 2006, 159, 1025-1033.
4. C. P. Wang, H. S. Chu, "Two-Phase Modeling of a PEMFC with CO Poisoning Effect Using Dilute Hydrogen Feed," ***ASME Fuel Cell Conference*** 2006-97208, Irvine, CA, 19-21, June, 2006.
5. C. P. Wang, H. S. Chu, Y. Y. Yan, K. L. Hsueh, "Transient Evolution of Carbon Monoxide Poisoning Effect of PBI Membrane Fuel Cells", ***J. Power Sources***, 2007, (Published).